SEA-LEVEL VERSUS BOTTOM-CURRENT INFLUENCED DIAGENESIS

A Dissertation

by

KIERON CALEB PRINCE

Submitted to the Office of Graduate and Professional Studies of
Texas A&M University
in partial fulfillment of the requirements for the degree of

DOCTOR OF PHILOSOPHY

Chair of Committee,	Juan Carlos Laya Pereira
Committee Members,	Ethan Grossman
	Michael Pope
	Carlos Alvarez Zarikian
Head of Department,	Julie Newman

May 2020

Major Subject: Geology

ABSTRACT

This study presents the diagenetic evolution of the Kardiva Platform, Maldives, located in the tropical region of the Indian Ocean off the southwest coast of India. This drowned carbonate platform was susceptible to high amplitude sea-level variation as well as intense climate events during the Neogene. International Ocean Discovery Program Expedition 359 Sites U1465, U1466, U1468, U1469, and U1470 were situated in waters between 400 and 522 meters with the study interval covering over 1400 m of core. These cores were studied using stable isotopes of C and O, strontium isotope dating, x-ray diffraction and petrographic methods.

The Kardiva Platform was impacted by subaerial exposure due to glacially controlled changes in sea-level during the expansion of the East Antarctic Ice Sheet (EAIS). The evidence of exposure and meteoric alteration is restricted to the platform sequences (PS) which show a major exposure surface, characterized by negative excursions in values of $\delta^{18}O$ and $\delta^{13}C$, and low strontium and magnesium elemental concentrations for carbonate cements. This represents the first identification of subaerial platform exposure for Miocene carbonate sediments in the Maldives and provides a record of sea-level in an area where this is not well constrained.

Dolomite samples showed a series of characteristics including decreasing crystal size from margin to slope, a flat-topped geometry to the ~50 m subsea dolomite body, cool dolomite formation temperatures (~14°C), and non-stoichiometric dolomite compositions (39-44 mole% $MgCO_3$) that are incompatible with the commonly invoked

Kohout Convection model. We propose a new model whereby oceanic bottom-currents created the “current pumping” of seawater through the upper ~100 meters of the older platform and younger periplatform deposits to create subsurface dolomite.

At Site U1468, inflections from decreasing to increasing crystal sizes occur at or below the interglacial surfaces. This trend suggests the presence of an up to 20 - 25 m deep advective zone in the middle to late Miocene sediments. Advection strengthened in glacial periods, extending into the previously deposited interglacial sediments. We suggest that changes in glacioeustasy from the middle to late Miocene influenced oceanic circulation and bottom-currents and thereby the advection of seawater below the sediment-water interface.

DEDICATION

For Sasha, Kaden, Kalana and Cheryl.

And for the boy who dreamed, they do come true.

ACKNOWLEDGEMENTS

I would like to thank my committee chair, Dr. Laya for his mentorship and my committee members, Prof. Grossman, Prof. Pope and Dr. Alvarez Zarikian for their guidance and support throughout the course of this research. Thanks are also extended to Professors Dave Budd and Hongbin Zhan for their invaluable contributions to our novel dolomite model.

This research utilized samples and data provided by the International Ocean Discovery Program (IODP) through the sample request LAYA 29994IODP by Juan Carlos Laya who was a shipboard scientist for Expedition 359. We wish to thank all Expedition 359 scientists, crew and staff for their contributions to this effort without whom this study would not have been possible.

I would also like to thank my friends and colleagues Roy Conte, James Teoh, Tanner Mills for being willing to lend a helping hand or a sympathetic ear. Thanks also go to the department faculty and staff, notably Dr. Julia Reece, Patricia Fike and Suzanne Rosser for their assistance throughout my time at Texas A&M University. Finally, I would like to thank my wife and son for their love and patience through this journey.

CONTRIBUTORS AND FUNDING SOURCES

Contributors

A dissertation committee consisting of Assistant Professor Juan Carlos Laya, Professors Michael Pope and Ethan Grossman of the Department of Geology and Geophysics and Associate Research Scientist Carlos Alvarez Zarikian of the International Ocean Discovery Program supervised this work.

The International Ocean Discovery Program provided the sediment samples analyzed for this dissertation.

Professors Dave Budd and Hongbin Zhan contributed to the development of the dolomite model and the estimations of the depths of seawater infiltration presented in Chapter III respectively.

The following undergraduate students are thanked for their contributions to sample preparation and analysis as part of GEOL 491 – Undergraduate Research: Luke Gezovitch, Cody Calhoun, Ivanakbar Purwamaska, Nurislam Karamurziyez, Brandon Basham, Corbin Berrones, Zachary Coutee, Samuel Meister, Kristen Morris, Michael Walker, David Allen, Alex Brown, and Erin Williams

The student completed all other work conducted for the dissertation independently.

Funding Sources

Graduate study was supported by a scholarship from the National Association of Black Geoscientists and the M.T. Halbouty ’30/AAPG Foundation Endowed Fellowship from the College of Geosciences.

NOMENCLATURE

EAIS	East Antarctic Ice Sheet
SAM	South Asian Monsoon
MBSF	Meters below seafloor
ITCZ	Intertropical Convergence Zone
IODP	International Ocean Discovery Program
VPDB	Vienna Pee Dee Belemnite
XRD	X-ray diffraction
ISM	Indian Summer Monsoon
SIGF	Stable Isotope Geosciences Facility
RIGF	Radiogenic Isotope Geosciences Facility
LA-ICPMS	Laser-ablation inductively coupled plasma
PS	Platform sequence
DS	Drift sequence
LBF	Large benthic foraminifera
HMC	High-magnesium calcite
LMC	Low-magnesium calcite
TWT	Two-way travel time

TABLE OF CONTENTS

Page

LIST OF FIGURES

Page

LIST OF TABLES

Page

CHAPTER I

INTRODUCTION

The Neogene marks a time of significant changes in Earth's climate, oceanography and continental glaciation. Following the relative global warmth of the early Miocene, the development of the East Antarctic Ice Sheet (EAIS) marks a period of rapid cooling, changing ocean circulation and eustasy. In the Indian Ocean, the middle Miocene climatic evolution is marked by the onset and/or intensification of the South Asian Monsoon (SAM).

The Maldives islands are a north-south trending archipelago of about 1200 islands located in the central Indian Ocean. The International Ocean Discovery Program (IODP) Expedition 359 was designed to investigate the changes in sea level and currents as monsoons evolved in the Indian Ocean (Betzler et al., 2017). The Maldives islands were selected as the Site of this expedition as its atolls record almost continuous carbonate deposition and monsoon development from the Eocene to the Holocene. Of the large Modern shallow carbonate platforms, the Maldives are among the least studied. Sedimentology and stratigraphy of these atolls were first described by Aubert (1994) and Aubert and Droxler (1996) using well data from exploration wells North Male-1 (NMA-1) and ARI-1 calibrated to multi-channel seismic profiles

While sea level often is invoked as a key control on carbonate diagenesis (Kendall and Schlager, 1981; Tucker, 1993), less attention is given to the role of bottom-currents and fluid flow as they relate to diagenetic alteration. Most studies of fluid flow

and diagenesis have focused on meteoric flux, downward brine reflux, Kohout convection, compaction dewatering and diffusive processes thereby leaving a gap in our understanding of shallow advective processes (Baker et al., 1982). This shallow advective zone is unique in that fluid movement in the subsurface is not related to diffusion, i.e. a flow from a region of high to low concentration, but rather driven by turbulent flow over bedforms creating a pressure differential. The process of advection can be important in metasomatism as it can supply reactants and remove products for reactions at relatively high rates of 0.5 to 3 meters/year (Simms, 1984; Swart, 2015).

The Maldives archipelago is characterized by a double row of atolls encompassing a basin, the Inner Sea, connected to the open ocean through passages such as the Kardiva Channel. This sedimentary system of drowned platform parts and drifts was the target of International Ocean Discovery Program (IODP) Expedition 359, which aimed to reconstruct its paleoceanographic evolution. This was done by drilling eight Sites in two transects covering shallow to deep water. Of these, we focused on U1465, U1466, U1468, U1469, and U1470. These Sites are in waters between 400 and 522 meters and the study interval covers over 1400 m (**Table 1)**. This study will investigate the diagenetic processes occurring in the Neogene carbonates on the Kadiva platform. Emphasis is dedicated to understanding how these processes were impacted by the significant climatic and oceanographic changes in the middle Miocene when a system of strong bottom currents was established in response to the intensification of the SAM.

Table I.1. Summary of IODP Expedition 359 drill Sites used in this study.

Site	Coordinates (Latitude, Longitude)	Water depth (m)	Sampled interval (mbsf)
U1465	4°55.9873′N, 073°0.6786′E	513	66 - 223
U1466	4°55.9888′N, 073°1.6785′E	518	89 - 664
U1468	4°55.9832′N, 073°4.2780′E	522	51 - 428
U1469	4°54.41′N, 073°0.48′E	427	45 - 153
U1470	4°45.9823′N, 072°59.0267′E	400	148 - 334

Geologic Setting

The sedimentology and stratigraphy of these atolls were first described by Aubert (1994) and Aubert and Droxler (1996) using well data from exploration wells North Male-1 (NMA-1) and ARI-1 calibrated to multi-channel seismic profiles. Sedimentation began with lacustrine sediments infilling the system of grabens. A marine transgression initiated carbonate deposition in the Eocene on the high shoulders of the grabens, forming flat-topped carbonate banks (Aubert, 1994). Carbonate sedimentation continued until the late Early Oligocene when the carbonate platforms were exposed during a fall in sea level resulting in dissolution and karstification. Growth reinitiated in the late Oligocene and the depositional style transitioned from an aggradational shelf type to rimmed banks with protected lagoons as carbonate production became more restricted in response to continued sea level rise during the early Miocene. The platform partially

drowned in the middle Miocene by strong currents sweeping the surface as re-flooding occurred preventing the restart of shallow water sedimentation in parts of the platform (Betzler et al., 2016b; Betzler et al., 2016c; Lüdmann et al., 2013).

Sea level fluctuations dominated Carbonate deposition before the middle Miocene but from the middle Miocene to present, the Maldives atolls underwent a change in sedimentation marked by the onset of increased drift deposits in the Inner Sea. This marked the initiation and/or intensification of the monsoonal climate with its associated bottom currents becoming the dominant control on sedimentation (Betzler et al., 2016c; Lüdmann et al., 2013). This is an unusual sedimentation style for modern carbonate platforms as sedimentation usually reflects changes in sea level and location in relation to the prevailing wind direction (Isern et al., 2004).

While most previous workers focused on the depositional evolution of the Maldives, there has been little study of the platform's diagenetic history, particularly as it relates to the global and regional climactic changes. This project aims to address this problem by utilizing data and samples collected as part of Expedition 359.

Understanding both the controls and products of current driven diagenesis will increase our understanding of the varied processes that act to shape the evolution of carbonate platforms and ultimately will enable us to recognize these processes in similar platforms. This new model of diagenesis, including bottom-current advection within the underlying sediments, provides an additional tool to address changes to rock properties and their impact on reservoirs in dolomitized carbonate platforms.

The objectives of each chapter of this dissertation are as follows: (II) to characterize the diagenesis occurring in the Miocene sediments of the Kardiva platform and interpret them in the framework of regional and global climatic changes occurring in the middle to late Miocene; (III) to determine the dolomitization model for both platform and periplatform sediments of the Kardiva Platform; (III) to investigate the relationship between bottom current strength, grain size and crystal size.

Chapter two focuses on the impact of meteoric diagenesis on the platform and its linkages to regional and global oceanographic and climatic changes. Detailed petrography and geochemistry were conducted to produce a diagenetic model for the platform that incorporates freshwater hydrology as well as a global repositioning of the Intertropical Convergence Zone (ITCZ).

Chapter three focuses on the occurrence, distribution and geochemistry of dolomite from the northern Sites (U1465, U1466, U1468 and U1469). The distribution of the dolomitized interval and its occurrence in the drift deposits younger than the drowning of the platform indicates that traditional models of dolomitization do not explain the dolomite here. A new model for dolomitization by seawater with a bottom current pump is presented.

Chapter four focuses on the occurrences of calcite overgrowths on the benthic foraminifera at Site U1468. Analyses of grain and crystal size distributions show relationships between these and glacial-interglacial periods. Downhole plots indicate a cyclic record between grain size and crystal size that indicates the presence of a shallow advective zone.

CHAPTER II

MIOCENE ONSET OF THE EAST ANTARCTIC ICE SHEET EXPANSION

Abstract

Glaciations are major climatic phenomena that affect local as well as global sedimentation. During the Miocene, climatic changes helped establish modern climate and oceanographic conditions. To understand those changes we studied cores from IODP Sites U1645, U1466, U1468, U1469, and U1470, which recovered complete stratigraphic successions from the early Miocene to present in the Maldives archipelago. These successions are formed by skeletal carbonate sediments deposited under a variety of depositional settings in an isolated carbonate platform.

The Maldives atolls are located in the tropical region of the Indian Ocean off southwest coast of India between 4°45 ′N and 4°55 ′N. These atolls were susceptible to high amplitude sea-level variation as well as intense climate events during the Neogene. We hypothesize that the Kardiva Platform was impacted by subaerial exposure due to glacially controlled changes in sea-level during the expansion of the East Antarctic Ice Sheet (EAIS). Additionally, the platform likely experienced increased rainfall during times of exposure due to narrowing of the seasonal variation of the intertropical convergence zone before South Asian Monsoon intensification at 12.9 My.

The evidence of exposure and meteoric alteration is restricted to the platform sequences (PS) which show a major exposure surface, characterized by a negative excursion in stable isotope values for $\delta^{18}O$ and $\delta^{13}C$, and low strontium elemental concentrations for

carbonate cements. In addition, a major shift in mineralogy from an aragonite to a low-Mg calcite dominated sediments across the drift sequences (DS) to platform sequences (PS) transition is present in all of the study sites. This process indicates mineralogical stabilization of aragonite and high-magnesium calcite (HMC) to low-magnesium calcite (LMC) via dissolution and precipitation reactions in a meteoric diagenetic setting. Furthermore, trace elements ratios for Sr/Ca and Mg/Ca of the cements contrast those from well-preserved brachiopods, which provide the closest record of seawater composition at this time.

This study presents the first identification of platform exposure for Miocene carbonate sediments in the Maldives and provides a record of sea-level in an area where this is not well constrained. Expedition 359 cores from Kardiva platform recorded the onset of the EAIS and the narrowing of the ITCZ during the middle Miocene, before the intensification of the SAM.

Introduction

The middle Miocene expansion of the East Antarctic Ice Sheet (EAIS) was linked to astronomical climatic (Naish et al., 2001; Holbourn et al., 2005). These glacial events represent a significant step toward the establishment of the present-day climate regime after the Mi-1 glaciation (Miller et al., 1991; Roberts et al., 2003; Gupta et al., 2015). In addition, EAIS expansion is linked to increases in the meridional surface temperature gradient, deep ocean water circulation, and burial of organic carbon and,

most notably for carbonate platforms, high amplitude sea level fluctuations, with changes in water depth up to ~ 50 m. (Flower and Kennett, 1994; Naish et al., 2001).

Traditionally, evidence for the middle Miocene expansion of the EAIS was based on glacial sediments proximal to Antarctica (Haywood et al., 2008), marine benthic $\delta^{18}O$ records (Woodruff and Savin, 1989; Miller et al., 1991; Woodruff and Savin, 1991) and benthic foraminiferal species diversity (Singh et al., 2012). However, this rapid ice should also be reflected in global eustasy since high latitude ice sheets cause high-frequency sea-level variations (Haq et al., 1987; Woodruff and Savin, 1991; Abreu and Anderson, 1998).

Sea level is a key control on carbonate diagenesis and can produce profound diagenetic changes through subaerial exposure and the introduction of meteoric fluids (Longman, 1980; Kendall and Schlager, 1981; Tucker, 1993; McKay et al., 1995). Although the Kardiva platform ultimately drowned in the middle Miocene, the amplitude and frequency of sea-level changes during the Neogene make it likely that the Kardiva platform underwent subaerial exposure (Aubert and Droxler, 1996; Lüdmann et al., 2013). Seismic evidence for exposure at the Oligocene-Miocene transition was proposed but others argue that these exposure events cannot be resolved by seismic data alone (Aubert and Droxler, 1996; Belopolsky and Droxler, 2003; Lüdmann et al., 2013).

The atolls of the Maldives archipelago atolls allow for very accurate interpretation of eustasy since they lack terrigenous input and are very tectonically stable. The carbonate stratigraphy in these isolated platforms archives an almost complete record of Cenozoic deposition (Aubert and Droxler, 1992; Aubert, 1994;

Betzler et al., 2017). While the Maldives atolls are described as a living laboratory for the study of carbonate platforms, the effect of environmental change on its diagenetic evolution are not well documented. This paper describes the impact of East Antarctic Ice Sheet expansion on the Neogene Kardiva platform in order to understand how significant climatic and oceanographic changes of the middle Miocene affected the Maldives archipelago. Our hypothesis is that sea level fall associated with the development of the East Antarctic Ice Sheet (EAIS), along with and a wetter climate drove isotopic composition and the meteoric mineralogical stabilization and dissolution of shallow carbonate sediments during the exposure of the platform.

Geological Background

The Maldives is a north-south trending archipelago of about 1200 islands located in the central Indian Ocean just southwest of southernmost tip of India (**Figure II.1**). These islands cover an area 900 km long and 120 km wide and comprise one of the largest modern isolated carbonate platforms on the surface of the earth. The atolls are arranged as two north-south oriented rows, which semi-enclose a perched interior basin called the Inner Sea, where water depths can reach 500 m (**Figure II.1**)

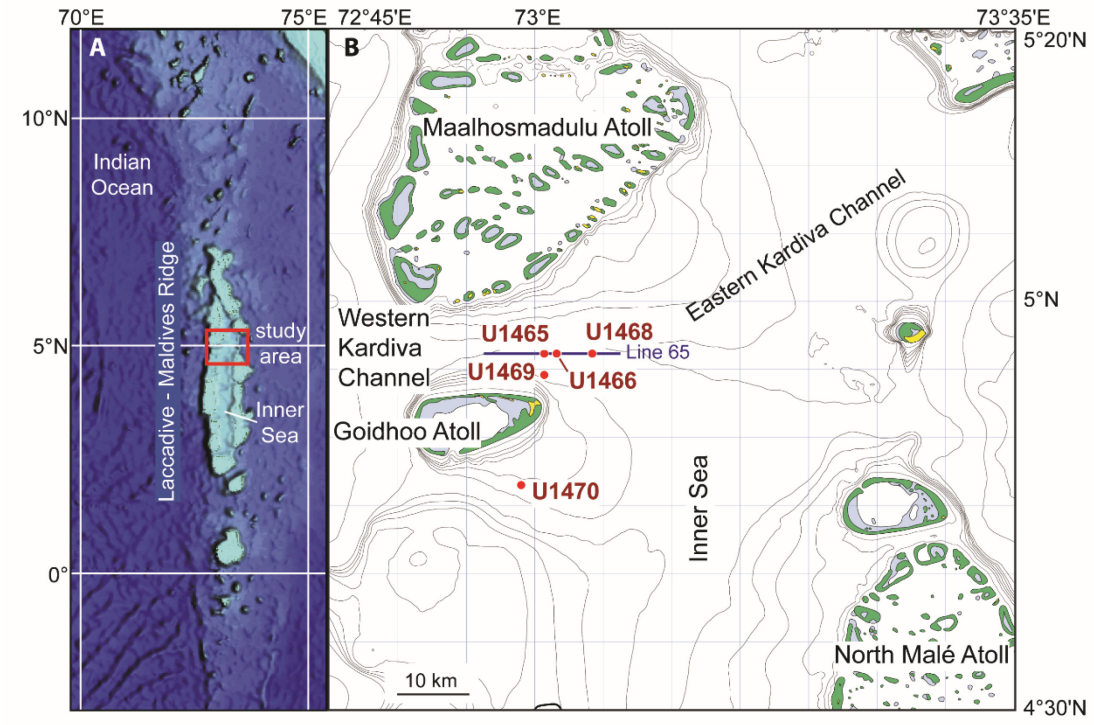

Figure II.1. (A) Location of the Maldives. (B) IODP Expedition 359 Sites in the Inner Sea and the location of the western Kardiva Channel (modified from Betzler et al., 2017). Yellow; islands, blue; reef, green; water depths 10-100 m.

IODP Sites U1465, U1469, and U1470 were drilled to address questions related to platform drowning, depositional systems, and the linkages between seismic and sedimentary datasets (Betzler et al., 2017). These Sites are the focus of this study and are supported with data from Sites U1466 and U1468 (**Table I.1**).

Table II.1. Summary of IODP Expedition 359 Sites used in this study.

Site	Coordinates (Latitude, Longitude)	Water depth (m)	Sampled Interval (mbsf)
U1465	4°55.9873′N, 073°0.6786′E	513	66 - 223
U1466	4°55.9888′N, 073°1.6785′E	518	89 - 664
U1468	4°55.9832′N, 073°4.2780′E	522	51 - 428
U1469	4°54.41′N, 073°0.48′E	427	45 - 153
U1470	4°45.9823′N, 072°59.0267′E	400	148 - 334

Maldives Platform Evolution

The Maldives carbonate platform's history was described using cores collected from early exploration wells (Aubert, 1994), seismic data (Aubert and Droxler, 1996) and most recently the cores collected during IODP Expedition 359 (Betzler et al., 2017). The platform's evolution began with the emplacement of Chagos-Laccadive Ridge 55-57 Ma. This NNE-SSW trending volcanic ridge is a fault-controlled, *en echelon* graben system that was initiated by Réunion hotspot activity beneath the African and Indian plates (Duncan and Storey, 1993; Belopolsky and Droxler, 2003; Lüdmann et al., 2013). Throughout the platform's history, subsidence was mostly constant with an average rate of about 0.043-0.047 mm/yr, punctuated by three periods of increased activity: immediately after volcanic emplacement in the early Paleogene, the late Oligocene, and the late Middle Miocene to uppermost Miocene (Lüdmann et al., 2013).

Sedimentation began with lacustrine deposits infilling the system of grabens followed by marine transgression-initiated carbonate deposition in the Eocene on the

high shoulders of the grabens, forming flat-topped carbonate banks (Aubert, 1994). Carbonate sedimentation continued until the late Early Oligocene when the platforms were exposed during a fall in sea level resulting in dissolution and karstification. Growth re-initiated in the late Oligocene and depositional style transitioned from aggradational shelf to a platform with rimmed banks (e.g. U1465, U1470) and protected lagoons as carbonate production became more restricted in response to continued sea-level rise during the early Miocene (Aubert and Droxler, 1996).

The platform partially drowned in the middle Miocene and strong bottom currents began to sweep the sea-floor due to the intensification of the SAM with the drowning event, associated with increased subsidence, preventing the restart of shallow water sedimentation in many areas (Betzler et al., 2009; Betzler et al., 2018; Lüdmann et al., 2018). Carbonate deposition before the middle Miocene was dominated by sea-level fluctuations but from the middle Miocene to present, the atolls underwent a change in sedimentation style marked by the onset of increased bottom-currents due to the intensification of the South Asian Monsoon (Betzler et al., 2018; Lüdmann et al., 2018).

Miocene Sequence Stratigraphy

The sequence stratigraphy of the platform (**Figure II.2**) was first constructed using seismic data (Belopolsky and Droxler, 2003, 2004). Using erosional truncations and onlap geometries, 11 platform sequence boundaries (PS1-11) and platform sequences (ps1-ps11) were defined within the Neogene carbonate bank before the drowning event with an additional 10 sequence boundaries (DS1-DS10) added in the

post-drowning drift sequences (ds1-ds10) (Betzler et al., 2013). These boundaries were redefined using shipboard biostratigraphy to assign ages to these sequence boundaries (Betzler et al., 2018). During the platform's evolution, there were two main stages of growth with an aggradational phase that spans PS1-PS8 and a progradational phase spanning PS8-PS11. A drowning unconfromity (DS1) (**Figure II.2)** at the top of the platform truncates PS11.

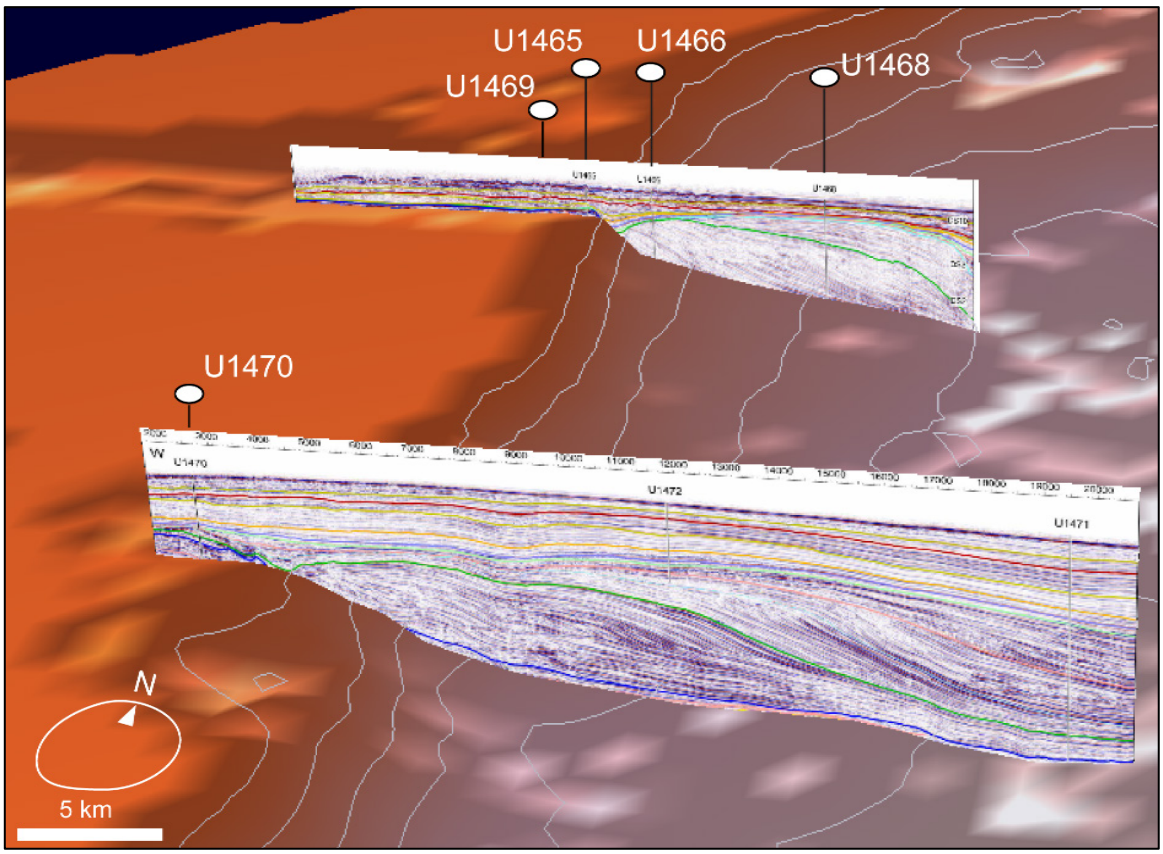

Figure II.2. Paleo-topography of the study area showing the expression of the Kardiva platform from surface DS1 (modified after Lüdmann et al., 2018). Location of the study Sites and seismic lines from Betzler et al. (2017). Contour lines show depth in two-way travel time (TWT).

Facies

Miocene sedimentation in the Maldives archipelago is sub-divided into two main categories: early and middle Miocene shallow water platform and upper slope sediments, and late Miocene periplatform sediments that are a combination of pelagic rain, platform-swept sediments, and current-shaped submarine dunes (Betzler et al., 2013; Lüdmann et al., 2013; Betzler et al., 2017). These periplatform sediments are herein referred to as drift deposits and are characterized by skeletal wackestone to rudstone containing benthic and planktonic foraminifera, lithoclasts and bioclasts (red algae, mollusk, bryozoans, Halimeda plates and aggregate grains) (Betzler et al., 2018). The shallow water platform-related facies consist of packstone, rudstone, and floatstone with abundant large benthic foraminifera, coralline red algae and rare corals.

Eleven facies were identified by Vulpe (2018) and span the depositional settings from forereef slope to reef based on the distribution of the major skeletal components and depositional texture after Dunham (1962) as modified by Embry and Klovan (1971). Grains smaller than 30 μm were considered as part of the matrix, according to Dunham (1962). The amount of each component was estimated by visual comparison charts of Flügel (1982). Abundance was described using the five terms (abundant, common, few, rare, present) after Betzler et al. (2017). These depositional facies are summarized in **Table II.2** and span the depositional settings from forereef slope to reef.

Table II.2. Summary of facies identified and criteria for their classification based on Vulpe (2018).

Facies	Characteristics	Environment
Large benthic foraminifera (LBF) grainstone	≥36% large benthic foraminifera. Variable grain sizes from fine (0.6 to 0.25mm) to coarse (0.5 to 2mm)	Forereef slope at U1465, reef pocket at U1470
LBF packstone to grainstone	≥29% large benthic foraminifera. Rare to few planktic foraminifera	Uppermost forereef slope
Dolomitized LBF packstone to grainstone	≥29% large benthic foraminifera. ≥16% benthic foraminifera. Intensively dolomitized.	Forereef slope
Benthic foraminifera floatstone	Rich in large and small benthic foraminifera. Miliolids represent about 40% of the total amount of benthic foraminifera	Upper forereef slope
Benthic foraminifera packstone	≥29% large benthic foraminifera. ≥20% benthic foraminifera. Few planktic foraminifera	Upper forereef slope
LBF floatstone to packstone	Large benthic foraminifera dominate with rare benthic and planktic foraminifera	Reef framework, possibly a reef pocket
LBF rudstone	≥53% large benthic foraminifera. Rare to few planktic foraminifera.	Reef framework, possibly a reef pocket
Foralgal floatstone	≥23% large benthic foraminifera. ≥13% red algae	Reef core
Rhodalgal rudstone	Red algae nodules and fragments dominate. Molds of green algae (*Halimeda*) common with rare large and small benthic foraminifera	Reef framework
Foralgal floatstone to rudstone	≥24% large benthic foraminifera. ≥12% benthic foraminifera ≥11% red algae	Reef core
Coral-red algae boundstone	≥27% corals. ≥17% red algae	Reef core

Dataset and Methods

Petrography

105 thin sections from Sites U1465, U1469, and U1470 sampled from 350 m of core were analyzed to describe microfacies and diagenesis using standard transmitted light microscopy and scanning electron microscopy (SEM). Petrographic images were captured with an Olympus BX53MTRF microscope using Olympus Stream Essentials 2.1 software and SEM images were captured using a Phenom XL Scanning Electron Microscope equipped with EDS detector for elemental analysis.

Total porosity and cementation were quantified using the ImageJ image processing program with the jPOR macro developed by Grove and Jerram (2011) using scanned thin sections converted to 8-bit images. Images were cropped to exclude the excess epoxy around the perimeter of the sample. Thresholds were applied to the image to select only the blue epoxy-filled pore space pixels. These pixels were compared to the total number of pixels in the image to determine porosity. Cementation was estimated by adjusting the thresholds to select the mostly white colored carbonate cements by defining upper and lower limits that captured cements across all thin sections. Visual estimations of percentage were made for cement and pore sub-types using the comparison charts for volume percentage estimation published by Bacelle and Bosellini (1965).

Stable Isotopes

165 bulk rock samples from Sites U1465, U1466, U1468, U1469 and U1470 were analyzed for $\delta^{18}O$ and $\delta^{13}C$ using a Thermo Scientific Kiel IV Automated Carbonate Device coupled to a Thermo Scientific MAT 253 dual inlet isotope ratio mass spectrometer at the Stable Isotope Geosciences Facility (SIGF) at Texas A&M University. Data are quoted relative to Vienna Pee Dee Belemnite (VPDB) with a precision of 0.04‰ for $\delta^{13}C$ and 0.06‰ for $\delta^{18}O$ based on long-term daily measurements of the carbonate standard NBS-19 ($\delta^{13}C$ = 1.95‰, $\delta^{18}O$ = -2.20‰).

Strontium Isotopes

Strontium isotope ($^{87}Sr/^{86}Sr$) analyses were performed at the R. Ken Williams '45 Radiogenic Isotope Geosciences Facility (RIGF) at Texas A&M University. 37 bulk samples from Sites U1465, U1469, and U1470 were collected approximately every 20 m downcore. Between 10 and 100 µg of powder were dissolved with 6M HCl in sealed Teflon beakers on a 90°C hot plate overnight. The HCl solution was evaporated and converted to HNO_3 solution for chemical purification on 100 µl of Sr-Spec resin. Purified solutions were loaded on outgassed Re filaments with a TaO emitter solution. Mass spectrometry was conducted on a Thermo Scientific Triton Thermal Ionization Mass Spectrometer running in static multiple-Faraday detector mode with amplifier rotation. Ion beams were in general 8-15 V of ^{87}Sr measured on 10^{10} Ω resistors. Analyses consisted of ten to twenty-five blocks of 15 two-second integrated cycles with outlier exclusion of points greater than two standard deviations from the mean. Measured isotope ratios were normalized to $^{88}Sr/^{86}Sr$ = 8.375209. Thirty-six replicate

analyses of NIST 987, conducted during sample analyses, yielded an average $^{87}Sr/^{86}Sr$ of 0.710233 and an external reproducibility of 5.3 ppm. The measured value for NIST 987 was within 0.000015 of the accepted value 0.710248, lower than other published normalization to the NIST 987 standard (McArthur et al., 2000). Internal precision of $^{87}Sr/^{86}Sr$ was better for most samples; diagrams were plotted and calculations conducted with this external reproducibility unless the internal measurement precision was greater than 5.3 ppm.

Ages are assigned using the table provided by McArthur et al. (2012) and are estimated based on the GTS2012 timescale. We know that this platform has undergone diagenesis including subaerial exposure, which has the ability to shift $^{87}Sr/^{86}Sr$ values (Fouke et al., 1996). While this approach means that asynchronous events like those observed are possible, Elderfield (1986) has shown that it is possible to use bulk strontium isotope data and obtain results that are comparable with those from unaltered material but with an alternative age control - as is presented in this article.

X-ray diffraction

Soft sediment samples were ground into fine powder using an agate mortar and pestle. Well-indurated samples were ground using a SPEX mixer mill in a stainless steel vial. Powders were analyzed by X-ray diffraction (XRD) using a Rigaku Miniflex XRD system with Co Kα radiation from 20° to 50° 2θ at 40 kV and 15 mA. Diffractograms were evaluated using the method of Milliman et al. (1974). Examination of XRD diffractograms provided data on the 2θ peak position, d-spacing, and intensities of the dolomite 104, 015, and 110 reflections as well as the calcite 104 reflection. Dolomite

composition was calculated based on the calibrated position of the dolomite 104 peak using the peak shift equation derived by (Lumsden, 1979)

Samples analyzed at Texas A&M University were supplemented by shipboard XRD data collected onboard the JOIDES Resolution. Shipboard samples were analyzed using a Bruker D-4 Endeavor diffractometer mounted with a Vantec-1 detector using nickel-filtered CuKα radiation from 20° to 40° 2θ at 40 kV and 40 mA. The percentage of minerals in samples was calculated following the methodology of Swart et al, (2002) using a Panalytical X-pert Pro X-ray diffractometer at the University of Miami since standards were not available aboard the *JOIDES Resolution*. The shipboard XRD data is available from the IODP Laboratory Information Management System (LIMS) database (http://web.iodp.tamu.edu/apps/).

Elemental analysis (Laser Ablation-ICP-MS)

Six samples from Site U1465 and three from U1470 were analyzed in polished thin sections by laser-ablation inductively coupled plasma (LA-ICPMS) methods at the RIGF Laboratory at Texas A&M University. 172 points were analyzed for six different cement types: blocky, isopachous, dogtooth, bladed, syntaxial and drusy cements, and brachiopod fragments to represent initial seawater chemistry with an LMC mineralogy. Trace element concentrations were determined using a NWR/ESI 193nm ArF excimer laser-ablation system and a ThermoScientific iCAP RQ quadrupole mass spectrometer. MACS-3 was used as the primary standard and NIST 610 as a secondary reference material . Trace element concentrations were calculated relative to MACS-3 using 43Ca

as the internal standard. Data were reduced with Iolite v.3.7 (Paton et al., 2010, 2011) and data reduction scheme "Trace Elements IS". Data tables are presented in Appendix A.

Results

Petrography

Calcite cements

Elemental analysis showed that cements are composed primarily LMC, as shown by XRD analysis (<4 mole % $MgCO_3$), and occurred in two main stages with initial bioclast-lining cements followed by pore filling cementation. Most commonly, pore lining cements are bladed prismatic 'dogtooth' with scalenohedral and elongated rhombohedral crystals (**Figure II.3D**) with sharp to blunted terminations that are between 28 μm and 118 μm in length (Reinhold, 1999). Less commonly, pore lining bladed cements occur as isopachous fringes of equal thickness or drusy equant to elongated crystals that increased in size toward the center of the pore space. These crystals are between 7 μm and 123 μm in length and normally have a clear appearance with no luminescence. No zonation was observed in any cement type under cathodoluminescence. On echinoderm fragments, initial cementation occurred as single crystal syntaxial overgrowths in optical continuity with the allochem with a typical crystal length of 71 μm (**Figure II.3D**).

Pore filling cements that either partially or completely occluded porosity (**Figure II.3A, 3C**) characterized the latter stage of cementation and contributed greatly to overall cement abundance. These late cements usually occurred as blocky crystals twith

no preferred orientation (Flügel, 2004), ranging in size from 50 μm to 144 μm. Coarse poikilotopic cements, occurring as large calcite crystals that enclose either smaller crystals or carbonate allochems, were rare pore filling cements and only observed below 208 mbsf at Site U1470.

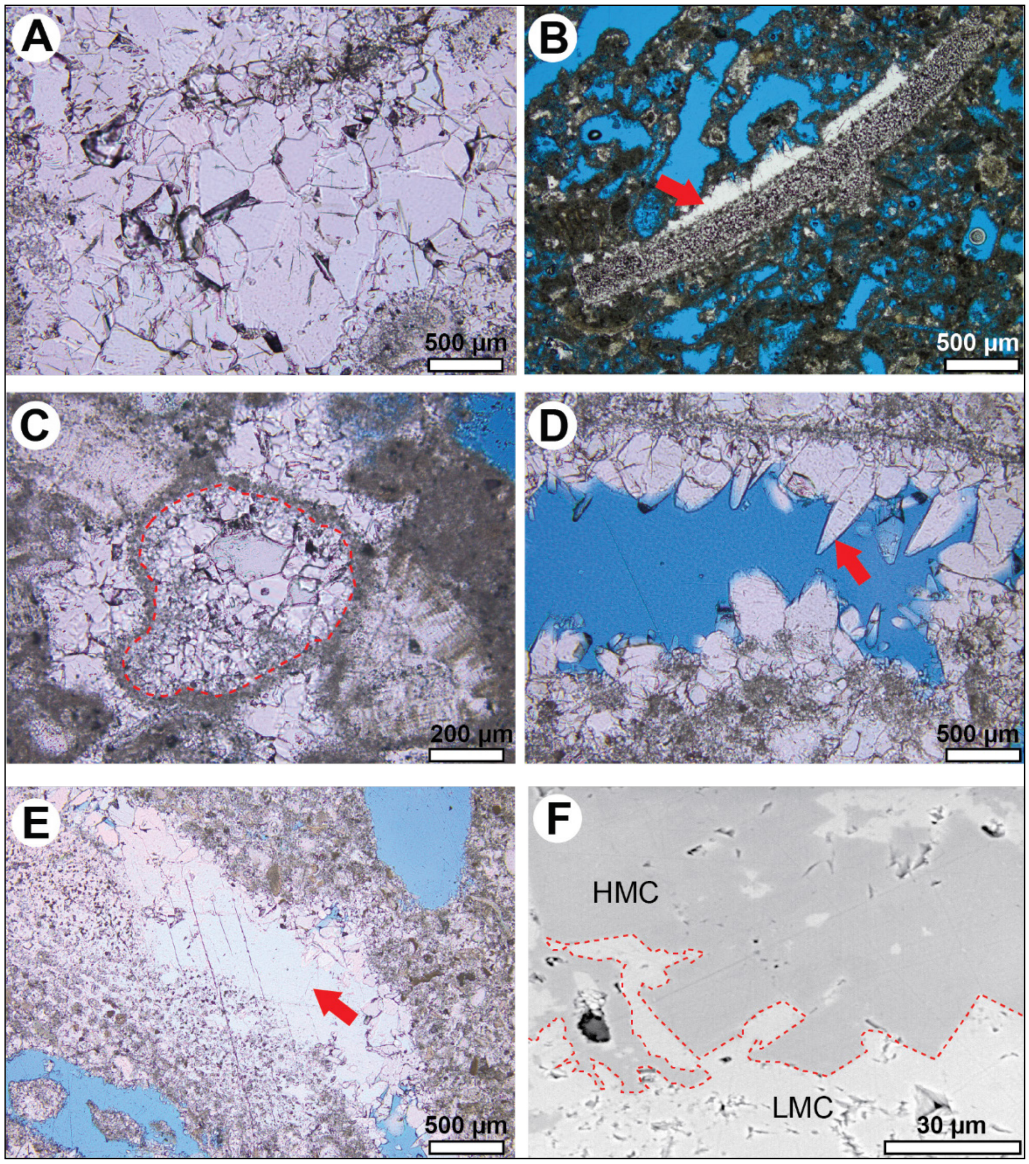

Figure II.3. Photomicrographs showing main cements described at Sites U1465, U1469 and U1470. (A) Blocky calcite spar (U1470A-18X-1W-8/10). (B) Syntaxial overgrowth on an echinoderm fragment (U1470B-6R-1W 90/93). (C) Drusy calcite cement within micrite envelope, highlighted by dashed line (U1470B-6R-1W-90/93). (D) Bladed to dogtooth calcite cement (U1470A-18X-1W-8/10). (E) Poikilotopic cement (U1470B-6R-1W 90/93). (F) Contrasting appearance of LMC and HMC cements (U1469A-4R-CCW 8/10).

Cement abundance showed the greatest variation between PS and the overlying DS deposits with cementation averaging 12% for DS sediments in contrast to an average PS cementation of 20%. Cementation averaged 19% at U1465 and 20% at U1469 but was highest at U1470 with an average of 25%. Cementation at U1470 increased below ~208 mbsf and remained high below this depth averaging 35%. At U1465, porosity and cementation were much more irregular within the PS deposits but generally increased below ~148 mbsf with an average of 21% below this depth (**Figure II.4**).

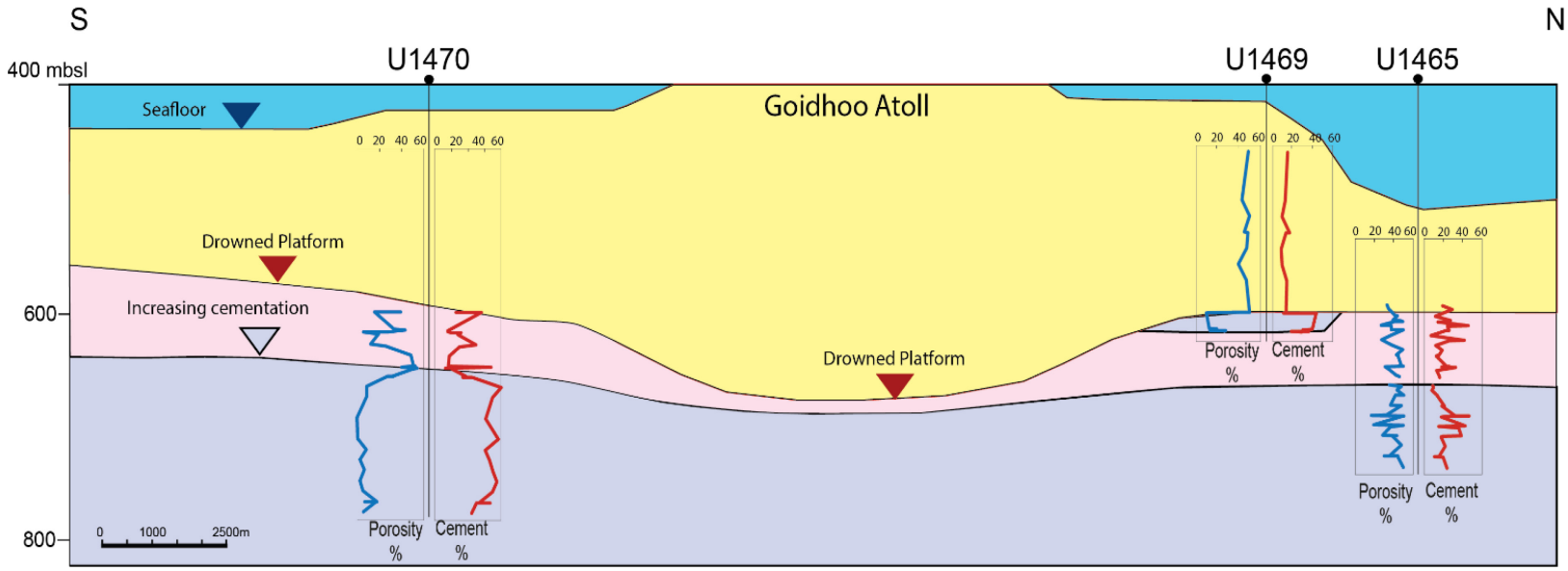

Figure II.4. S-N cross section of the platform showing cement and porosity estimates calculated using ImageJ and the JPOR plugin.

Dissolution features

Moldic pores (Choquette and Pray, 1970) are common in the PS facies and are most frequently uncemented with micrite envelopes (**Figure II.5B**). Less commonly, molds were lined by bladed, isopachous or drusy cement (**Figure II.5C**). The average pore-size is characterized as small mesopore in the sense of Choquette and Pray (1970), ranging between 0.1 mm and 2 mm in length. These pores are elongated or platy, and in some cases curvilinear with an average width: length ratio of 0.21. These molds are fabric selective most being biomoldic remnants of aragonite skeletal grains (e.g. Halimeda and gastropods).

Dissolution is common in all samples, occurring most pervasively as moldic porosity with lesser instances of interconnected vuggy porosity that is likely enlarged moldic pores. Molds account for the majority of pore types within the PS sediments, contributing an average 47% and 45% of total porosity at Sites U1465 and U1470 respectively with interparticle, intraparticle and vuggy pores contributing to the remaining porosity. Moldic porosity showed inverse trends to overall cementation, increasing below depths of 153 mbsf at U1465 and 218 mbsf at U1470, whereas overall porosity decreased below these depths. This suggests that even as overall porosity decreased, moldic pores accounted for the majority of pores present.

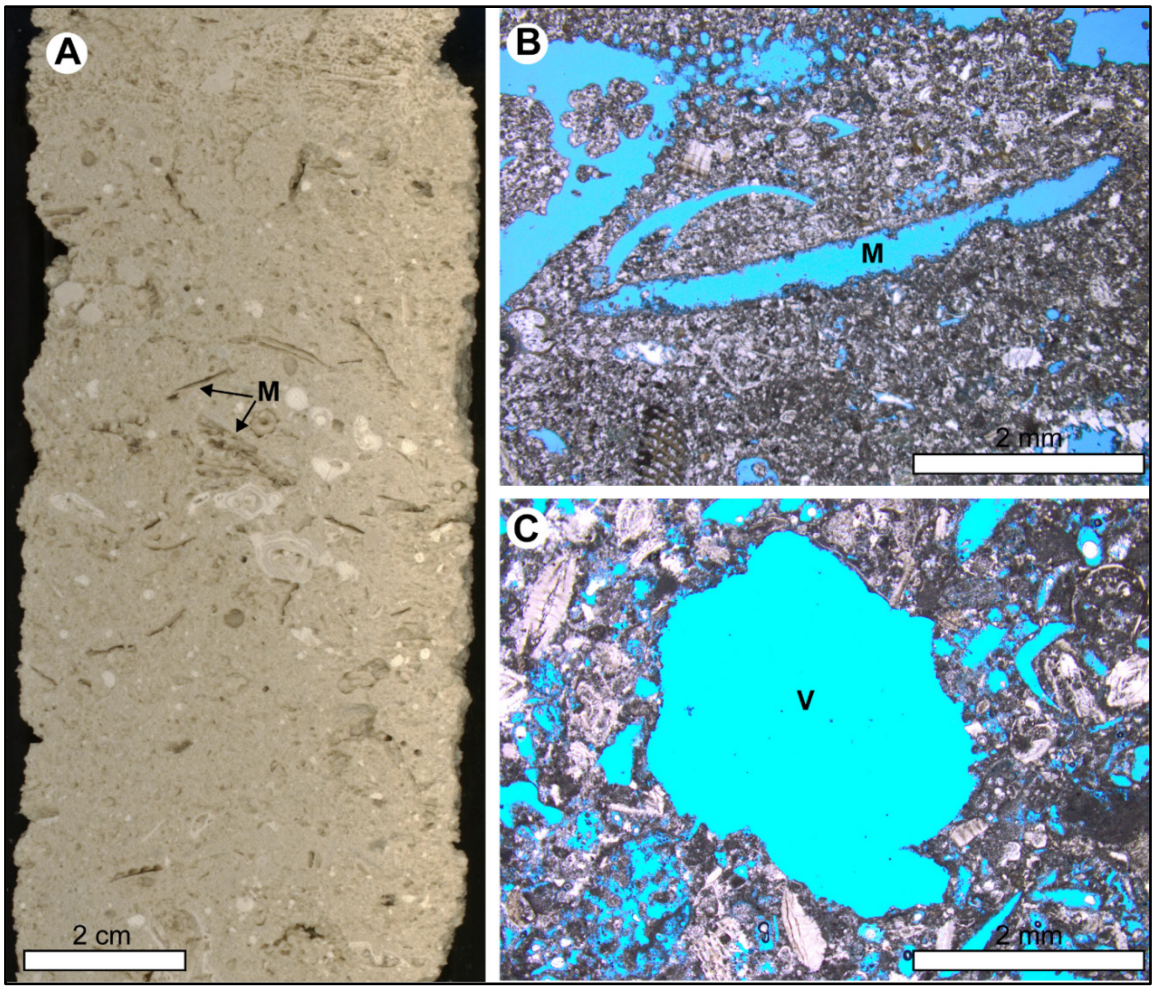

Figure II.5. Core photograph (left) and photomicrographs (right) of the pore types discussed in the text. (A) Core section photograph showing abundant moldic porosity (M) (U1470B-6R-1A-5/10). (B) Thin section showing biomoldic porosity of elongate skeletal grain (U1470B-7R-1W 49/52). (C) Thin section showing vuggy porosity (V) (U1470B-7R-1W 49/52).

Other diagenetic features

Micrite envelopes (Bathurst, 1964; Bathurst, 1966), micron sized crystals forming a thin coating about 18 μm around grains and pores, are common in PS sediments from all Sites. These micrite envelopes are relatively resistant to dissolution

and contribute to the preservation of casts of primary aragonitic skeletal grains that were dissolved to form moldic pores that are commonly unfilled (Flügel, 2004).

Dolomite occurs in varied replacement textures including fabric destructive (**Figure II.6A**) and mimetic after red algae (**Figures II.6B, 6D**). Dolomitization was most complete at Site U1469 where PS sediments are 100% dolomite below 151 mbsf. At Site U1465, dolomite was greatest at 148 mbsf, reaching 63% by volume within the ps11 sequence. Site U1470 has the least dolomite of the shallow water platform sediments with only 3% dolomite at 198 mbsf representing the greatest abundance (**Figure II.7**).

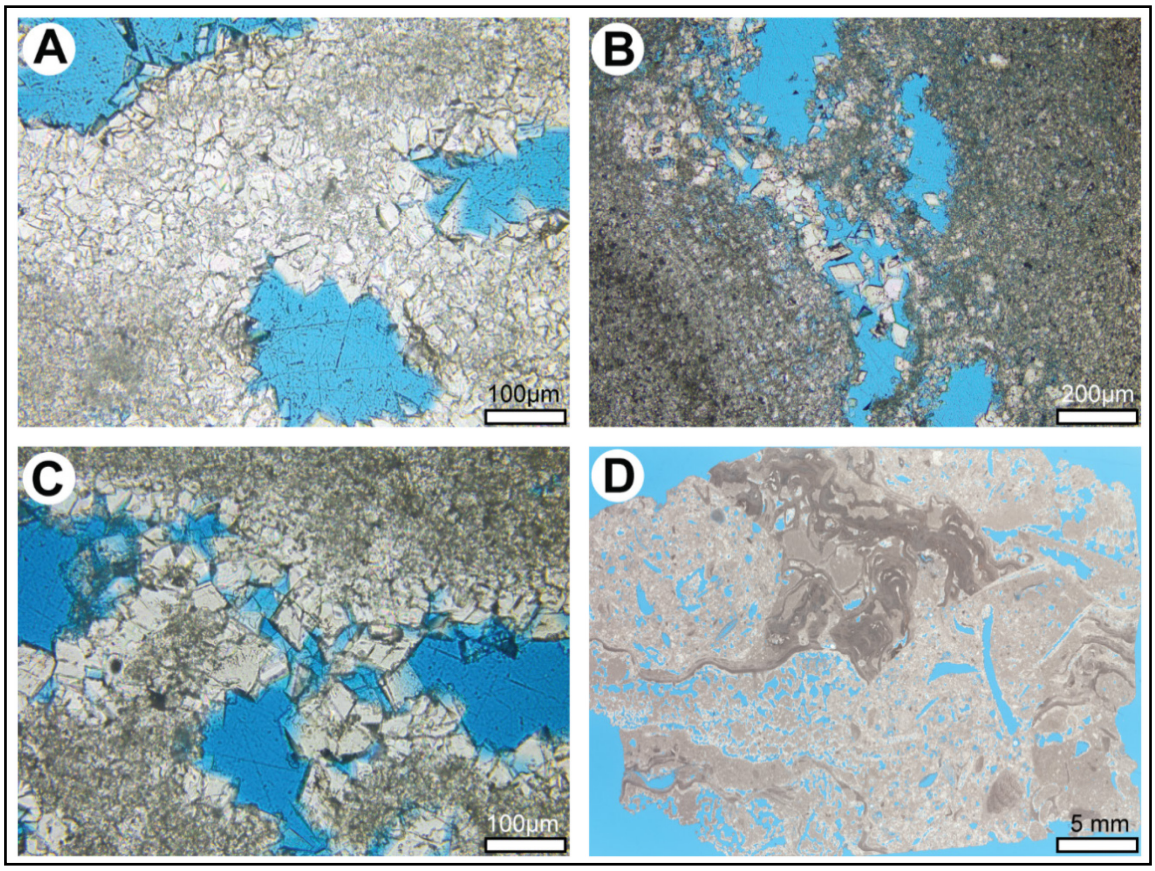

Figure II.6. Photomicrographs showing main dolomite fabrics. (A) Fabric destructive non-planar dolomite with local planar fabric replacing sediments and mostly preserving molds with some intra-moldic cements. (B) Mimetic non-planar very fine crystalline dolomite replacing red algae and planar, clear fine crystalline dolomite cements partially occluding porosity. (C) Rhombohedral dolomite growing into pore space as cement. (D) Mimetic dolomite replacement associated with coralline red algae (entire sample is dolomitized).

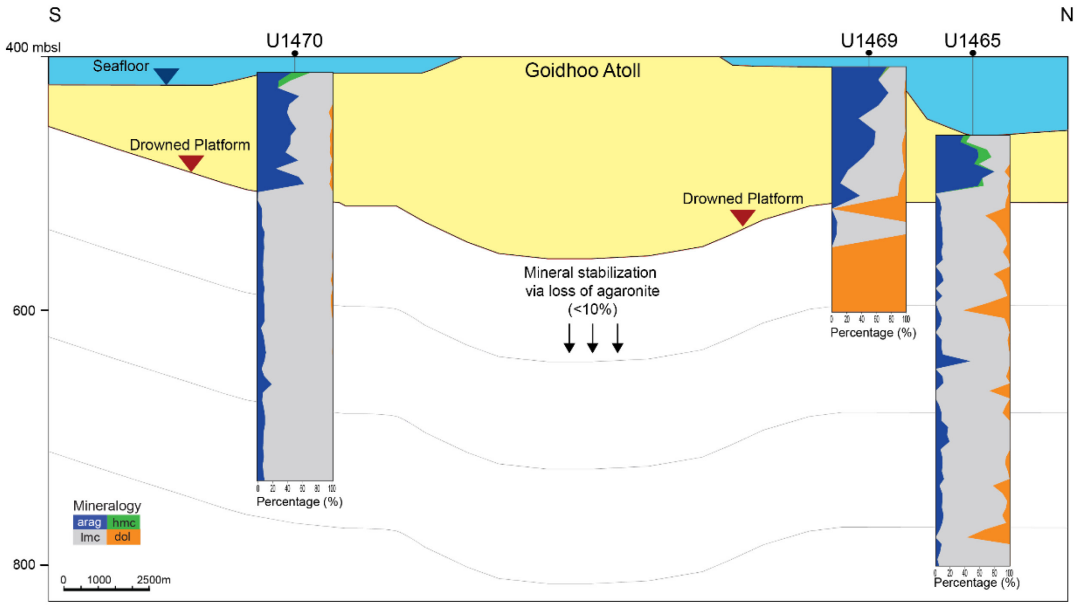

Figure II.7. S-N cross-section showing the mineralogical stabilization of the PS (white) to predominantly LMC and dolomite in contrast to the HMC and aragonite of the DS (yellow) deposits.

Elemental concentration

Mg/Ca and Sr/Ca ratios

Results of elemental concentration analysis including Sr, Ca, Na and Mg presented in **Table A.1** of Appendix A. Mg/Ca ratios are generally within the 1-5 mmol/mol expected for seawater throughout the Phanerozoic (Dickson, 2004), ranging from 0.2 mmol/mol to 8.7 µmol/mol with an average of 2.5 µmol/mol. Sr/Ca ratios are similarly low with a range of 0.006 µmol/mol to 0.02 µmol/mol with an average of 0.006 µmol/mol. Brachiopod fragments clustered tightly within a narrow range of Mg/Ca and Sr/Ca values, and plotted distinctly from the various cement types (**Figure II.8**).

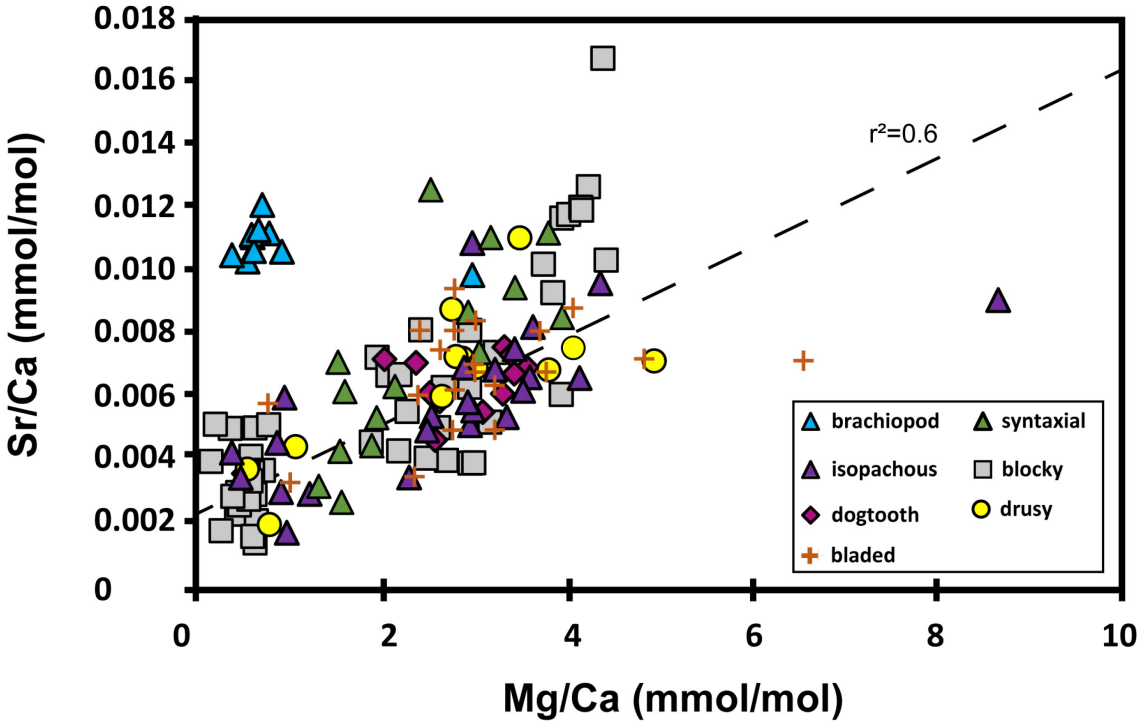

Figure II.8. Scatter plot showing Mg/Ca and Sr/Ca values for brachiopod fragments (which serve as a baseline proxy for seawater) and various cement types from Sites U1465 and U1470.

Strontium

Strontium concentrations show large variations for some individual cement types with outliers observed in both blocky and drusy cements. Skeletal allochems show the highest mean value (9.78 mmol/mol) whereas lowest values were observed in pore filling drusy cements (1.74 mmol/mol) and blocky cements (~2.9 mmol/mol). Samples from U1465 (~6.43 mmol/mol) have a higher mean concentration (**Figure II.9**) than those of U1470 (~3.11 mmol/mol).

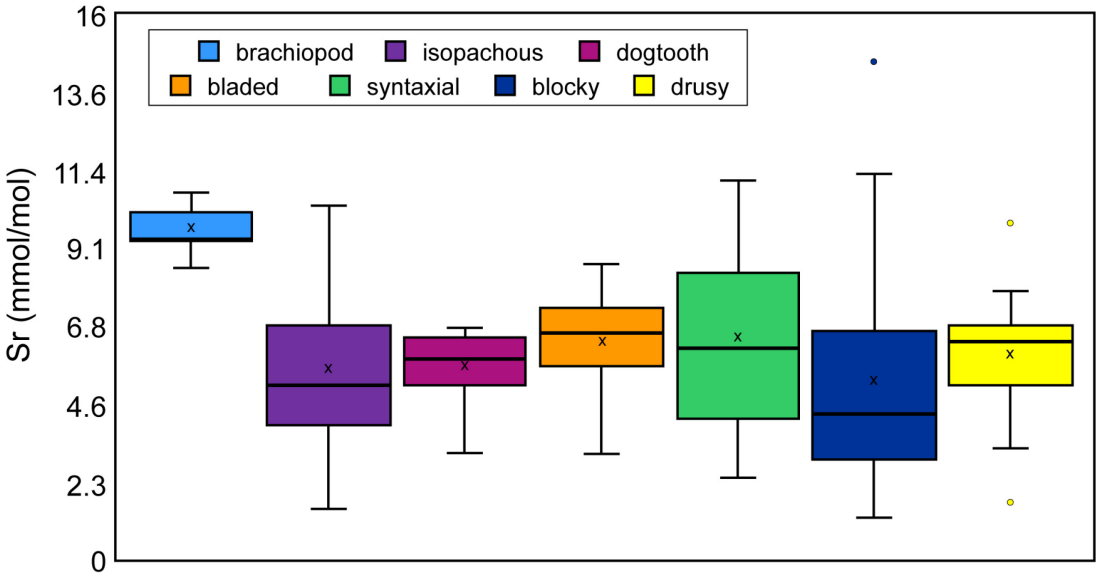

Figure II.9. Strontium concentrations of carbonate cements from Sites U1465 and U1470. The first to third quartile (box), range (thin vertical line), median (thick horizontal line) and mean (x) are shown for each cement type.

Oxygen and carbon stable isotopes

We separated the results of the stable isotopic analysis by depositional setting to illustrate the differences between the platform, slope and drift sediments. Results of O and C stable isotopes are presented in **Figure II.10** and **Table A.2** in Appendix A.

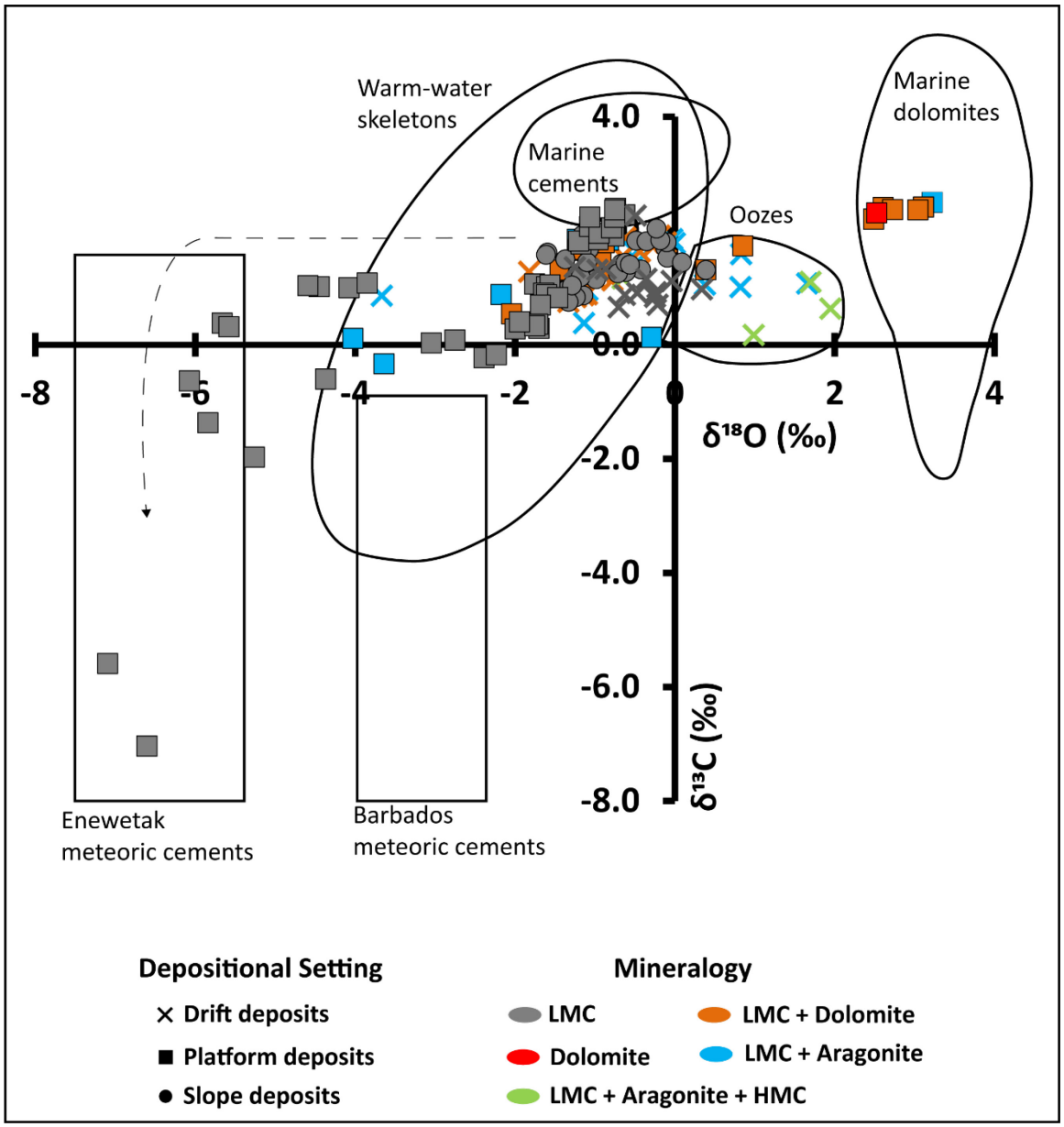

Figure II.10. Carbon and oxygen stable isotopes diagram, modified after Nelson and Smith (1996). The shapes represent depositional settings: drift (x), platform (square), and slope (circle). Colors indicate mineralogy. Data sources are as follows: Enewetak meteoric cements: Saller, 1984; Barbados meteoric cements: Matthews, 1974; marine cements: James and Choquette, 1983; pelagic oozes and warm-water skeletons: Hudson, 1977.

Platform margin

The $\delta^{18}O$ and $\delta^{13}C$ values for PS sediments plot mostly within the range expected for warm-water skeletons with U1465 and U1470 PS sediments contributing almost exclusively to this field (**Figure II.11**). $\delta^{18}O$ values vary between -4.4‰ to -0.7‰ and $\delta^{13}C$ between -0.6‰ to 2.4‰. The next most populous cluster for PS sediments occurs from -7‰ to -4‰ for $\delta^{18}O$ and -7‰ to 1‰ for $\delta^{13}C$ with some values falling in the range of Enewetak meteoric cements (Saller, 1984). Most occurrences of dolomite had positive $\delta^{18}O$ values between 2.5‰ to 3.2‰ and $\delta^{13}C$ between 2.2‰ to 2.5‰, plotting in the "marine dolomite' field of Nelson and Smith (1996). This field also overlaps significantly with the evaporative dolomite field (Nelson and Smith, 1996). The partially dolomitized samples with negative $\delta^{18}O$ values were all contained in the warm-water skeletons field.

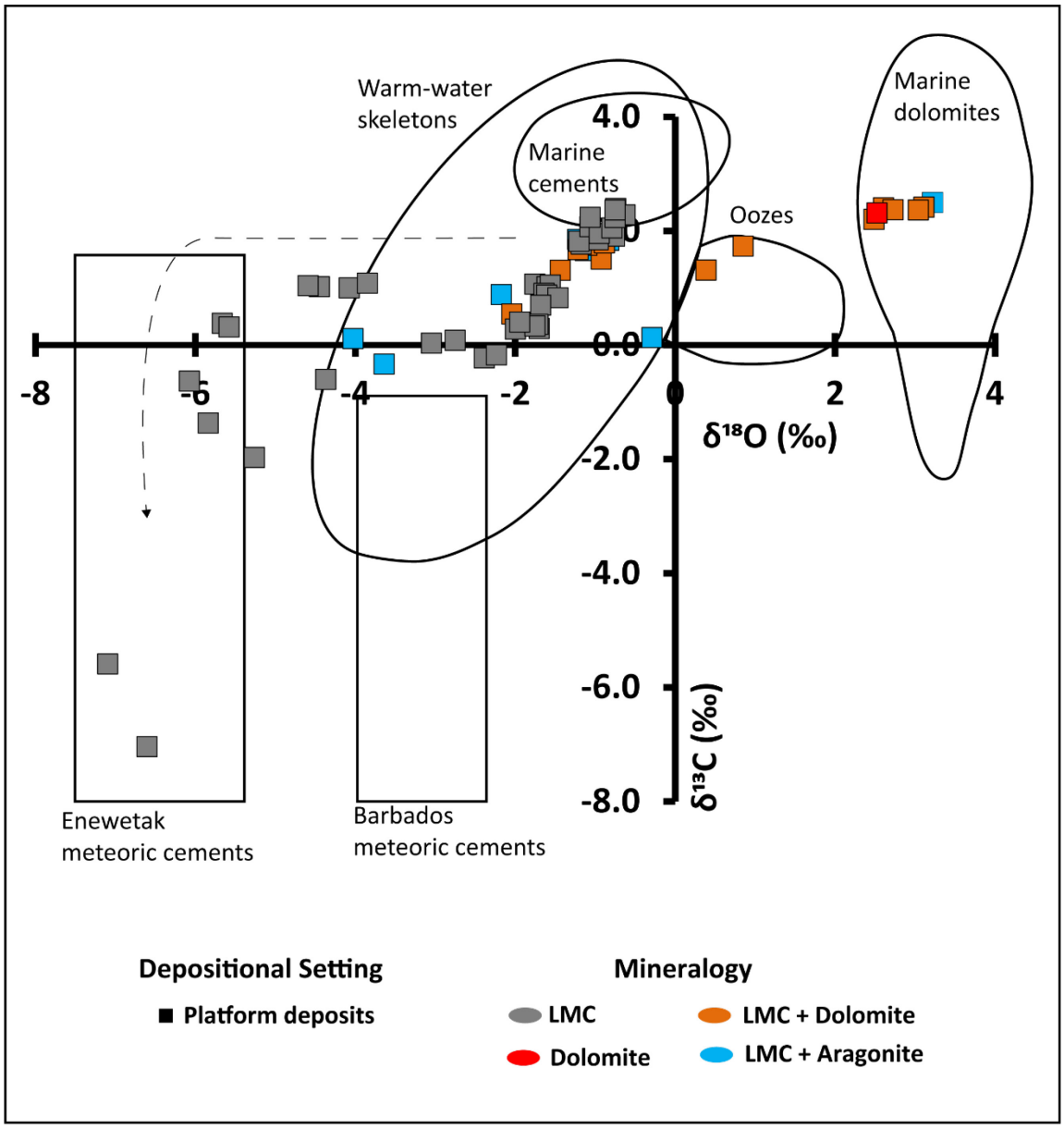

Figure II.11. Carbon and oxygen stable isotopes for PS sediments

Slope and drift deposits

Sediments from the slope facies (SL) are all from Site U1466 and, with the exception of a single sample, cluster within the warm-water skeletons field (**Figure II.12**). They have $\delta^{18}O$ between 0.4‰ to -1.6‰ and $\delta^{13}C$ between 0.3‰ to 2.3‰. This field is defined as modern marine skeletons (dominantly bryozoans and bivalves) from mainly shelf water depths (Nelson and Smith, 1996).

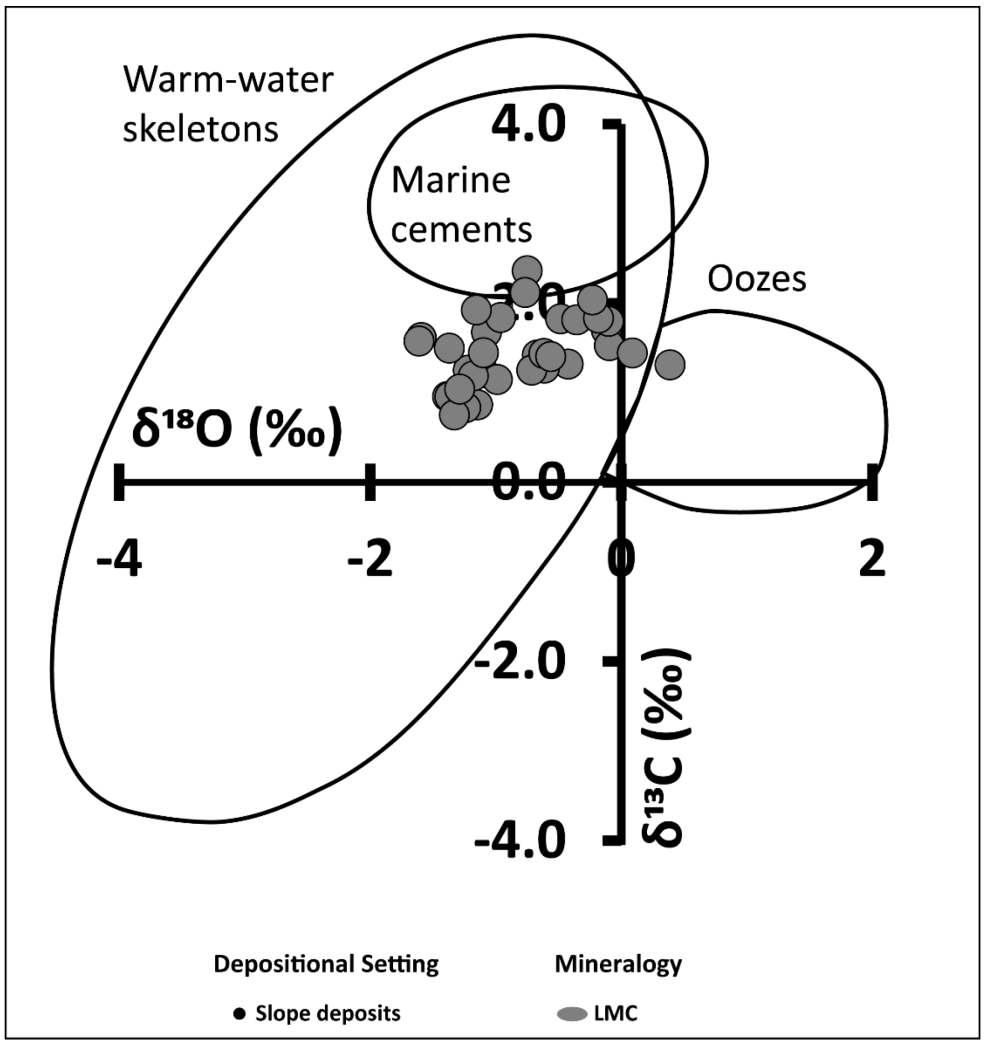

Figure II.12. Carbon and oxygen stable isotopes for SL sediments

Most drift facies (DS) samples (Sites U1465, U1466, U1468, and U1470) plot within the warm water skeleton field (**Figure II.13**) with $\delta^{18}O$ values from -3.7‰ to -0.1‰ and $\delta^{13}C$ between 0.4‰ and 2.7‰. 16 of 17 samples from Site U1469 plot in the pelagic ooze field, which overlaps, with the warm-water skeleton field observed for samples from U1468. The pelagic ooze field samples values range between 0.4‰ and 1.9‰ for $\delta^{18}O$ and from 0.2‰ to 1.6‰ for $\delta^{13}C$.

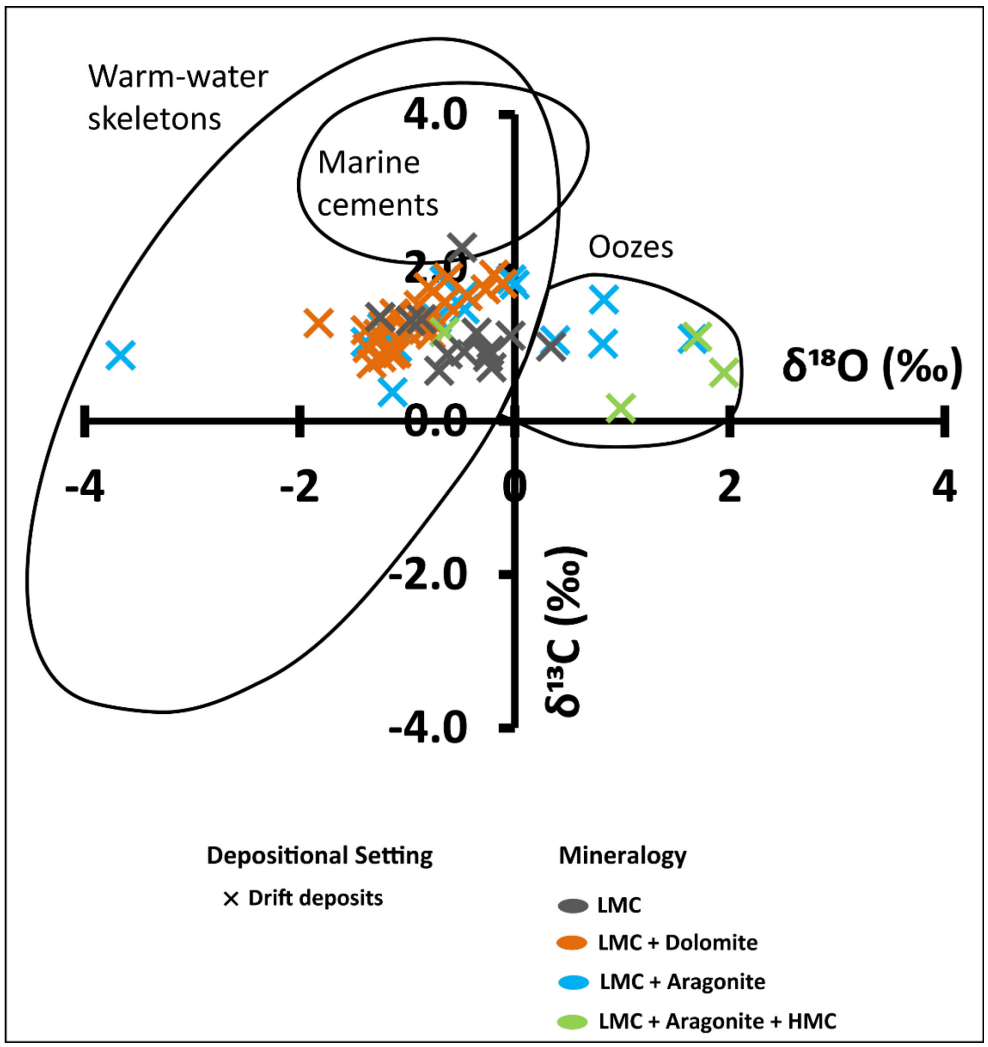

Figure II.13. Carbon and oxygen stable isotopes for DS sediments.

Strontium isotopes

The $^{87}Sr/^{86}Sr$ isotope values vary between 0.7087 and 0.7091 in all samples. The PS samples vary from 0.7085 to 0.7089 whereas the DS samples vary from 0.7087 to 0.7091 (**Table II.3**). The obtained ages show an expected coherent trend, increasing with increases in depth and likely record values of contemporaneous seawater and thus depositional ages. Some dolomitized samples show higher $^{87}Sr/^{86}Sr$ isotope values than surrounding sediments and likely reflect an average timing of dolomitization.

Table II.3. Strontium isotope analyses of bulk rock samples from Sites U1465, U1466, U1469, and U1470. Ages are assigned using the table provided by McArthur et al. (2012) and are estimated based on the GTS2012 timescale. (A=aragonite; LMC = low Mg-calcite; D = dolomite), in order of abundance. Sample nomenclature follows standard IODP naming procedure: For example, a sample identification of "U1466A-37X-1W 124/126," represents a sample taken from the interval between 124 and 126 cm below the top of Section 1 of Core 37 of Hole A of Site U1466. The 'X' after 37 denotes that the core was retrieved using the 'extended rotary core barrel coring system'. The 'W' denotes the sample was taken out of the working half of the core section. CC: core catcher (Betzler et al., 2017).

Sample Name	Depth (mbsf)	Depositional Sequence	Sample Mineralogy	Sr (ppm)	$^{87}Sr/^{86}Sr \pm 2\sigma$	Age (Ma)	Min (Ma)	Max (Ma)
U1466A-37X-1W 124/126	231.84	DS 1	LMC, D, A	1971	0.70882695	12.6	12.35	12.8
U1466A-40F-2W 11/14	259.71	DS 1	LMC, A	1433	0.70883426	12.15	11.95	12.4
U1466A-42F-3W 83/85	271.33	DS 1	LMC, A, D	1299	0.70883613	12.05	11.8	12.3
U1466A-47F-1W 100/104	307.3	DS 1	LMC, A	1379	0.70892653	8.3	8.05	8.55
U1469B-4R-CCW 3/5	141.63	DS 1	LMC, A	945	0.70892749	8.25	8	8.5
U1470B-7R-1W 49/52	217.89	DS 1	LMC, A	545	0.70887094	10.5	10.35	10.65
U1470A-20F-CCW 3/4	164.67	DS 2	LMC	601	0.70876409	15.4	15.35	15.45
U1470A-24X-1W 7/9	180.38	DS 2	LMC, D	300	0.70914252	0.9	0.85	0.95
U1470B-5R-2W 84/86	200.32	DS 2	LMC, D	380	0.70874359	15.75	15.7	15.8
U1470A-16H-4W 8/10	139.68	DS 6	LMC, A, D	1875	0.70900040	5.8	5.75	5.85
U1465B-19R-1W 13/16	172.73	PS 10	LMC, A	934	0.70879240	14.85	14.7	14.9
U1465B-21R-1W 10/13	192.2	PS 10	LMC	523	0.70878914	14.95	14.85	15.05
U1465B-23R-1W 29/31	211.89	PS 10	LMC, A	771	0.70881832	13.05	12.85	13.3

Table II.3. Continued

Sample Name	Depth (mbsf)	Depositional Sequence	Sample Mineralogy	Sr (ppm)	$^{87}Sr/^{86}Sr \pm 2\sigma$	Age (Ma)	Min (Ma)	Max (Ma)
U1465C-26X-1W 4/6	223.44	-	LMC, A	-	0.70881046	13.6	13.3	14.1
U1466B-5R-1W 58/61	343.68	PS 10	LMC	856	0.70880602	14.1	13.6	14.5
U1466B-7R-1W 62/64	363.12	PS 10	LMC	969	0.70878663	15	14.9	15.1
U1466B-9R-1W 60/63	382.6	PS 10	LMC	879	0.70879851	14.65	14.45	14.8
U1470B-18R-1W 5/8	324.35	PS 10	LMC	545	0.70878413	15.05	14.95	15.15
U1470B-19R-CCW 1/3	334.01	PS 10	LMC	654	0.70876873	15.35	15.3	15.4
U1465A-11X-CCW 34/36	69.44	PS 11	LMC, D	1481	0.70882274	12.8	12.6	13
U1465B-6R-1W 2/5	90.02	PS 11	LMC, D	498	0.70880893	13.75	13.4	14.2
U1465C-12X-1W 3/6	109.33	PS 11	LMC, D	654	0.70882878	12.5	12.25	12.75
U1465B-12R-1W 1/3	128.81	PS 11	LMC, D	333	0.70881071	13.55	13.25	14.05
U1466B-3R-1W 125/128	324.85	PS 11	LMC	1061	0.70887893	10.2	10.05	10.35
U1470B-10R-CCW 7/10	246.57	PS 11	LMC, A	1710	0.70880910	13.7	13.4	14.2
U1470B-12R-CCW 3/5	265.93	PS 11	LMC, A	-	0.70881446	13.3	13.05	13.6
U1470B-14R-CCW 5/7	285.45	PS 11	LMC	429	0.70878520	15.05	14.95	15.15
U1470B-16R-CCW 3/5	304.83	PS 11	LMC	855	0.70877458	15.25	15.2	15.3
U1466B-39R-1W 101/105	635.41	PS 4	LMC	540	0.70854404	18.35	18.25	18.45
U1466B-40R-1W 44/48	644.54	PS 4	LMC	444	0.70853573	18.45	18.35	18.55
U1466B-42R-1W 45/49	663.95	PS 4	LMC	445	0.70851287	18.7	18.6	18.8

Table II.3. Continued

Sample Name	Depth (mbsf)	Depositional Sequence	Sample Mineralogy	Sr (ppm)	$^{87}Sr/^{86}Sr \pm 2\sigma$	Age (Ma)	Min (Ma)	Max (Ma)
U1466B-34R-1W 95/98	586.85	PS 5	LMC	573	0.70864917	17.05	17	17.1
U1466B-29R-1W 50/54	542.6	PS 6	LMC	951	0.70867808	16.65	16.6	16.7
U1466B-32R-1W 51/56	567.01	PS 6	LMC	881	0.70862927	17.3	17.25	17.35
U1466B-15R-1W 38/41	440.58	PS 7	LMC	1249	0.70879022	14.9	14.8	15
U1466B-11R-2W 30/33	402.65	PS 8	LMC	942	0.70879849	14.65	14.45	14.8
U1466B-13R-1W 81/84	421.61	PS 8	LMC	1005	0.70885556	11.1	10.9	11.3

Discussion

Age control

The strontium isotope values correspond to the middle Miocene to late Pleistocene epochs. Samples show a reasonable age distribution with those from younger deposits generally yielding younger $^{87}Sr/^{86}Sr$ ages. Our confidence in the ages obtained from $^{87}Sr/^{86}Sr$ is bolstered by good agreement with the age model obtained from shipboard biostratigraphy (**Figure II.14**) which utilized planktonic foraminifera and calcareous nannofossils (Betzler et al., 2017). There are some instances where $^{87}Sr/^{86}Sr$ isotopes yield asynchronous ages (**Figure II.15**). These instances of younger ages that are out of phase with depth are attributed to episodes of dolomitization which may have reset strontium composition, as seen at 180 mbsf in U1470, and previously documented in the Marion Plateau (Ehrenberg et al., 2006).

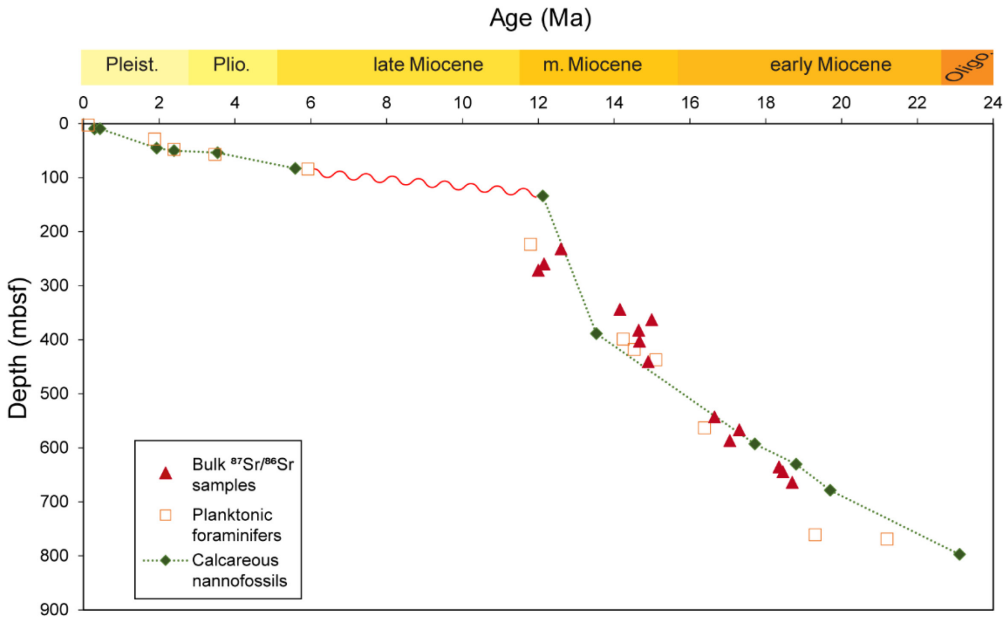

Figure II.14. Age-depth plot for Site U1466. Ages obtained from bulk strontium isotope ratios are compared with Expedition 359 shipboard biostratigraphic model (Betzler et al., 2017).

Mineralogical stabilization

The original sediments of the Maldives' platform succession contained significant amounts of aragonite and HMC based on the dominant skeletal fragments (e.g. foraminifera, echinoderms, bivalves) and the prevalence of these minerals in the younger, less altered sediments of the drift deposits. Stabilization of those metastable minerals to LMC proceeds via dissolution-reprecipitation reactions in meteoric (Veizer, 1977; James and Choquette, 1984) mixing zone (Budd, 1988; Melim et al., 2004) and marine waters (Schlager and James, 1978; Dix and Mullins, 1992) driven by differences in the solubility of these carbonate phases.

The abrupt nature of the mineralogical change from aragonite (with less HMC) to LMC between the drift and the underlying platform deposits (**Figure II.7**) suggests that the influence of meteoric water during the sea-level dominated platform regime was a significant factor to the stabilization of these polymorphs. It is likely that this stabilization involved meteoric fluids as it is accompanied by dissolution resulting in pervasive moldic porosity, which is a common feature in the meteoric environment (Choquette and Pray, 1970; James and Choquette, 1984; Pierson and Shinn, 1985). It is likely that the total sum of these mineralogical changes are the result of multiple cumulative periods of subaerial exposure and resultant changes in the position of the water table.

While the presence of drusy and blocky LMC cements along with micritization are typically associated to subaerial exposure (James and Choquette, 1983), they have also been interpreted from marine settings (e.g., Melim et al., 1995, 2001, 2002). In the Maldives, the interpretation for marine stabilization of mineralogy is supported by the geochemistry of the cements. In this study, our data (**Figure II.8**) show that those cements are clearly different than well-preserved brachiopod fragments which represent the baseline for comparison (seawater composition). This would indicate that these cements were mediated in fluids other than seawater, and based on the geographic setting of the Maldives, meteoric fluids.

In addition, while mean strontium concentration at Site U1465 is higher than at U1470, they both are within the modal range of calcite cements from the Enewetak, Cat Island and Yucatan platforms where meteoric diagenesis is well-documented (Lohmann, 1988;

Quinn, 1991; Saller, 1992). Mg/Ca ratios are indicative of freshwater alteration as the mean is well below the ~4.5 mmol/mol expected for seawater in the Miocene with 96% of cement samples below this value (Dickson, 2004).

Subaerial exposure and the freshwater phreatic zone

The inverted "J" pattern that occurs in the Kardiva platform samples is indicative of diagenetic alteration by variable degrees of freshwater fluids (Lohmann, 1988). In other words, this pattern is characteristic of meteoric diagenesis (Allan and Matthews, 1977, 1982). This isotopic characteristic is observed at Site U1470 between 265 and 295 mbsf with negative values of $\delta^{18}O$ (-7.1‰) and $\delta^{13}C$ (-7.0‰) (**Figure II.15**, **Figure II.16**). The very negative carbon values indicate the input of soil-zone derived CO_2 and the low $\delta^{18}O$ values in the horizons above and below indicate that warm meteoric waters drove diagenesis in the interval from 218 to 334 mbsf. The development of soils is characteristic of intense rainfall and wet conditions in tropical areas, which contributes to terrestrial vegetation on the incipient islands. This indicates that the exposure was long enough to develop significant soil and vegetation cover. The dates obtained using $^{87}Sr/^{86}Sr$ ratios (**Figure II.15**) suggest that the strata bounding the uppermost part of the exposed zone at U1470 are approximately 15 My old. This is comparable with the platform sequence ps10 of Betzler et al., (2013) that coincides with a period of large fluctuations (>50 m) of sea level between 14.5 and 16.5 Ma (Flower and Kennett, 1993).

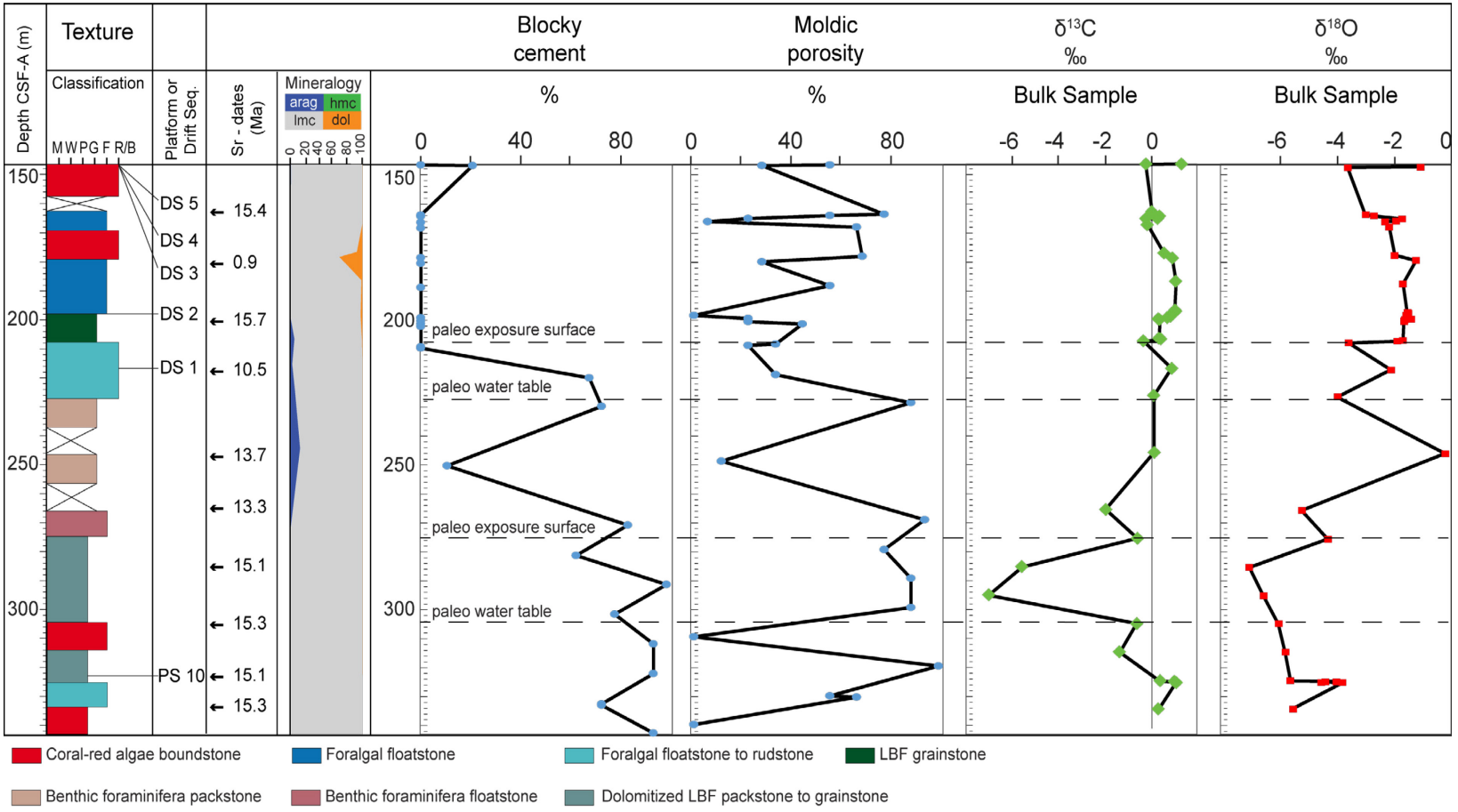

Figure II.15. Site U1470 stratigraphy, physical and geochemical measurements showing positions of two paleo exposure surfaces and water table couplets. Position of the exposure surface interpreted from $\delta^{18}O$ values ≤ -4‰, water table interpreted from blocky cement maxima beneath exposure surface.

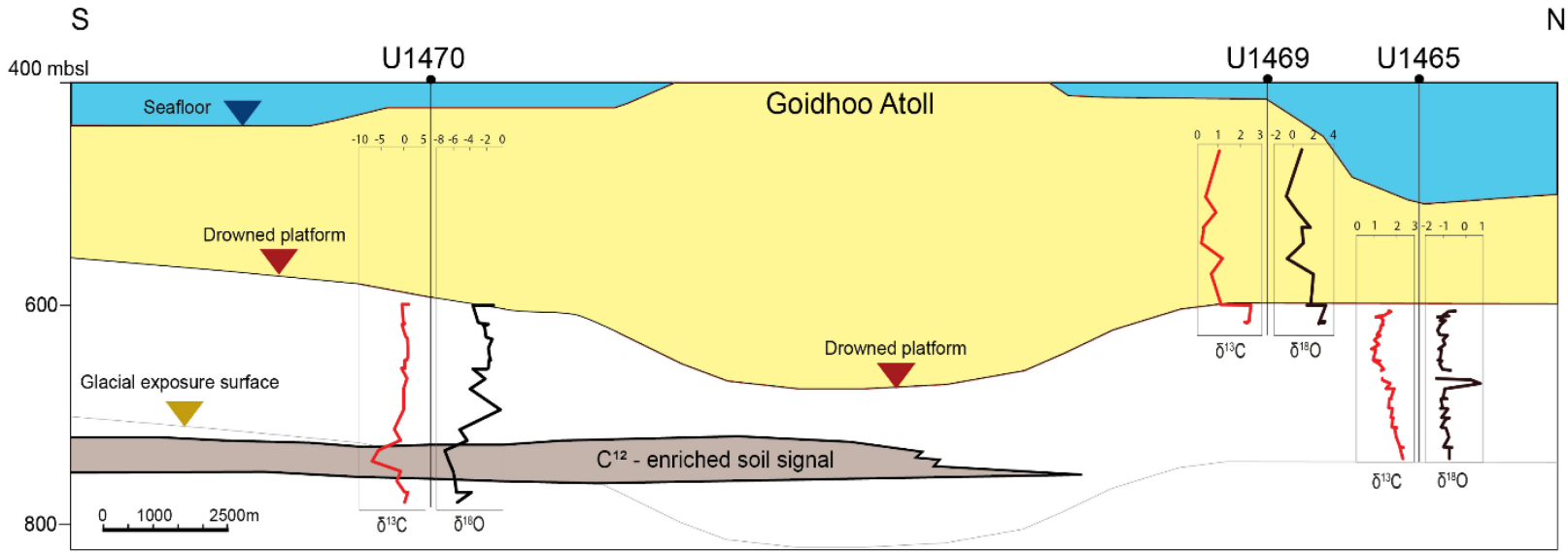

Figure II.16. S-N cross-section showing the stable isotope values and inferred zone of exposure and ^{12}C- enriched soil signal associated with EAIS glaciation.

At Site U1465, the diagenetic history is less clear, likely due to the occurrence of more diagenetically active processes (e.g. dolomitization) (**Figure II.17**) that may have overprinted the earlier diagenetic stages (Sheppard and Schwarcz, 1970; Land, 1980). This offsetting of stable isotope values makes the detection of paleo exposure surfaces and their water table couplets less obvious but if a correction for the fractionation is applied to account for the enrichment of dolomite (+3‰ and +1‰ for $\delta^{18}O$ and $\delta^{13}C$ respectively), the meteoric influence becomes evident (Land, 1983; Vasconcelos et al., 1995). Even when this correction is applied, the $\delta^{13}C$ values at U1465 are more positive than those at the southern margin with no distinctive ^{12}C- depleted soil gas signature seen at ~300 mbsf in U1470 (**Figure II.18**). Only a narrow zone at or near the subaerial exposure surface typically preserves this highly negative signal whereas the near-surface freshwater phreatic environment is capable of producing positive $\delta^{13}C$ values (Allan and Matthews, 1977).

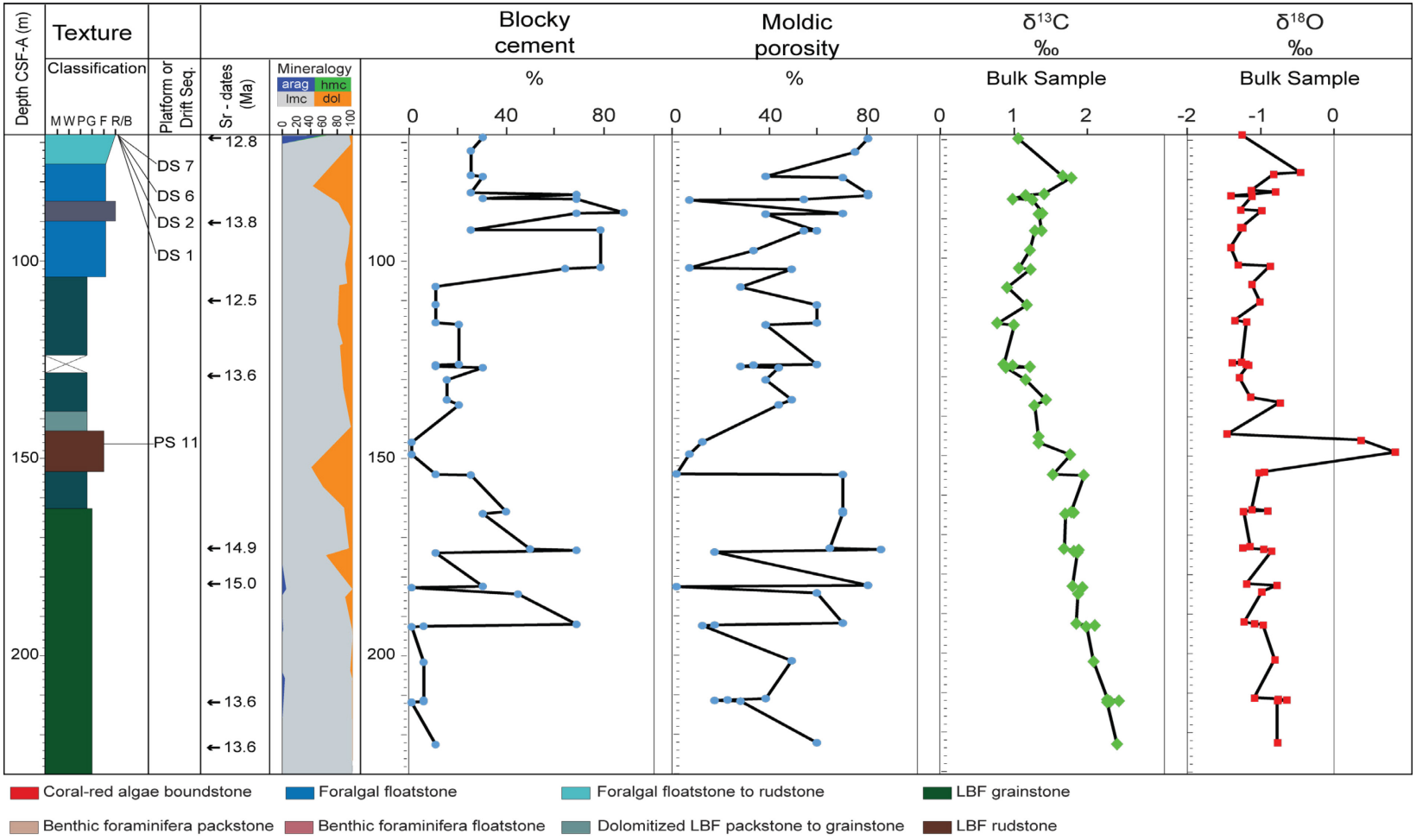

Figure II.17. Site U1465 stratigraphy, physical and geochemical measurements.

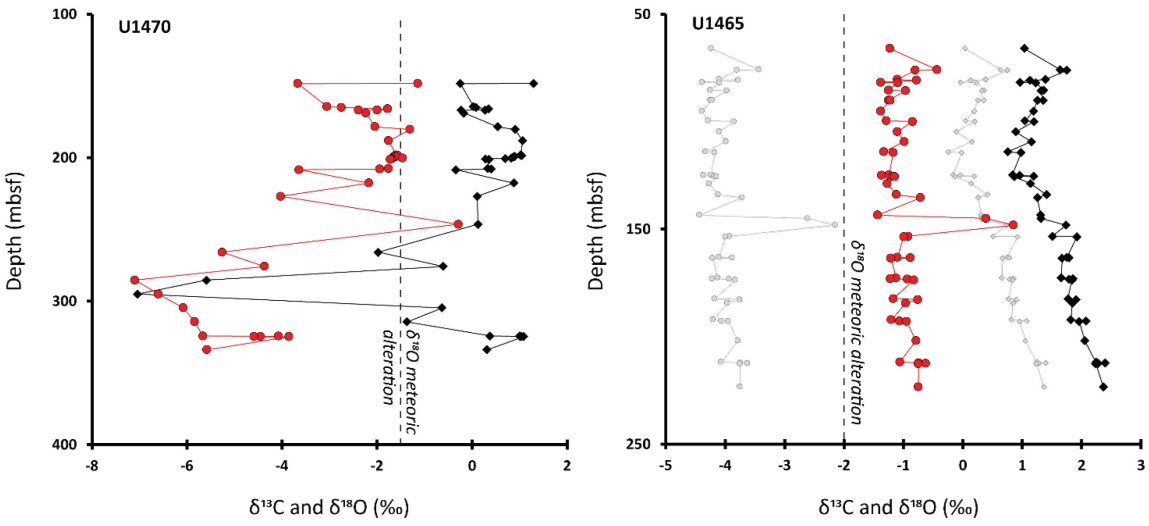

Figure II.18. The $\delta^{18}O$ (red circles) and $\delta^{13}C$ (black diamonds) values of bulk sediments from U1470 and U1465. The $\delta^{18}O$ (grey circles) and $\delta^{13}C$ (grey diamonds) represent a correction for the positive enrichment of $\delta^{18}O$ and $\delta^{13}C$ by 3‰ and 1‰ respectively (Land, 1983; Vasconcelos et al., 1995)

The difference in elevation (35 m) between Sites U1470 and U1465 could account for the difference in $\delta^{13}C$. Most infiltration of water through the vadose zone does not occur directly above the reservoir instead, 99% of infiltration occurs in areas with higher relief with water then flowing laterally along a hydrologic gradient (Harris, 1971). If the southern transect was the main area for aquifer recharge, freshwater would flow north toward U1465 becoming enriched in $\delta^{13}C$ as it flows. This enrichment is the result of freshwater becoming supersaturated with respect to calcite, continuously dissolving metastable carbonate and reprecipitating LMC. Over a 2 km wide phreatic lens in Barbados, this process has resulted in a 2‰ positive shift in $\delta^{13}C$, and with a greater distance, this shift would be more pronounced and move values closer to that of marine sediments, as observed at U1465 (**Figure II.18**) (Harris, 1971).

While the magnitude of sea-level fall would delineate the top of the freshwater lens, the phreatic zone actually extends well below this surface. Extensive studies of modern islands have yielded a model for estimating the thickness of the phreatic zone based on the width of the island, the ratio between the amount of recharge and hydraulic conductivity (Budd and Vacher, 1991). This H/a method (where H is the thickness of the freshwater lens and a is the width of the platform) results in ratios that range from 0.2% to 2% with 1% being the most representative value. If we use 1% as the ratio between the width of the lens and platform, (assuming the width of platform from the western to eastern margin be ~18.6 km) then the freshwater lense on the Kardiva platform would be about 186 m thick (**Figure II.19**). This H/a method for estimating the thickness of the freshwater lense is preferred to the Ghyben-Herzberg rule (H = 40 times the elevation of the water table) because it does not require the estimation of the paleo water table and sea level to within centimeters.

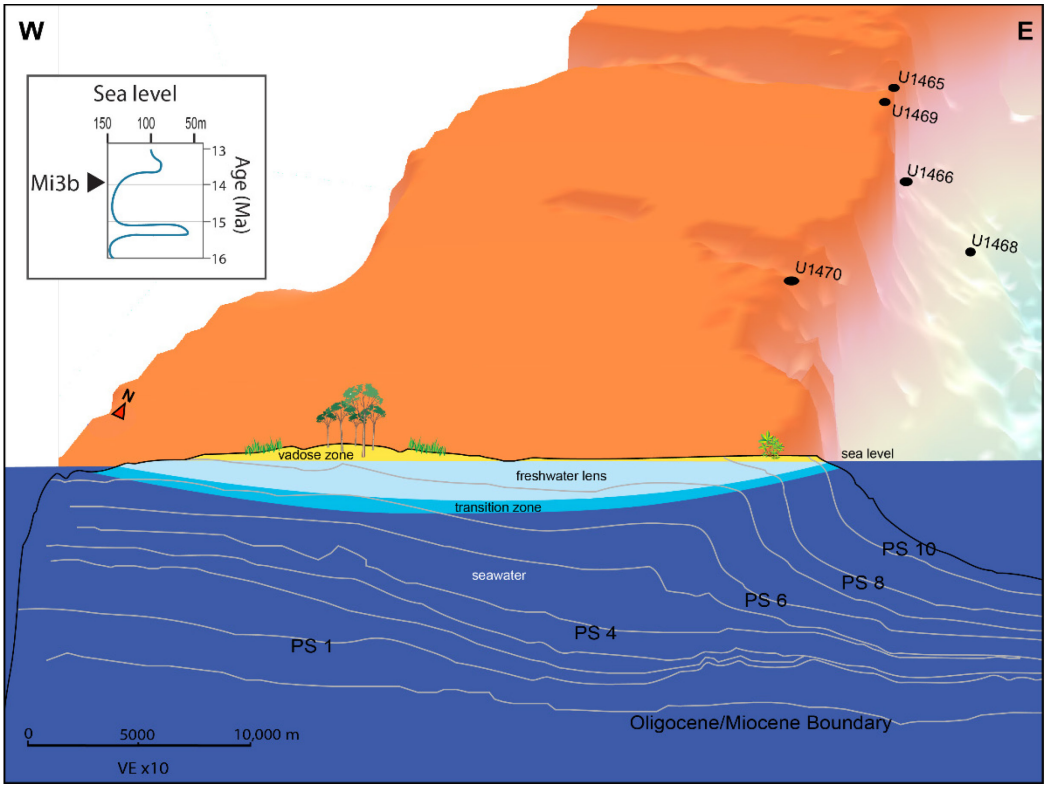

Figure II.19. Model showing the distribution and calculated extent of the water table. Generalized 2D cross section of the northern transect showing platform sequence (PS) boundaries is modified from Betzler et al. (2018) and Lüdmann et al. (2018). Global sea-level curve is from Haq et al. (1987).

During the exposure of the platform around 14.3 Ma, as evidenced by the soil $\delta^{13}C$ values at U1470, freshwater would have penetrated to a depth of 486 mbsf. This depth of penetration is more than double the width of the investigated interval at U1465 (66 mbsf to 223 mbsf) making it likely that most of the sediments at U1465 were in the freshwater phreatic zone.

Middle Miocene glacio-eustacy and climatic influence on low latitude areas

The middle Miocene marks a major change in the climatic evolution of the Cenozoic. Following the Middle Miocene Climate Optimum, the warmest period of the Neogene (Holbourn et al., 2015), there was a period of rapid cooling that produced a permanent decrease in Cenozoic temperature from ~14.8 to 14.1 Ma (Flower and Kennett, 1994), and continued up to 13.7 Ma (**Figure II.20**), during the Middle Miocene Climate Transition (Flower and Kennett, 1994; Mourik et al., 2011; Holbourn et al., 2015).

Initial growth of the EAIS near the Eocene/Oligocene boundary, was attributed to a decline in atmospheric CO_2 allowing for the development of small ice sheets as the snowline lowered in the Transantarctic Mountains (Drewry, 1975; DeConto and Pollard, 2003). Tectonics and resulting changes in ocean circulation likely played some part in the development on the Antarctic cryosphere as the tectonic opening of the Tasmanian and Drake passages resulted in the development of the Antarctic Circumpolar Current (ACC), which acted to thermally isolate Antarctica by reducing southward oceanic heat transport (DeConto and Pollard, 2003). Finally, the development of the EAIS likely accounts for the high amplitude sea-level variations between ~ 16 and 14 Ma and marks the middle Miocene with two sea-level falls between ~14 and 12.5 Ma (Haq et al., 1987). The exposure surface at approximately 275 mbsf at Site U1470 is likely between 13 and 15 Ma, within the range of the first and second growth phases of the EAIS.

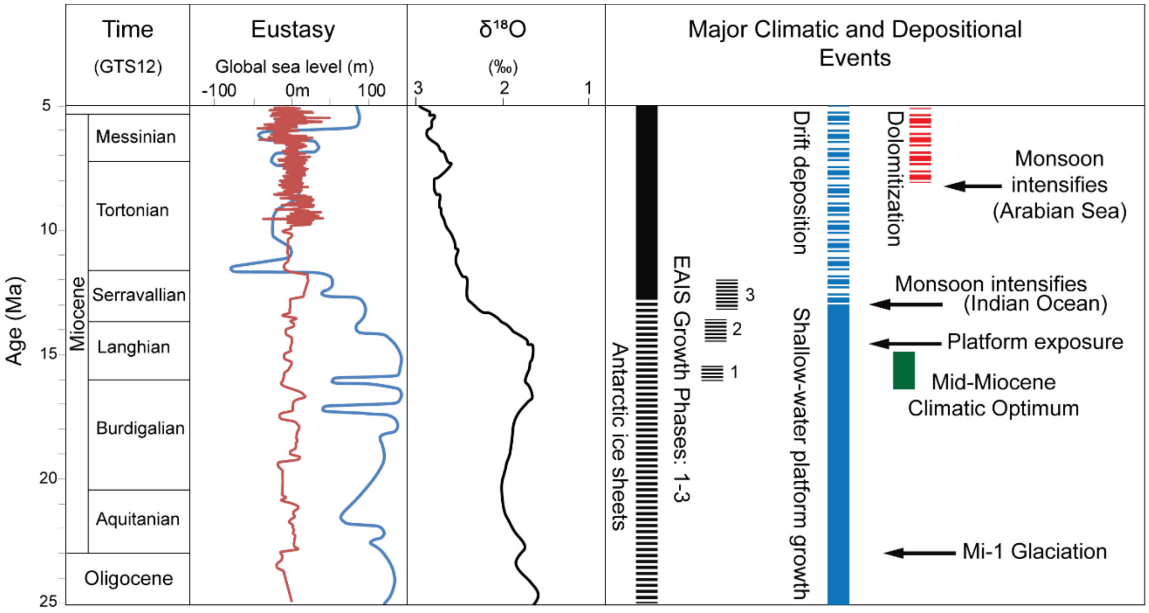

Figure II.20. Major climatic and diagenetic events of the western Kardiva platform. The middle Miocene marks a major change in the climatic evolution of the Cenozoic. Following the climatic optimum in the early Miocene, the middle Miocene represents a period of rapid cooling, producing a permanent change in Cenozoic temperature. High amplitude sea level variations between ~ 16 and 14 Ma mark the middle Miocene. Global sea-level curves (red and blue) are from Miller et al. (2005) and Haq et al. (1987) and emphasize increased frequency and large amplitude sea-level changes respectively. Global $\delta^{18}O$ curve is from Zachos et al. (2001).

Middle Miocene exposures linked to growth of the EAIS were described from other parts of the Indian Ocean. For example, submarine canyon incisions associated with a regional shelf/slope confined unconformity formed in the Durban Basin, South Africa (Hicks and Green, 2017). A similar event was described in the Marion Platform on the northeastern Australian margin where eustatic falls of 33 m and 59 m were associated with the Mi3a and Mi3 glaciations at 13.9 and 15.3 Ma respectively (John et al., 2011).

The seasonal migration of the Intertropical Convergence Zone (ITCZ) has existed since the middle Miocene and controlled a monsoonal rainfall system comparable to today (Kaandorp et al., 2005). Typically, the ITCZ exists in a narrow latitudinal zone over the tropics during glacial minimum periods, covering much of the tropics. In contrast, during times of glacial maxima (**Figure II.21**), the ITCZ becomes narrow as suggested for the Permian (Laya et al., 2013). Antarctic glaciation during the growth of the EAIS would produce northward shifts of the ITCZ (John et al., 2003) and result in increased seasonal precipitation over the Maldives archipelago as was recorded in the northern South China Sea (Holbourn et al., 2010). This rainfall intensification and development of a more humid climate during the time of maximum glaciation would increase the likelihood meteoric fluids affected these exposed atolls during the Miocene before the intensification of South Asian Monsoon at 12.9 My (Gupta et al., 2015; C. Betzler et al., 2016).

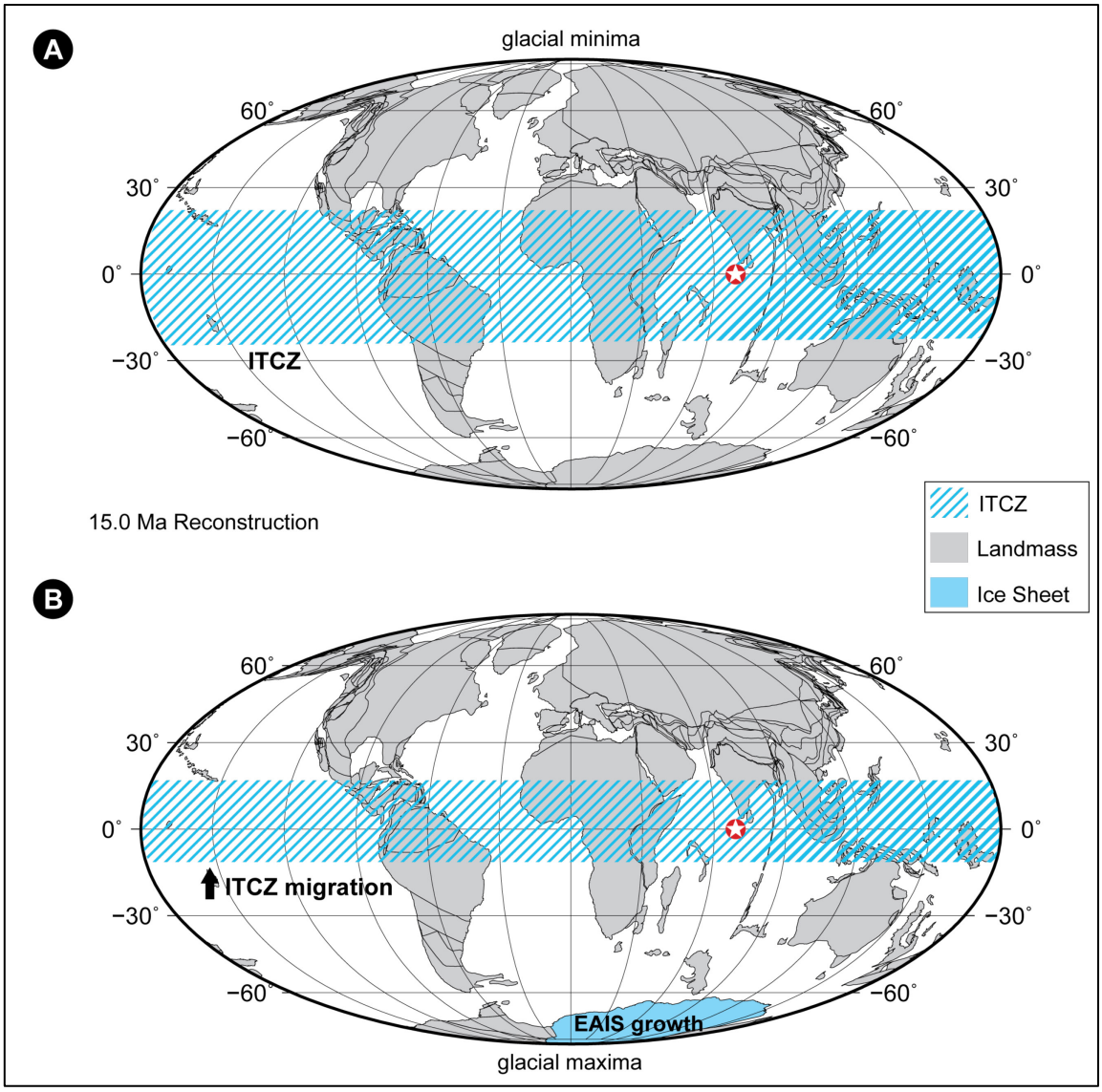

Figure II.21. Schematic palaeogeography of the middle Miocene (Langhian). Red star showing the approximate location of the Kardiva platform. (A) For glacial minima the intertropical convergence zone band was wide, covering more distance away from the equator. (B) For glacial maxima the intertropical convergence zone band was narrow and focused in the tropical area resulting in greater rainfall over the Maldives. Reconstruction is based upon ODSN Plate Tectonic Reconstruction Service (http://www.odsn.de/odsn/services/paleomap/paleomap.html).

Conclusions

This study shows an innovative approach to identifying major high latitude environmental changes in low latitude carbonate sediments. IODP Expedition 359 cores from Kardiva platform record the onset of the EAIS and the narrowing of the ITCZ during the middle Miocene, before the intensification of the SAM. Evidence of this exposure and meteoric alteration is best demonstrated by an exposure surface that is characterized by a negative excursion of stable isotope values for $\delta^{13}C$. This was one of several periods of exposure that affected the platform and overprinted the stable isotopes and elemental concentrations of carbonate cements. The cumulative effect of meteoric alteration during this sea level controlled period of the platform's diagenesis was a major shift in mineralogy from aragonite to low-Mg calcite dominated sediments across the DS to PS transition observed at all of the main study Sites.

This study presents the first identification of platform exposure for Miocene carbonate sediments in the Maldives and provides a record of sea-level in an area where this is not well constrained. Expedition 359 cores from Kardiva platform recorded the onset of the EAIS and the narrowing of the ITCZ during the middle Miocene, before the intensification of the SAM.

Acknowledgements

David Budd, Leslie Melim and Peter Swart provided helpful reviews and comments that greatly improved this manuscript.

References

Abreu, V.S., Anderson, J.B., 1998. Glacial eustasy during the Cenozoic: sequence stratigraphic implications. AAPG Bulletin 82, 1385-1400.

Allan, J., Matthews, R., 1977. Carbon and oxygen isotopes as diagenetic and stratigraphic tools: surface and subsurface data, Barbados, West Indies. Geology 5, 16-20.

Aubert, O., 1994. Origin and stratigraphic evolution of the Maldives (Central Indian Ocean). Rice University.

Aubert, O., Droxler, A., 1996. Seismic stratigraphy and depositional signatures of the Maldive carbonate system (Indian Ocean). Marine and Petroleum Geology 13, 503-536.

Aubert, O., Droxler, A.W., 1992. General Cenozoic evolution of the Maldives carbonate system (equatorial Indian Ocean). Bull Centers Rech Explor Prod Elf-Aquitaine 16.

Bacelle, L., Bosellini, A., 1965. Diagrammi per la stima visiva della composizionze percentuale nelle rocce sedimentarie. Science Geologiche e Paleontologiche Sezione IX, 59-62.

Bailey, R., Jenson, J., Olsen, A., 2008. An atoll freshwater lens algebraic model for groundwater management in the Caroline Islands. Water and Environmental Research Institute of the Western Pacific, University of Guam, UOG Station, Mangilao, Guam 96923, p. 36.

Bathurst, R.G., 1964. The replacement of aragonite by calcite in molluscan shell wall. Approaches to Paleoecology., 357-367.

Bathurst, R.G.C., 1966. Boring algae, micrite envelopes and lithification of molluscan biosparites. Geological Journal 5, 15-32.

Belopolsky, A., Droxler, A., 2003. Imaging Tertiary carbonate system—the Maldives, Indian Ocean: Insights into carbonate sequence interpretation. The Leading Edge 22, 646-652.

Belopolsky, A.V., Droxler, A.W., 2004. Seismic expressions of prograding carbonate bank margins: middle Miocene, Maldives, Indian Ocean, in: Eberli, G.P., Masaferro, J.L., Sarg, J.F. (Eds.), Seismic imaging of carbonate reservoirs and systems.

Betzler, Eberli, G.P., Alvarez-Zarikian, C.A., Alonso-García, M., Bejugam, N.N., Bialik, O.M., Blättler, C.L., Guo, J.A., Haffen, S., Horozal, S., 2016. International ocean discovery program expedition 359 preliminary report: Maldives monsoon and sea level. Integrated Ocean Drilling Program: Preliminary Reports, 1-53.

Betzler, C., Eberli, G., Zarikian, C.A., Scientists, a.t.E., 2017. Maldives Monsoon and Sea Level. Proceedings of the International Ocean Discovery Program, 359. International Ocean Discovery Program, College Station, TX.

Betzler, C., Eberli, G.P., Kroon, D., Wright, J.D., Swart, P.K., Nath, B.N., Alvarez-Zarikian, C.A., Alonso-Garcia, M., Bialik, O.M., Blattler, C.L., Guo, J.A., Haffen, S., Horozal, S., Inoue, M., Jovane, L., Lanci, L., Laya, J.C., Mee, A.L., Ludmann, T., Nakakuni, M., Niino, K., Petruny, L.M., Pratiwi, S.D., Reijmer,

J.J., Reolid, J., Slagle, A.L., Sloss, C.R., Su, X., Yao, Z., Young, J.R., 2016. The abrupt onset of the modern South Asian Monsoon winds. Sci Rep 6, 29838.

Betzler, C., Eberli, G.P., Lüdmann, T., Reolid, J., Kroon, D., Reijmer, J.J.G., Swart, P.K., Wright, J., Young, J.R., Alvarez-Zarikian, C., Alonso-García, M., Bialik, O.M., Blättler, C.L., Guo, J.A., Haffen, S., Horozal, S., Inoue, M., Jovane, L., Lanci, L., Laya, J.C., Hui Mee, A.L., Nakakuni, M., Nath, B.N., Niino, K., Petruny, L.M., Pratiwi, S.D., Slagle, A.L., Sloss, C.R., Su, X., Yao, Z., 2018. Refinement of Miocene sea level and monsoon events from the sedimentary archive of the Maldives (Indian Ocean). Progress in Earth and Planetary Science 5, 5.

Betzler, C., Fürstenau, J., Lüdmann, T., Hübscher, C., Lindhorst, S., Paul, A., Reijmer, J.J.G., Droxler, A.W., 2013. Sea-level and ocean-current control on carbonate-platform growth, Maldives, Indian Ocean. Basin Research 25, 172-196.

Betzler, C., Hubscher, C., Lindhorst, S., Reijmer, J.J.G., Romer, M., Droxler, A.W., Furstenau, J., Ludmann, T., 2009. Monsoon-induced partial carbonate platform drowning (Maldives, Indian Ocean). Geology 37, 867-870.

Budd, D.A., 1988. Aragonite-to-calcite transformation during freshWater diagenesis of carbonates: Insights from poreWater chemistry. GSA Bulletin 100, 1260-1270.

Budd, D.A., Vacher, H.L., 1991. Predicting the thickness of freshWater lenses in carbonate paleo-islands. Journal of Sedimentary Research 61, 43-53.

Choquette, P.W., Pray, L.C., 1970. Geologic nomenclature and classification of porosity in sedimentary carbonates. AAPG bulletin 54, 207-250.

DeConto, R.M., Pollard, D., 2003. Rapid Cenozoic glaciation of Antarctica induced by declining atmospheric CO 2. Nature 421, 245.

Dickson, J.A.D., 2004. Echinoderm Skeletal Preservation: Calcite-Aragonite Seas and the Mg/Ca Ratio of Phanerozoic Oceans. Journal of Sedimentary Research 74, 355-365.

Dix, G.R., Mullins, H.T., 1992. Shallow-burial diagenesis of deepWater carbonates, northern Bahamas: Results from deep-ocean drilling transects. GSA Bulletin 104, 303-315.

Drewry, D.J., 1975. Initiation and growth of the East Antarctic ice sheet. Journal of the Geological Society 131, 255-273.

Duncan, R.A., Storey, M., 1993. The life cycle of Indian Ocean hotspots. Synthesis of Results from Scientific Drilling in the Indian Ocean, 91-103.

Dunham, R.J., 1962. Classification of carbonate rocks according to depositional textures.

Elderfield, H., 1986. Strontium isotope stratigraphy. Palaeogeography, Palaeoclimatology, Palaeoecology 57, 71-90.

Embry, A.F., Klovan, J.E., 1971. A late Devonian reef tract on northeastern Banks Island, NWT. Bulletin of Canadian Petroleum Geology 19, 730-781.

Flower, B., Kennett, J., 1993. Middle Miocene ocean-climate transition: High-resolution oxygen and carbon isotopic records from Deep Sea Drilling Project Site 588A, southwest Pacific. Paleoceanography 8, 811-843.

Flower, B.P., Kennett, J.P., 1994. The middle Miocene climatic transition: East Antarctic ice sheet development, deep ocean circulation and global carbon cycling. Palaeogeography, palaeoclimatology, palaeoecology 108, 537-555.

Flügel, E., 2004. Microfacies of carbonate rocks: analysis, interpretation and application. Springer Science & Business Media.

Fouke, B.W., Beets, C.J., Meyers, W.J., Hanson, G.N., Melillo, A.J., 1996. 87Sr/86Sr Chronostratigraphy and dolomitization history of the Seroe Domi Formation, Curaçao (Netherlands Antilles). Facies 35, 293-320.

Grove, C., Jerram, D.A., 2011. jPOR: An ImageJ macro to quantify total optical porosity from blue-stained thin sections. Computers & Geosciences 37, 1850-1859.

Gupta, A.K., Yuvaraja, A., Prakasam, M., Clemens, S.C., Velu, A., 2015. Evolution of the South Asian monsoon wind system since the late Middle Miocene. Palaeogeography, Palaeoclimatology, Palaeoecology 438, 160-167.

Haq, B.U., Hardenbol, J., Vail, P.R., 1987. Chronology of fluctuating sea levels since the Triassic. Science 235, 1156-1167.

Haywood, A.M., Smellie, J.L., Ashworth, A.C., Cantrill, D.J., Florindo, F., Hambrey, M.J., Hill, D., Hillenbrand, C.-D., Hunter, S.J., Larter, R.D., Lear, C.H., Passchier, S., van de Wal, R., 2008. Chapter 10 Middle Miocene to Pliocene History of Antarctica and the Southern Ocean, in: Florindo, F., Siegert, M. (Eds.), Developments in Earth and Environmental Sciences. Elsevier, pp. 401-463.

Holbourn, A., Kuhnt, W., Regenberg, M., Schulz, M., Mix, A., Andersen, N., 2010. Does Antarctic glaciation force migration of the tropical rain belt? Geology 38, 783-786.

Holbourn, A., Kuhnt, W., Schulz, M., Erlenkeuser, H., 2005. Impacts of orbital forcing and atmospheric carbon dioxide on Miocene ice-sheet expansion. Nature 438, 483-487.

James, N.P., Choquette, P.W., 1984. Diagenesis 9. Limestones - The Meteoric Diagenetic Environment. Geoscience Canada 11.

John, C.d.M., Mutti, M., Adatte, T., 2003. Mixed carbonate-siliciclastic record on the North African margin (Malta)—coupling of weathering processes and mid Miocene climate. GSA Bulletin 115, 217-229.

Kaandorp, R.J.G., Vonhof, H.B., Wesselingh, F.P., Pittman, L.R., Kroon, D., van Hinte, J.E., 2005. Seasonal Amazonian rainfall variation in the Miocene Climate Optimum. Palaeogeography, Palaeoclimatology, Palaeoecology 221, 1-6.

Kendall, C.G.S.C., Schlager, W., 1981. Carbonates and relative changes in sea level. Marine Geology 44, 181-212.

Land, L.S., 1980. The isotopic and trace element geochemistry of dolomite: the state of the art, in: Donald, Z,H., John, D.B., Raymond, E.L. (Eds.), Concepts and Models of Dolomitization. SEPM Special Publication no. 28, pp. 87-110.

Land, L.S., 1983. The application of stable isotopes to studies of the origin of dolomite and to problems of diagenesis of clastic sediments, in: Arthur, M.A., Anderson,

T.F. (Eds.), Stable Isotopes in Sedimentary Geology. SEPM Short course no. 10, pp. 4.1–4.22.

Laya, J.C., Tucker, M.E., Gröcke, D.R., Perez-Huerta, A., 2013. Carbon, oxygen and strontium isotopic composition of low-latitude Permian carbonates (Venezuelan Andes): climate proxies of tropical Pangea. Geological Society, London, Special Publications 376, 367-385.

Lohmann, K.C., 1988. Geochemical Patterns of Meteoric Diagenetic Systems and Their Application to Studies of Paleokarst, in: James, N.P., Choquette, P.W. (Eds.), Paleokarst. Springer New York, New York, NY, pp. 58-80.

Longman, M.W., 1980. Carbonate diagenetic textures from nearsurface diagenetic environments. AAPG bulletin 64, 461-487.

Lüdmann, T., Betzler, C., Eberli, G.P., Reolid, J., Reijmer, J.J.G., Sloss, C.R., Bialik, O.M., Alvarez-Zarikian, C.A., Alonso-García, M., Blättler, C.L., Guo, J.A., Haffen, S., Horozal, S., Inoue, M., Jovane, L., Kroon, D., Lanci, L., Laya, J.C., Mee, A.L.H., Nakakuni, M., Nath, B.N., Niino, K., Petruny, L.M., Pratiwi, S.D., Slagle, A.L., Su, X., Swart, P.K., Wright, J.D., Yao, Z., Young, J.R., 2018. Carbonate delta drift: A new sediment drift type. Marine Geology 401, 98-111.

Lüdmann, T., Kalvelage, C., Betzler, C., Fürstenau, J., Hübscher, C., 2013. The Maldives, a giant isolated carbonate platform dominated by bottom currents. Marine and Petroleum Geology 43, 326-340.

Lumsden, D.N., 1979. Discrepancy between thin-section and X-ray estimates of dolomite in limestone. Journal of Sedimentary Research 49, 429-435.

McKay, J.L., Longstaffe, F.J., Plint, A.G., 1995. Early diagenesis and its relationship to depositional environment and relative sea-level fluctuations (Upper Cretaceous Marshybank Formation, Alberta and British Columbia). Sedimentology 42, 161-190.

Melim, L.A., Swart, P.K., Eberli, G.P., 2004. Mixing-Zone Diagenesis in the Subsurface of Florida and the Bahamas. Journal of Sedimentary Research 74, 904-913.

Miller, K.G., Wright, J.D., Fairbanks, R.G., 1991. Unlocking the Ice House: Oligocene-Miocene oxygen isotopes, eustasy, and margin erosion. Journal of Geophysical Research: Solid Earth 96, 6829-6848.

Milliman, J.D., Müller, G., Förstner, U., 1974. Carbonates and the Ocean, Recent Sedimentary Carbonates: Part 1 Marine Carbonates. Springer Berlin Heidelberg, Berlin, Heidelberg, pp. 3-15.

Naish, T.R., Woolfe, K.J., Barrett, P.J., Wilson, G.S., Atkins, C., Bohaty, S.M., Bücker, C.J., Claps, M., Davey, F.J., Dunbar, G.B., Dunn, A.G., Fielding, C.R., Florindo, F., Hannah, M.J., Harwood, D.M., Henrys, S.A., Krissek, L.A., Lavelle, M., Meer, J.v.d., McIntosh, W.C., Niessen, F., Passchier, S., Powell, R.D., Roberts, A.P., Sagnotti, L., Scherer, R.P., Strong, C.P., Talarico, F., Verosub, K.L., Villa, G., Watkins, D.K., Webb, P.-N., Wonik, T., 2001. Orbitally induced oscillations in the East Antarctic ice sheet at the Oligocene/Miocene boundary. Nature 413, 719-723.

Nelson, C.S., Smith, A.M., 1996. Stable oxygen and carbon isotope compositional fields for skeletal and diagenetic components in New Zealand Cenozoic nontropical

carbonate sediments and limestones: A synthesis and review. New Zealand Journal of Geology and Geophysics 39, 93-107.

Paton, C., Hellstrom, J., Paul, B., Woodhead, J., Hergt, J., 2011. Iolite: Freeware for the visualisation and processing of mass spectrometric data. Journal of Analytical Atomic Spectrometry 26, 2508-2518.

Paton, C., Woodhead, J.D., Hellstrom, J.C., Hergt, J.M., Greig, A., Maas, R., 2010. Improved laser ablation U-Pb zircon geochronology through robust downhole fractionation correction. Geochemistry, Geophysics, Geosystems 11.

Pierson, B.J., Shinn, E.A., 1985. Cement distribution and carbonate mineral stabilization in Pleistocene limestones of Hogsty Reef, Bahamas.

Quinn, T.M., 1991. Meteoric diagenesis of Plio-Pleistocene limestones at Enewetak Atoll. Journal of Sedimentary Research 61, 681-703.

Reinhold, C., 1999. Dog-tooth cements: indicators of different diagenetic environments. Zentralblatt für Geologie und Paläontologie Teil I 1997, 1221-1235.

Roberts, A.P., Wilson, G.S., Harwood, D.M., Verosub, K.L., 2003. Glaciation across the Oligocene–Miocene boundary in southern McMurdo Sound, Antarctica: new chronology from the CIROS-1 drill hole. Palaeogeography, Palaeoclimatology, Palaeoecology 198, 113-130.

Saller, A.H., 1984. Petrologic and geochemical constraints on the origin of subsurface dolomite, Enewetak Atoll: An example of dolomitization by normal seawater. Geology 12, 217-220.

Saller, A.H., 1992. Calcitization of aragonite in Pleistocene limestones of Enewetak Atoll, Bahamas, and Yucatan —An alternative to thin-film neomorphism. Carbonates and Evaporites 7, 56.

Schlager, W., James, N.P., 1978. Low-magnesian calcite limestones forming at the deep-sea floor, Tongue of the Ocean, Bahamas. Sedimentology 25, 675-702.

Sheppard, S.M., Schwarcz, H.P., 1970. Fractionation of carbon and oxygen isotopes and magnesium between coexisting metamorphic calcite and dolomite. Contributions to Mineralogy and Petrology 26, 161-198.

Singh, R.K., Gupta, A.K., Das, M., 2012. Paleoceanographic significance of deep-sea benthic foraminiferal species diversity at southeastern Indian Ocean Hole 752A during the Neogene. Palaeogeography, Palaeoclimatology, Palaeoecology 361-362, 94-103.

Tucker, M.E., 1993. Carbonate diagenesis and sequence stratigraphy, Sedimentology Review 1. Blackwell Scientific Publications Oxford, pp. 51-72.

Vasconcelos, C., McKenzie, J.A., Bernasconi, S., Grujic, D., Tiens, A.J., 1995. Microbial mediation as a possible mechanism for natural dolomite formation at low temperatures. Nature 377, 220.

Veizer, J., 1977. Diagenesis of pre-Quaternary carbonates as indicated by tracer studies. Journal of Sedimentary Research 47, 565-581.

Vulpe, C., 2018. Characterization of the geometry and facies of a carbonate platform drowning sequence (Miocene, Maldives, IODP Expedition 359), Institut für Geologie. Universität Hamburg, Hamburg, p. 64.

Woodruff, F., Savin, S., 1991. Mid-Miocene isotope stratigraphy in the deep sea: High-resolution correlations, paleoclimatic cycles, and sediment preservation. Paleoceanography 6, 755-806.

Woodruff, F., Savin, S.M., 1989. Miocene deepwater oceanography. Paleoceanography 4, 87-140.

Zachos, J., Pagani, M., Sloan, L., Thomas, E., Billups, K., 2001. Trends, Rhythms, and Aberrations in Global Climate 65 Ma to Present. Science 292, 686-693.

CHAPTER III

CURRENT PUMPING: A NEW HYDROLOGICAL MODEL FOR DOLOMITIZATION BY SEAWATER

Abstract

Kohout convection is commonly invoked to account for dolomitization of isolated carbonate platforms. Less attention has been given to the role of deep oceanic bottom-currents in creating advective fluid fluxes and their potential as diagenetic agents. Leached stable isotope analyses, strontium isotope dating, x-ray diffraction and petrographic methods were used to study four IODP sites in the Maldives. Dolomite samples showed a series of characteristics including decreasing crystal size from margin to slope, a flat-topped geometry to the ~50 m subsea dolomite body, cool dolomite formation temperatures (~14°C), and non-stoichiometric dolomite compositions (39-44 mole% $MgCO_3$). Trends in crystal size, cation ordering, geometry of dolomite body, low formation temperatures are incompatible with the expected trend for Kohout Convection as the dolomitizing mechanism. An alternative mechanism whereby oceanic bottom-currents created the "current pumping" of seawater through the upper ~100 meters of the older platform and younger periplatform deposits to create subsurface dolomite. This "current pump" provided the needed transport of reactants to drive dolomite formation and might be an under recognized driver of dolomitization in the geologic record.

Introduction

The formation of dolomite $CaMg(CO_3)_2$ requires an active system of fluid circulation (a "pump") to both supply the necessary Mg^{2+} and remove Ca^{2+}. Normal seawater is an adequate source of Mg^{2+} and account for significant amounts of dolomitization, although it requires high water/rock ratios and a pumping mechanism that circulates large volumes of seawater through the carbonate strata (Zenger, 1972; Land, 1985; Machel and Mountjoy, 1986; Hardie, 1987; Budd, 1997).

Current hydrologic models for dolomitization by normal seawater include freshwater-seawater mixing zones (Machel and Mountjoy, 1980; Vahrenkamp and Swart, 1994), geostrophic currents (Ehrenberg et al., 2006), trans-platform flow driven by difference in sea-surface elevation (Whitaker and Smart, 1993; Whitaker et al., 2004), and convection driven by temperature differences (e.g., Simms, 1984; Wilson et al., 1990; Whitaker et al., 2004). The later process, known as Kohout Convection (Kohout et al., 1977), is applied to isolated carbonate platforms and atolls and has been invoked for numerous Paleogene and Neogene atolls in the Pacific Ocean (e.g. Saller, 1984; Aharon et al., 1987).

This study documents subsea dolomite that formed on the drowned Kardiva carbonate platform in the Maldives and in its periplatform sediments that are not compatible with Kohout convection. Therefore, we propose a new model for dolomitization where the pump that drives the process is created by strong bottom-currents rather than temperature variations or differences in sea-surface elevation.

The rationale for our model is based on the ability of bedforms to create pressure differences within the underlying sediments that generate interstitial flow due to Bernoulli's law. The presence of large sand waves on the seafloor in the study area suggest a potential zone of advective seawater flux to a maximum possible depth of 444 m based on flow rates, porosity and bedform dimensions (Blättler et al, 2019; Cardenas and Wilson 2007). This estimate is sufficiently deep enough to explain dolomite formed up to 350 m below the seafloor. A lack of significant trends in dolomite ordering and the morphology of the dolomite body also support a shallow advective system. Therefore, we propose a new and complementary model of seawater circulation to those currently in use to explain dolomitization of the Kardiva platform and its periplatform deposits.

Geologic Setting

The Kardiva platform carbonates accumulated on a volcanic ridge (**Figure III.1A**) emplaced by hotspot activity beneath the African and Indian plates during the Eocene with carbonate sedimentation beginning with a marine transgression in the Eocene (Duncan and Storey, 1993; Belopolsky and Droxler, 2003). The platform drowned in the middle Miocene as strong bottom currents began to sweep the sea-floor at depths up to 500 m as the of the South Asian Monsoon (SAM) intensified, with the drowning event also preventing the re-establishment of shallow-water sedimentation (Betzler et al., 2009; Lüdmann et al., 2018). The resultant stratigraphy, from oldest to youngest, consists of platform parasequences PS 1 to 11 overlain by periplatform drift parasequences DS 1 to 10 (Betzler et al., 2016a).

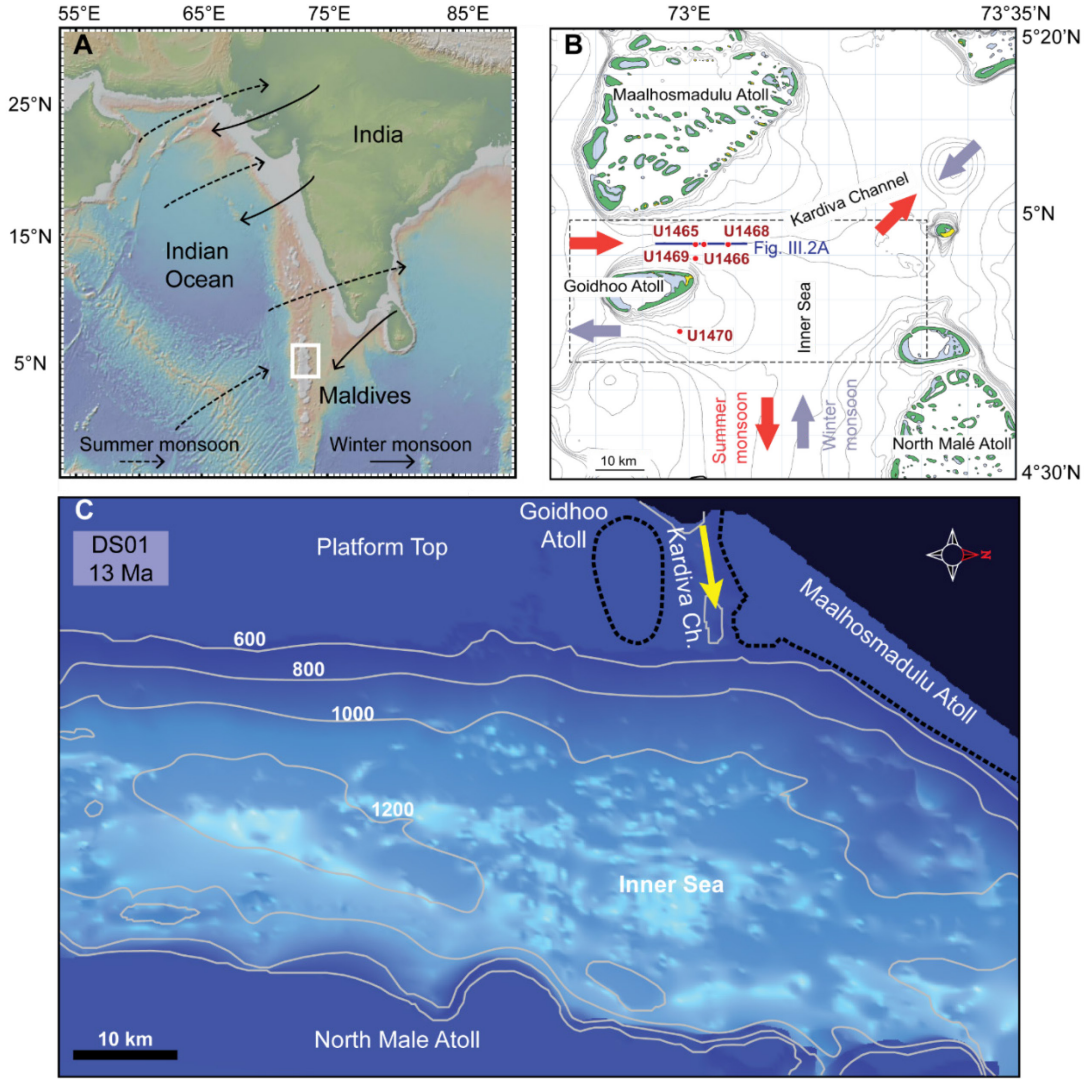

Figure III.1. (A) Location of the Maldives and prevailing wind directions associated with the winter and summer SAM (after Betzler et al., 2016). Satellite imagery from www.geomapapp.org. Inset shows the area of panel B. (B) Map of the study area showing cored IODP Sites and the general pattern of modern bottom-currents below a water depth of 200 m. Red arrows associated with the winter SAM and purple arrows with the summer SAM (Lüdmann et al. 2018). (C) Palaeo-topography in the study atop the DS1 surface (modified after Lüdmann et al., 2018). Isolines show depth in twoWay travel time. Yellow arrow indicates bottom current flow, entering the Inner Sea from the Kardiva Channel. Inset shows the area of panel C.

Methods

Samples for this study were collected from IODP Sites U1465, U1466, U1468, U1469, and U1470 covering 350 m of core (**Figure 1B**). Dolomite crystal diameters (N=476) were measured using thin-section micrographs of 21 samples from the five Sites.

$\delta^{18}O$ and $\delta^{13}C$ analyses were performed on bulk samples (N=19) and data are given relative to Vienna Pee Dee Belemnite (VPDB). Strontium isotope ($^{87}Sr/^{86}Sr$) analyses were performed on bulk samples (N=37) collected approximately every 20 m. Ages were assigned using the lookup table of McArthur et al. (2012) based on the GTS2012 timescale.

The percent dolomite (relative to calcite) was calculated following the approach of Goldsmith and Graf (1958). Dolomite stoichiometry (mole% $MgCO_3$) was calculated using the position of the corrected (104) dolomite reflection (Lumsden, 1979). Cation ordering was calculated following Goldsmith and Graf (1958).

Results

Distribution

Dolomite occurs in both DS (40-140 mbsf) and PS (70-200) sediments with varied replacement textures including fabric destructive and mimetic after red algae. Dolomite abundance ranges from zero to 99.6% (**Figure III.2**) and shows consistent vertical distribution and abundance increase toward the platform margin/interior. The greatest abundance occurs in the platform interior at Site U1469 at 153.22 mbsf (11.52 m below the platform top).

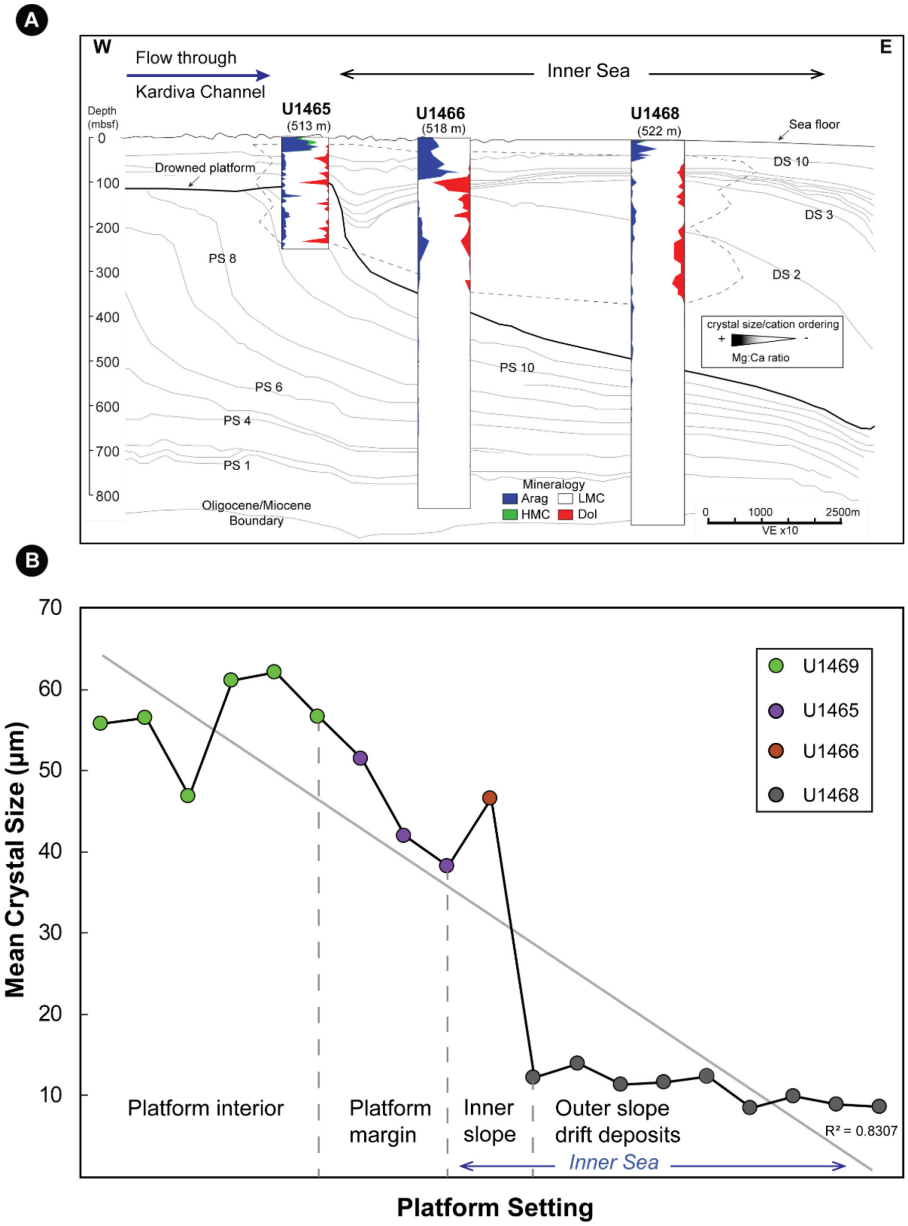

Figure III.2. (A) Generalized 2D cross section of the northern drill Sites showing platform and drift sequence boundaries (PS 1 to 11 and DS 1 to 10) and their relationship to the distribution of dolomite (adapted from Betzler et al., 2018 and Lüdmann et al., 2018). (B) Dolomite crystal sizes versus platform setting shows a decreasing size away from the platform interior and margin.

Average crystal size (**Figure III.2B**) for all dolomite varieties is 48.7 µm (± 20.2 µm) with a range of 27.1 µm (± 12.1 µm) to 81.6 µm (± 35 µm). Crystal size generally decreases with increasing distance from the platform interior/margin with an R^2 value of 0.83. Limited data constrained our ability to investigate variations with depth except at Site U1468 where crystal size ranged from 3.7 µm to 27.7 µm with an average of 10.8 µm. and decreased by ~87% between 61.7 mbsf and 327.5 mbsf.

Stable isotopes

Leached dolomite $\delta^{13}C$ and $\delta^{18}O$ values average 1.9‰ and 2.7‰, respectively. $\delta^{13}C$ ranged from 1.3‰ to 2.7‰ while $\delta^{18}O$ varied between 2.1‰ and 3.5‰. Dolomite in post-drowning drift samples from Site U1466 form one cluster with values for $\delta^{13}C$ averaging 1.5‰ and $\delta^{18}O$ averaging 2.9‰. Dolomite in older platform margin samples from Sites U1465 and U1469 comprise a second cluster where $\delta^{13}C$ averaged 2.3‰ and $\delta^{18}O$ averaged 2.5‰ (**Figure III.3**).

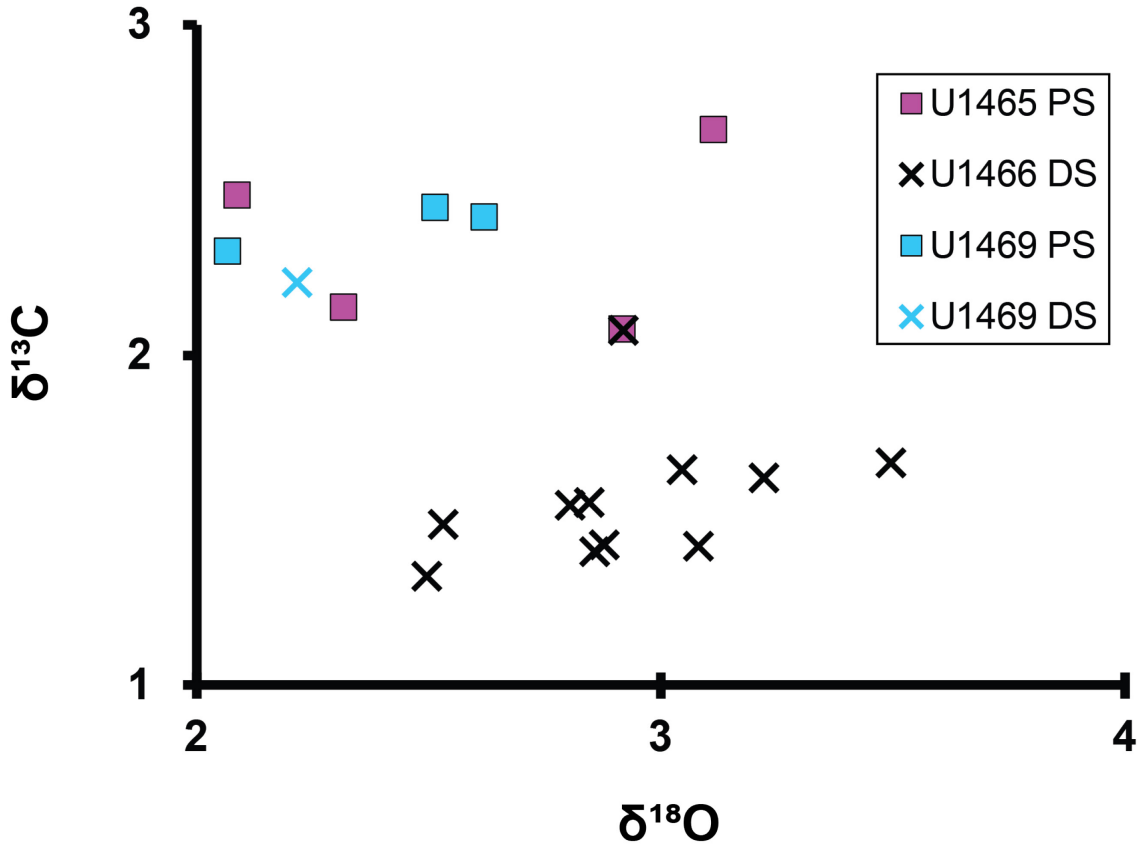

Figure III.3. Dolomite stable isotopes presented by Site and depositional setting.

Paleotemperature calculations using the equation of Land (1985) and $\delta^{18}O_{water}$ of -0.38‰ (SMOW), $\delta^{18}O_{calcite}$ of 0‰ (PDB), and $\delta^{18}O$ between coeval calcite and dolomite of 3‰ yields an estimated range of temperatures between 3.5 to 14.9°C, which is in good agreement with the recorded downhole temperatures of 7.4 to 13.6°C (Betzler et al., 2016).

Stoichiometry

Dolomite crystals in this study are non-stoichiometric with $CaCO_3$ mol% ranging from 56% to 61% (**Figure III.4**). No trends are present with position along the depositional profile. Samples showed a range of 0.05 to 0.45 for cation ordering. Two groups were distinguished: one with relatively poor ordering with ratios <0.10 and a second group showing better ordering with values >0.25 (**Figure III.5**). A trend of increasing cation ordering was observed from Site U1465 at the platform margin (0.3) to U1469 at the platform interior (0.4). This trend in cation ordering also corresponds to a trend of increasing crystal size.

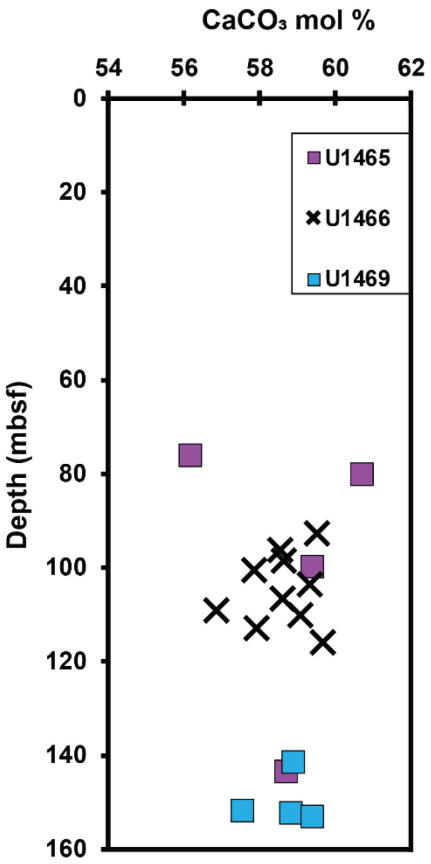

Figure III.4. Dolomite stoichiometry at Sites U1465, U1466, U1469.

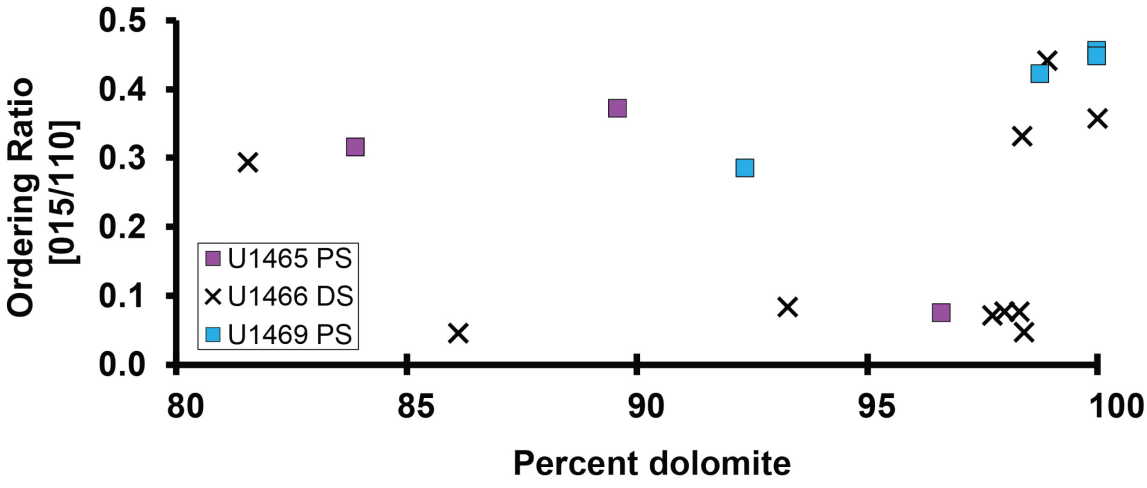

Figure III.5. Dolomite abundance and ordering presented by Site and depositional setting.

Age

Dolomitization in the northern sites crosscuts drift sequences DS1 through DS8 with the greatest amount of dolomite occurring in 5.6 Ma DS6 sediments at U1466 (**Figure III.2A**). This implies that dolomitization of those deposits is younger than ~3.6 Ma based on the biostratigraphic age for DS8 (Betzler et al., 2017). PS samples with the greatest amount of dolomite occur in the platform at U1469 where dolomite reached 99.6%. Bulk strontium isotope derived ages show a coherent increase with depth and likely record values of contemporaneous seawater and thus depositional ages. Some dolomitized samples show higher $^{87}Sr/^{86}Sr$ isotope values than the surrounding sediment, and likely reflect an aggregate timing of dolomitization. The $^{87}Sr/^{86}Sr$ values obtained from leached dolomite samples suggest an age of ~0.9 Ma for the dolomite at 180 mbsf at Site U1470 and ~8.2 Ma at 142 mbsf at Site U1469. Both strontium and biostratigraphic dating methods yield ages younger than the ~12.9 Ma intensification of the SAM system when ocean currents began to exert more control over the local sedimentary system.

Discussion

During the winter SAM, the northern part of the Maldives archipelago is dominated by inflow of water from the Indian Ocean through the Kardiva Channel (**Figure III.1 A, C**) with velocities up to 40 cm/s (Lüdmann et al., 2013). We propose that those currents created advective circulation of normal seawater through the underlying sediment and drove the post-depositional dolomitization of the uppermost

early to middle Miocene platform margin deposits and later periplatform drift sediments. We hypothesize that this advection was initiated or strengthened by bottom-currents associated with the strengthened SAM. Mean seawater is preferred as the dolomitizing fluid as the dolomite $\delta^{18}O$ values (+1.3 to +3.5 ‰ for the four northern cores) suggest seawater formed these dolomite crystals (Hudson, 1977; Machel, 2004; Machel and Burton, 1994; Purser et al., 2009).

A pressure gradient is required to drive an advective flux of seawater into the sediment. Sediment waves formed on the seafloor by bottom currents result in flow being driven into underlying sediment as a result of pressure variations imposed at the upper sedimentWater boundary (Shum, 1992) (**Figure III.6A**). This is dictated primarily by Bernoulli's Law for flow pressure distribution over dunes that are symmetric or have a small height-to-length ratio. Cardenas and Wilson (2007) provide a numerical analysis of such a setting in which turbulence in the overlying water column combined with the topography of sedimentary bedforms creates the needed pressure gradient. In this scenario, water downwells near the pressure maximum along stoss faces (**Figure III.6B**), with some water downwelling deeply and not returning to the sediment water interface and discharge occurring at the pressure minimum on crests. Over lateral distances of many kilometers, this flow field is thus a suite of circulation cells and dolomite bodies below each bedform (**Figure III.6C**).

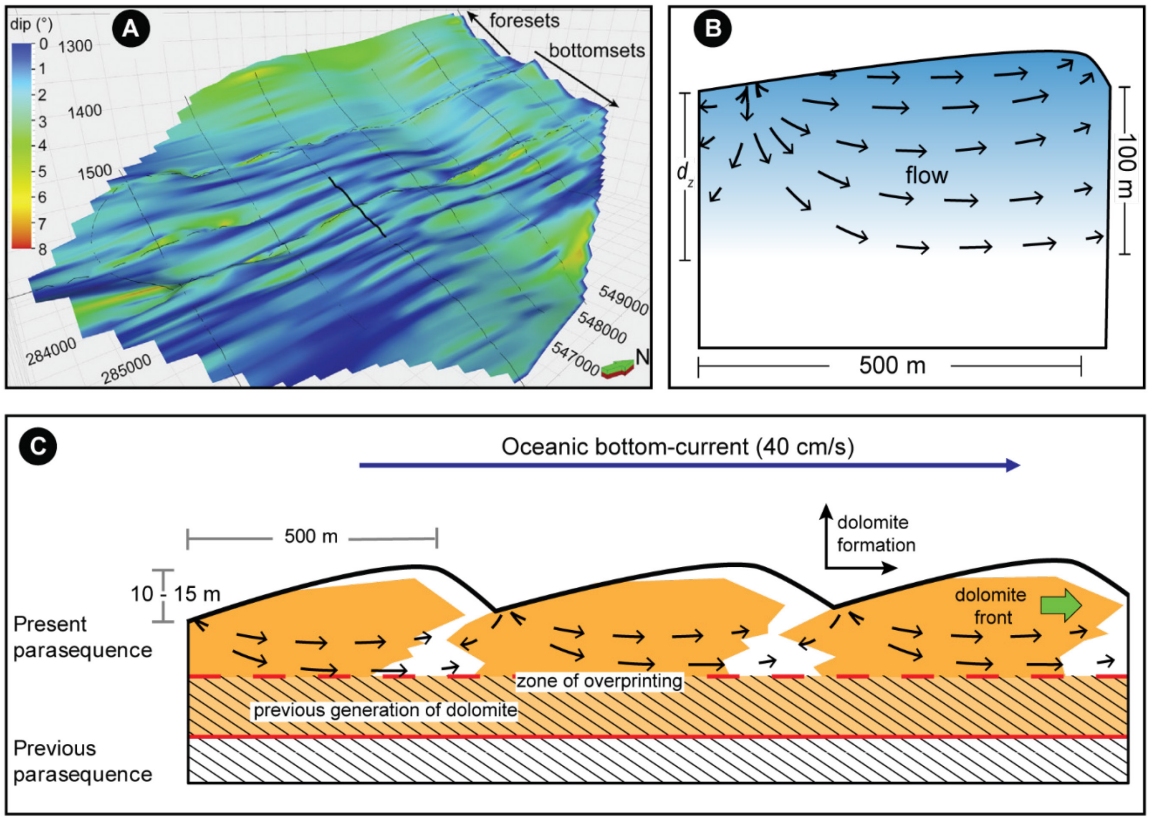

Figure III.6. (A) 3D view of cyclic steps (large sediment waves) at the base of the oldest drift parasequences (DS1). The dip angle of the surface is expressed via the color scale and shows low upslope (stoss) and high downslope (lee) inclinations of the margin-parallel sediment waves (after Lüdmann et al., 2018). (B) Modeling results (adapted from Cardenas and Wilson, 2007) showing streamlines of advective flow that results from pressure variations imposed at the upper sediment-water boundary. Streamlines show flow directions but not velocities. Color gradient shows intensity of advection from strong (blue) to weak (white) (C) Model for dolomite formation invoking shallow advective flow. Flow lines are time transgressive and overprint the younger parasequence.

The depth of the zone of infiltration, dz, can be estimated using the equation of Cardenas and Wilson (2007):

$$dz^* = (dz/L)\,(H/L)cd = 0.379 \qquad (1)$$

Equation 1 provides a maximum estimate of advective flux into the sediment of 407 to 444 m for dunes with heights (H) of 10 to 15 m and lengths (L) of 500 m as reported by Lüdmann et al. (2018) (**Figure III.6A**). Equation 1 assumes an isotropic and homogeneous sediment, but since that is surely not the case, these are maximum estimates. If anisotropy is considered, equation 1 can be modified as:

$$dz^*=(dz/L)\ (H/L)cd\ = 0.379(kz/kh)0.5(1+cd) \qquad (2)$$

This scales the depth of the zone of infiltration by a factor ~0.246 of the isotropic case (Bear, 1972, 1979; Fetter, 2001), meaning advective flux into the sediment of 100 to 109 m. This estimate for the anisotropic case is still more than adequate to pump seawater far below the sedimentWater interface and dolomitize underlying carbonates. Blättler et al. (2019). The existence of a shallow advective system is indicated based on pore fluid data that sediments deep within the interior of the Kardiva platform are exposed to Pleistocene waters.

Our model suggests that easterly bottom water flow through the Kardiva Channel is responsible for dolomitization in the northern cores. These currents presumably drive seawater through the upper 50 – 150 m of porous sediments and provide the Mg needed for dolomitization. Dolomite abundance and crystal size are greater in areas proximal to the oceanward aperture of the channel and decreases towards the Inner Sea (**Figure III.2B**). This is interpreted to reflect attenuation of the bottom current as it enters the Inner Sea and dissipates over a larger cross-sectional area (i.e., is no longer restricted to the Kardiva channel). Slower bottom water flow means reduced bedform sizes, thus reduced pressure gradients and advective fluxes. As a result, there would be less

dolomite, and smaller dolomite crystal sizes in the outer shelf drift. The dissipation of flow, however, would not affect dolomite stoichiometry because dolomitization along each individual flow path (Figure 3C) is still relatively short (~ 500 m). Therefore there would be little evolution in pore water Mg:Ca ratio along the path. At the upper and lower surfaces situated in the drift deposits, the dolomite body is near horizontal suggesting that bottom-currents flushed fluid into these upper regions to a uniform depth (**Figure III.6C**).

The variation in dolomite formation ages and the different populations of dolomite $\delta^{18}O$ values also suggest that dolomitization may have occurred as multiple events. It is possible that as each DS parasequence accumulated, the zone of advective flux would have risen stratigraphically through time (**Figure III.6C**), thus the age of dolomite formation should be time transgressive (younger on top), and older ones could be multi-generational. For example, dolomite in DS3 formed while DS4 was depoSited, then perhaps overprinted with dolomite during DS5 and DS6 deposition.

Similar aged dolomitization was reported from Marion Plateau and Enewetak and Niue atolls in the Pacific Ocean where dolomitization occurred during the early Miocene as indicated by $^{87}Sr/^{86}Sr$ ratios (Aharon et al., 1987; Budd, 1997; Ehrenberg et al 2006; Saller, 1984). The model proposed for these atolls involved seawater advection through shallow limestone strata, but by Kohout convection (Kohout, 1965, 1967; Kohout et al., 1977; Simms, 1984). In both atolls, the resultant dolomitization was focused at the platform margin and occurred at depths at about a kilometer or more, which is in keeping with reactive transport models that suggests most dolomitization in

atoll-like settings is focused near the margin and at depths near 1500 m (Wilson et al., 2001). In contrast, in the Maldives, dolomitization occurred at relatively shallow depths (not exceeding 350 m) and also at the platform interior (Site U1469) where abundant coralline algae might have influence dolomitization (Bullen and Sibley, 1984; Laya et al., 2018).

The western, ocean facing margin of the Kardiva platform has a steep angle and Kohout convection might be present, but it seems unlikely for the investigated Sites on the northern side of the platform. Since cold water should be drawn into the platform's steep western margin, fluids would have to travel ~25 km before arriving at the most distal northern Site, U1468. Numerical models of Kohout convection (e.g., Caspard et al., 2004; Whitaker and Xiao, 2010) do not support the flow paths and geometry of the convection cell that would be required to reach the northern Sites. Instead those models predict a dominance of upward flow in the platform with higher flow velocity on the slope, and more complete dolomitization for the given time period (13 Ma) respectively. In the northern cores, no evidence of fluid evolution is reflected in the stoichiometry of the dolomite, which should occur over such a long distance, suggesting that flow paths were relatively short (Kaczmarek and Sibley, 2011). This lack of stoichiometry coupled with the flat, geometry of the dolomite body, cool temperatures, and very shallow depths support the current pumping model, not Kohout convection.

Conclusions

Dolomitization of the Kardiva platform is inconsistent with Kahout convection, which is the most commonly invoked hydrologic model for atoll and isolated platforms. The stoichiometry, crystal size trends and spatial distribution of the dolomite body suggest a shallow system of advection acting as a hydrologic pump. This study offers two key findings. Firstly, that bottom-currents can provide an effective mechanism to circulate seawater through sediments and promote dolomite formation in any setting. Secondly, that dolomitization in such a shallow advective system can produce significant amounts of dolomite (~50%) in less than 5.6 Ma.

References

Aharon, P., Socki, R. A., and Chan, L., 1987, Dolomitization of Atolls by Sea Water Convection Flow: Test of a Hypothesis at Niue, South Pacific: The Journal of Geology, v. 95, no. 2, p. 187-203.

Belopolsky, A., and Droxler, A., 2003, Imaging Tertiary carbonate system—the Maldives, Indian Ocean: Insights into carbonate sequence interpretation: The Leading Edge, v. 22, no. 7, p. 646-652.

Betzler, Eberli, G. P., Giosan, L., and Zarikian, C. A., 2016b, International Ocean Discovery Program Expedition 359 Scientific Prospectus Sea Level, Currents, and Monsoon Evolution in the Indian Ocean: World Wide Web, v. 2332, p. 1385.

Betzler, C., Eberli, G. P., Kroon, D., Wright, J. D., Swart, P. K., Nath, B. N., Alvarez-Zarikian, C. A., Alonso-Garcia, M., Bialik, O. M., Blattler, C. L., Guo, J. A., Haffen, S., Horozal, S., Inoue, M., Jovane, L., Lanci, L., Laya, J. C., Mee, A. L., Ludmann, T., Nakakuni, M., Niino, K., Petruny, L. M., Pratiwi, S. D., Reijmer, J. J., Reolid, J., Slagle, A. L., Sloss, C. R., Su, X., Yao, Z., and Young, J. R., 2016c, The abrupt onset of the modern South Asian Monsoon winds: Sci Rep, v. 6, p. 29838.

Betzler, C., Hübscher, C., Lindhorst, S., Reijmer, J. J. G., Römer, M., Droxler, A. W., Fürstenau, J., and Lüdmann, T., 2009, Monsoonal-induced partial carbonate platform drowning (Maldives, Indian Ocean): Geology, v. 37.

Blättler, C. L., Higgins, J. A., and Swart, P. K., 2019, Advected glacial seawater preserved in the subsurface of the Maldives carbonate edifice: Geochimica et Cosmochimica Acta, v. 257, p. 80-95.

Budd, D. A., 1997, Cenozoic dolomite of carbonate islands: their attributes and origin: Earth-Science Reviews, v. 42, no. 1, p. 1-47.

Bullen, S. B., and Sibley, D. F., 1984, Dolomite selectivity and mimic replacement: Geology, v. 12, no. 11, p. 655-658.

Cardenas, M. B., and Wilson, J. L., 2007, Exchange across a sediment–water interface with ambient groundwater discharge: Journal of Hydrology, v. 346, no. 3, p. 69-80.

Caspard, E., Rudkiewicz, J.-L., Eberli, G. P., Brosse, E., and Renard, M., 2004, Massive dolomitization of a Messinian reef in the Great Bahama Bank: a numerical modelling evaluation of Kohout geothermal convection: Geofluids, v. 4, no. 1, p. 40-60.

Duncan, R. A., and Storey, M., 1993, The life cycle of Indian Ocean hotspots: Synthesis of Results from Scientific Drilling in the Indian Ocean, p. 91-103.

Ehrenberg, S., McArthur, J., and Thirlwall, M., 2006, Growth, demise, and dolomitization of Miocene carbonate platforms on the Marion Plateau, offshore NE Australia: Journal of Sedimentary Research, v. 76, no. 1, p. 91-116.

Hardie, L. A., 1987, Dolomitization; a critical view of some current views: Journal of Sedimentary Research, v. 57, no. 1, p. 166-183.

Hudson, J., 1977, Stable isotopes and limestone lithification: Journal of the Geological Society, v. 133, no. 6, p. 637-660.

Kaczmarek, S. E., and Sibley, D. F., 2011, On the evolution of dolomite stoichiometry and cation order during high-temperature synthesis experiments: An alternative model for the geochemical evolution of natural dolomite: Sedimentary Geology, v. 240, no. 1, p. 30-40.

Kohout, F., 1965, A hypothesis concerning cyclic flow of salt water related to geothermal heating in the Floridian Aquifer: Transactions of the New York Academy of Sciences, v. 28, p. 249-271.

Kohout, F., 1967, GroundWater Flow and the Geothermal Regime of the Floridian Plateau, Transactions of the Gulf Coast Association of Geological Societies, v. 17, p. 339-354.

Kohout, F., Henry, H., and Banks, J., 1977, Hydrogeology related to geothermal conditions of the Floridan Plateau: Florida Bureau of Geology Special Publication, no. 21.

Land, L. S., 1985, The origin of massive dolomite: Journal of Geological Education, v. 33, no. 2, p. 112-125.

Laya, J. C., Sulaica, J., Teoh, C. P., Whitaker, F., Gabellone, T., Tucker, M., Tesch, P., Miller, B., Prince, K., and Izaguirre, I., 2018, Controls on Neogene carbonate facies and stratigraphic architecture of an isolated carbonate platform – the Caribbean island of Bonaire: Marine and Petroleum Geology.

Lüdmann, T., Betzler, C., Eberli, G. P., Reolid, J., Reijmer, J. J. G., Sloss, C. R., Bialik, O. M., Alvarez-Zarikian, C. A., Alonso-García, M., Blättler, C. L., Guo, J. A., Haffen, S., Horozal, S., Inoue, M., Jovane, L., Kroon, D., Lanci, L., Laya, J. C., Mee, A. L. H., Nakakuni, M., Nath, B. N., Niino, K., Petruny, L. M., Pratiwi, S. D., Slagle, A. L., Su, X., Swart, P. K., Wright, J. D., Yao, Z., and Young, J. R., 2018, Carbonate delta drift: A new sediment drift type: Marine Geology, v. 401, p. 98-111.

Lüdmann, T., Kalvelage, C., Betzler, C., Fürstenau, J., and Hübscher, C., 2013, The Maldives, a giant isolated carbonate platform dominated by bottom currents: Marine and Petroleum Geology, v. 43, p. 326-340.

Machel, H.-G., and Mountjoy, E. W., 1986, Chemistry and Environments of Dolomitization —A Reappraisal: Earth-Science Reviews, v. 23, no. 3, p. 175-222.

Machel, H., and Mountjoy, E., 1990, Coastal mixing zone dolomite, forward modeling, and massive dolomitization of platform-margin carbonates: Discussion: Journal of Sedimentary Research, v. 60, no. 6.

Machel, H. G., 2004, Concepts and models of dolomitization: a critical reappraisal: Geological Society, London, Special Publications, v. 235, no. 1, p. 7-63.

Machel, H. G., and Burton, E. A., 1994, Golden Grove Dolomite, Barbados; origin from modified seawater: Journal of Sedimentary Research, v. 64, no. 4a, p. 741-751.

McArthur, J. M., Howarth, R. J., and Shields, G. A., 2012, Chapter 7 - Strontium Isotope Stratigraphy, in Gradstein, F. M., Ogg, J. G., Schmitz, M. D., and Ogg, G. M., eds., The Geologic Time Scale: Boston, Elsevier, p. 127-144.

Purser, B. H., Tucker, M. E., and Zenger, D. H., 2009, Dolomite: A volume in honour of Dolomieu, John Wiley & Sons.

Saller, A. H., 1984, Petrologic and geochemical constraints on the origin of subsurface dolomite, Enewetak Atoll: An example of dolomitization by normal seawater: Geology, v. 12, no. 4, p. 217-220.

Shum, K. T., 1992, Wave-induced advective transport below a rippled water-sediment interface: Journal of Geophysical Research: Oceans, v. 97, no. C1, p. 789-808.

Simms, M., 1984, Dolomitization by groundwater-flow system in carbonate platforms.

Vahrenkamp, V., and Swart, P. K., 1994, Late Cenozoic dolomite of the Bahamas: metastable analogues for the genesis of ancient platform dolomite: Dolomite: A volume in honour of Dolomieu, v. 21, p. 133-153.

Whitaker, F. F., Smart, P. L., Horbury, A. D., and Robinson, A. G., 1993, Circulation Of Saline Ground Water In Carbonate Platforms—A Review and Case Study From the Bahamas, Diagenesis and Basin Development, Volume 36, American Association of Petroleum Geologists, p. 0.

Whitaker, F. F., Smart, P. L., and Jones, G. D., 2004, Dolomitization: from conceptual to numerical models: Geological Society, London, Special Publications, v. 235, no. 1, p. 99-139.

Whitaker, F. F., and Xiao, Y., 2010, Reactive transport modeling of early burial dolomitization of carbonate platforms by geothermal convection: AAPG bulletin, v. 94, no. 6, p. 889-917.

Wilson, A. M., Sanford, W., Whitaker, F., and Smart, P., 2001, Spatial patterns of diagenesis during geothermal circulation in carbonate platforms: American Journal of Science, v. 301, no. 8, p. 727-752.

Wilson, E. N., Hardie, L. A., and Phillips, O. M., 1990, Dolomitization front geometry, fluid flow patterns, and the origin of massive dolomite: the Triassic Latemar buildup, northern Italy: American Journal of Science, v. 290, no. 7, p. 741-796.

Zenger, D. H., 1972, Dolomitization and Uniformitarianism: Journal of Geological Education, v. 20, no. 3, p. 107-124.

CHAPTER IV

LINKING DIAGENESIS TO BOTTOM CURRENT STRENGTH: CEMENT OVERGROWTHS ON BENTHIC FORAMINIFERA AT SITE U1468, KARDIVA PLATFORM, MALDIVES

Abstract

Foraminifera are some of the most widely used microfossils for reconstructing paleoceanographic changes during the last ~300 Ma of earth's history. However, in some cases, extensive alteration can diminish a foraminifer's original features. Diagenesis therefore often masks the paleoenvironmental insights that foraminifera could provide. However, in this study we utilized these mostly early diagenetic alterations to interpret paleooceanographic changes as well as to document near-seafloor processes.

Using foraminiferal samples from Site U1468, we utilized grain size and crystal length measurements by employing a CAMSIZER and scanning electron microscope respectively. Our observations show that calcite overgrowth lengths reflect changes in the rate of the supply of reactants (i.e. carbonate ions) and in this hydrodynamic setting, are controlled by the rate of interstitial flow. In the Maldives, interstitial water chemistry shows values similar to that of mean seawater between 50 and 100 m below the seafloor. This suggests that seawater is actively circulating through the interstitial pores over this interval and driving the kinetics of surface nucleation and the amount of reactants.

These findings suggest the presence of a 20 to 25 m deep advective zone in the middle to late Miocene sediments at Site U1468. This zone was delineated from the crystal length inflection points on the 125 or 250 μm grain size classes where the inflection from decreasing to increasing crystal sizes occur at or below the interglacial surfaces. The best way to explain this is by advection into the sediments during glacial periods down into lower horizons that were originally deposited during interglacial periods. We suggest that changes in glacioeustasy from the middle to late Miocene influenced oceanic circulation and bottom-currents and thereby the advection of seawater below the sediment-water interface. Changes in the strength of the advective regime therefore are the main control on the size of the calcite overgrowths suggesting that overgrowth crystal size is a proxy for advective strength.

Introduction

Benthic foraminifera are important biogenic components of Cenozoic and Neogene carbonate rocks and are some of the most widely used microfossils for reconstructing paleoceanographic changes (Sarkar et al., 2009). Foraminifera are testate unilocular species (Pawlowski et al., 2003), and can have varied compositions including calcite, aragonite, silica, organic matter, or foreign particles (Gupta, 2002) with each species having distinctive chamber numbers, shapes and ornamentation (Haynes, 1981). Calcitic foraminifera are sub-divided into species that precipitate low magnesium calcite (LMC), high magnesium calcite (HMC), or aragonite (Gussone, 2016). Benthic foraminifera are further sub-divided into small benthic foraminifera (SBF) with simple internal structures and large benthic foraminifera (LBF) with complex internal structures. Larger foraminifera are K-strategists which have evolved to occupy niches in oligotrophic, shallow, tropical environments (Hottinger, 1990).

Many species of foraminifera serve as stratigraphic markers between eras of drastic changes in the environment. Species are confined to distinctive time periods, temperature, salinity, and geographical ranges oftentimes occupying particular ecological niches (Haynes, 1981).

At Site U1468, the main large benthic foraminifera (LBF) include S. *globulus*, *Lepidocyclina* sp., *Amphistegina* sp., *Operculina* sp., *Cycloclypeus annulatus*, *Miogypsinoides* sp., *Sphaerogypsina Globulus*, and *Heterostegina* sp. (Betzler et a1., 2017). Although larger benthic foraminifera like those listed also occur in relatively deep

settings, their carbonate production depends on endosymbiotic relationships with unicellular algae and therefore on the penetration of light into the water column (Vaziri-Moghaddam et al., 2006).

Foraminifera tests experience diagenetic processes that include but are not limited to dissolution, overgrowth, and recrystallization (Pearson, 2008). The process begins with etching, transforming the tests from clear or glassy to dull and cloudy and ends with extensive damage to the test. Foraminifera dissolution is an important diagenetic process, manifested through etching and breakage of test walls and is more pronounced in topographic highs, possibly aided by abrasion (Flügel, 2004). Fibrous calcite overgrowths on foraminiferal tests were first described by Friedman (1975) and Kendall (1976). These cements were characterized as bladed calcite crystals that showed radial extinction and project into intergranular and intragranular pore spaces. The foraminiferal species also appears to exercise some inüuence on the diagenetic outcomes. For example thinner-walled species were dissolved first suggesting an assemblage control on dissolution (Collen and Burgess, 1979) whereas others suggest that overgrowths were the result of a progressive sequence controlled in part by the composition, size, habit and/or orientation of the tests rather than the surrounding matrix (Banner and Wood, 1964).

While foraminifera are important tools in the study of paleoceanographic evolution, alteration typically diminishes their utility in this regard with several studies outlining criteria by which foraminifera diagenesis can be recognized to exclude such samples from consideration (Schrag et al., 1992; Huber et al., 1995; Norris and Wilson,

1998). Here, we employ a novel approach by using extensively cemented foraminifera to deduce environmental and oceanographic changes in Miocene sediments.

This study investigates the relationship between current strength and the development of calcite crystal overgrowths in a diagenetic system where advective fluid flow dominates. We suggest that changes in monsoon intensity from the middle Miocene to early Pliocene dictated oceanic circulation and bottom-currents and thereby the advection of seawater below the sediment-water interface. Changes in the strength of the advective regime therefore are the main control on the size of the calcite overgrowths suggesting that crystal size is a proxy for advective flow strength.

Geologic Setting

Site U1468, located at 4°55.98′N and 73°4.28′E, lies in 521.5 m of water in the eastern Kardiva Channel (**Figure IV.1**) and was selected to reconstruct the platform evolution from the Oligocene/Miocene boundary, date its sequence boundaries, and constrain the timing of the platform drowning (Betzler et al., 2016a) (**Figure IV.1C**).

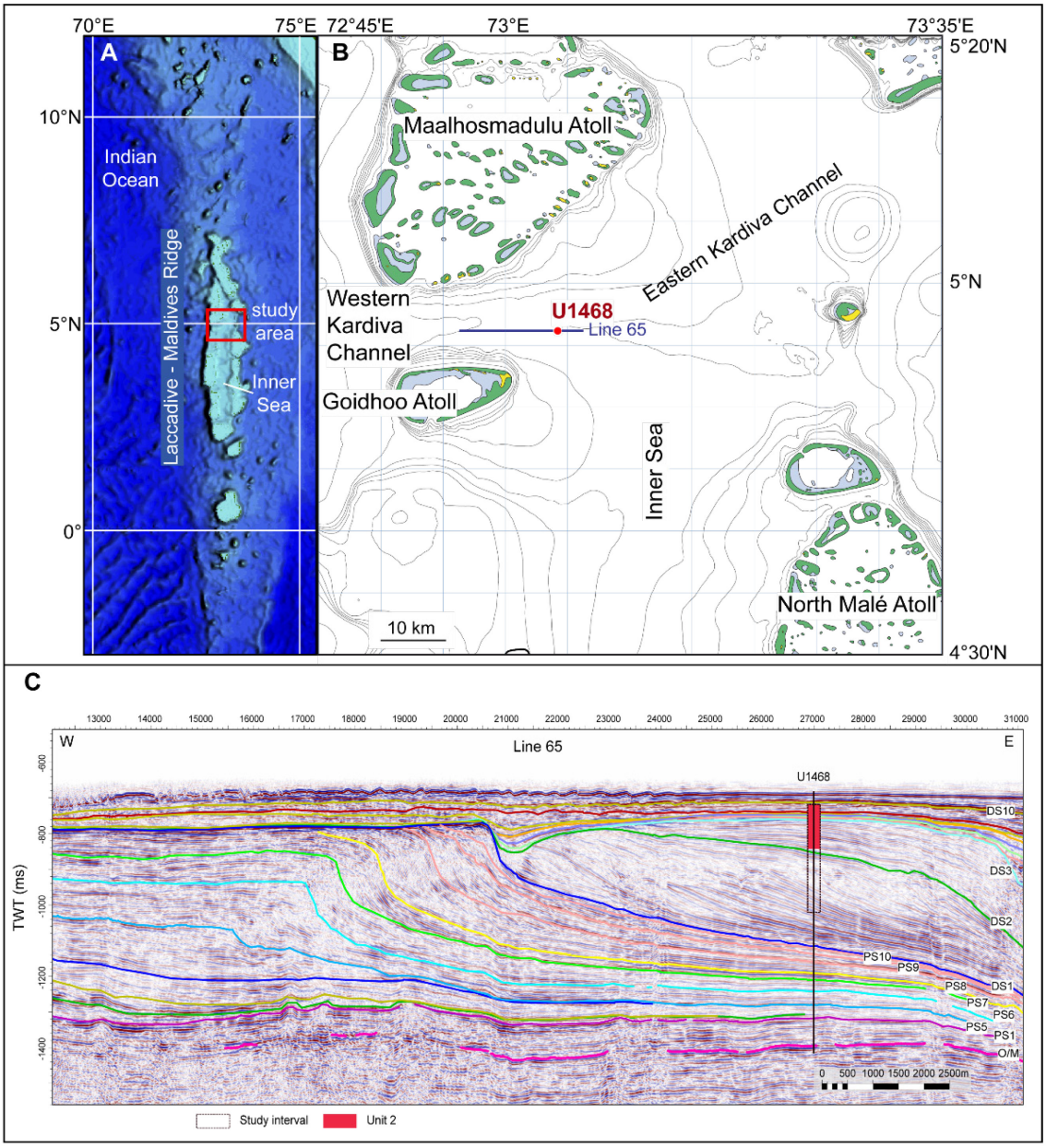

Figure IV.1. (A) Location of the Maldives archipelago in the Indian Ocean. (B) IODP Expedition 359 Site U1468 in the Inner Sea and the location of the western Kardiva Channel (modified from Betzler et al., 2017). (C) Seismic line 65 with the of Site U1468, sequence boundaries and the extent of the study interval.

Site U1468 is key to addressing issues of global ocean circulation as the drift deposits here were influenced by changes to the bottom current regime (**Chapter III**). Samples for this study were collected between 48.9 to 428.56 mbsf and correspond to lithostratigraphic units II-V described by Betzler et al. (2016a). These units consist of bioclastic wackestone – rudstone with abundant planktonic and benthic foraminifera that contain extensive calcite cement overgrowths.

Shallow drift deposits

Site U1468 contains the record of a new category of channel related drift deposit termed a delta drift (Lüdmann et al., 2018). These drifts are composed of several stacked lobes deposited at the mouth of conduits where the velocity of the flow dissipated (Lüdmann et al., 2018). In the Maldives archipelago, these drift deposits are associated with the transition from a sea level-controlled system to one where bottom currents dominate as the South Asian Monsoon (SAM) intensified (Betzler et al., 2018). Eastward flowing bottom currents directed through channels and passages, created by the drowning of the original carbonate platform, entrained carbonate allochems and re-deposited them at the mouth of the Kardiva Channel as sigmoidal clinoforms that thin both proximally and distally (Reolid et al., 2019).

Planktonic foraminifera dominate the lower units of the drift deposits until benthic foraminifera in Unit II supplant them. This is expressed by a change in facies from chert-nodule packstone and sponge spicule–bryozoan packstone to LBF-rich facies. Changes to the strength of the bottom currents are reflected in Unit II by the fluctuations

of micrite in the LBF-rich facies as intense currents winnowed the finer material (Reolid et al., 2019). This facies transition is the result of rapid sedimentation and filling of accommodation space, which created a shallow marine environment suitable for *in-situ* carbonate production by LBF (Betzler et al., 2017).

Methods

103 samples from Hole U1468A (4°55.9832′N 073°4.2780′E) were analyzed for this study. Each sample was mechanically sub-divided using a splitter to separate a working portion with the remaining portion preserved as an archival sample. Sieved samples were placed under a stereoscope to pick foraminifera using a fine paintbrush. Foraminifera were selected in various states of preservation: whole, partially dissolved and fragmented. 20-30 forams were mounted from each sample on an individual pin mount that was prepared with double-sided carbon adhesive tape. Images of the cements were captured using a Phenom XL Scanning Electron Microscope (SEM). Crystal lengths were measured along the c-axis from the nucleation point on the wall of the test to the tip of the crystal using the Olympus Stream Essentials and ImageJ programs. 20-40 individual crystals were measured per individual foraminifera yielding 400 to 800 individual measurements per sample stub. Measurements for the average maximum, minimum and mean length of the crystals were reported for each stub/sample for all samples. Samples from 48.9 to 192 mbsf (lithostratigraphic unit II) were sieved and sorted into four size fractions: 500 μm, 355 μm, 250 μm, and 125 μm. For these samples,

five to ten foraminifera from each size fraction were mounted and SEM-imaged with crystal sizes reported for each of the four size fractions.

Grain size distributions were obtained using a Retsch Camsizer P4, a compact laboratory instrument that uses dynamic image analysis determine particle size and shape as a sample was passed between a light source and two cameras.

Results

Grain Size

Grain size of the foraminifera varied downhole between 0.33 mm and 2.12 mm (**Figure IV.2**) (medium sand to granule size after the system first proposed by Udden (1898) then modified and extended by Wentworth (1922)) with a mean of 0.82 mm (coarse sand. Most samples were classified as skeletalgrainstone according to the Dunham (1962) classification scheme as modified by Embry and Klovan (1971) but range from mudstone to rudstone.

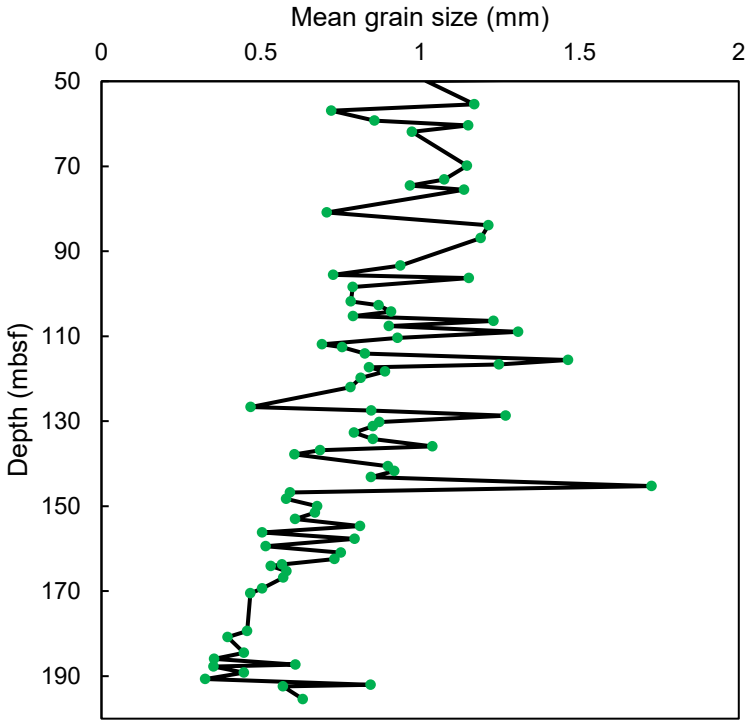

Figure IV.2. Mean grain size, Unit II.

The fine fraction (<63 μm grain size) is plotted with depth in **Figure IV.3** and ranges from zero to 2.3%, with an average of 0.44% and a median of 0.15%.

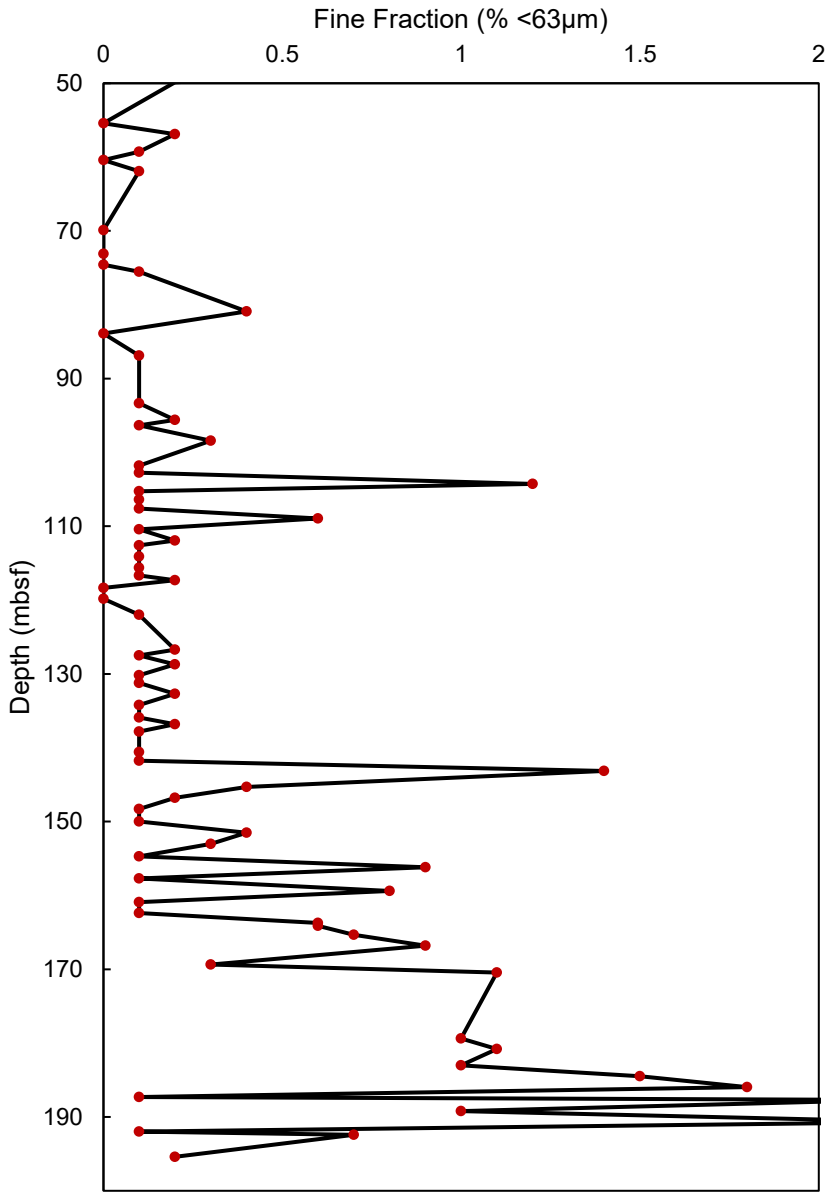

Figure IV.3. Fine fraction abundance (% <63µm grains), Unit II.

Overgrowths

Both LBF and planktonic foraminifera were extensively altered, showing a frosted appearance when observed under stereomicroscope. Various states of preservation were observed as fracturing and/or abrasion of the foraminifera test (**Figure IV.4A**) and the crystals themselves (**Figure IV.4B**). Most calcite crystals were observed on the exterior of the tests but where grains were fractured and shell's interior exposed, lesser cementation was noted in the internal chambers (**Figure IV.5C**, **D**).

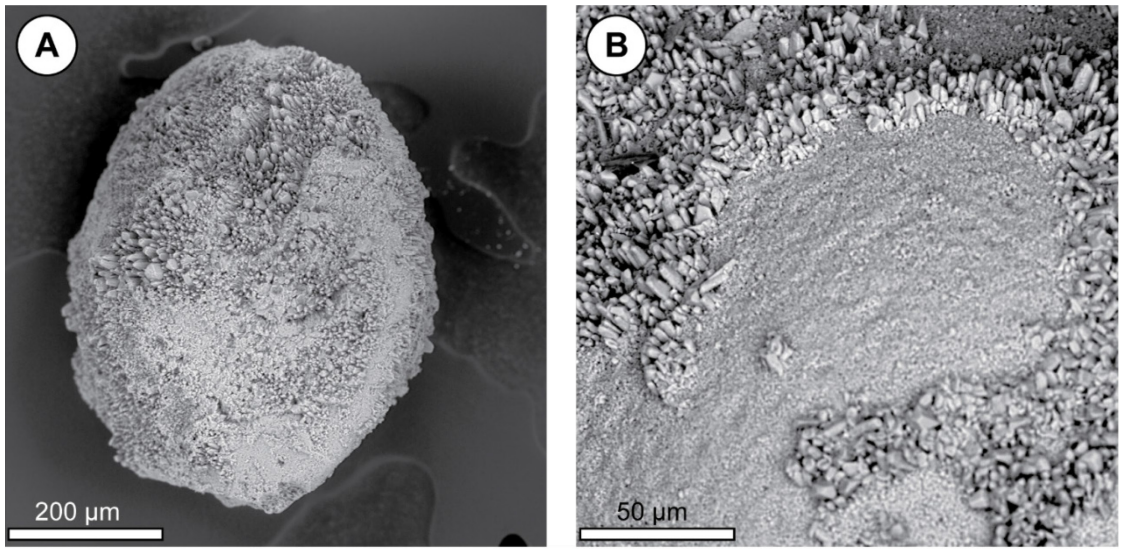

Figure IV.4. Abrasion of tests and crystals. (A) Blunted crystal terminations and planed surface (U1468A-21F-2W 120/122). (B) Blunted crystals and pitted test surface (U1468A-20F-1W 78/80).

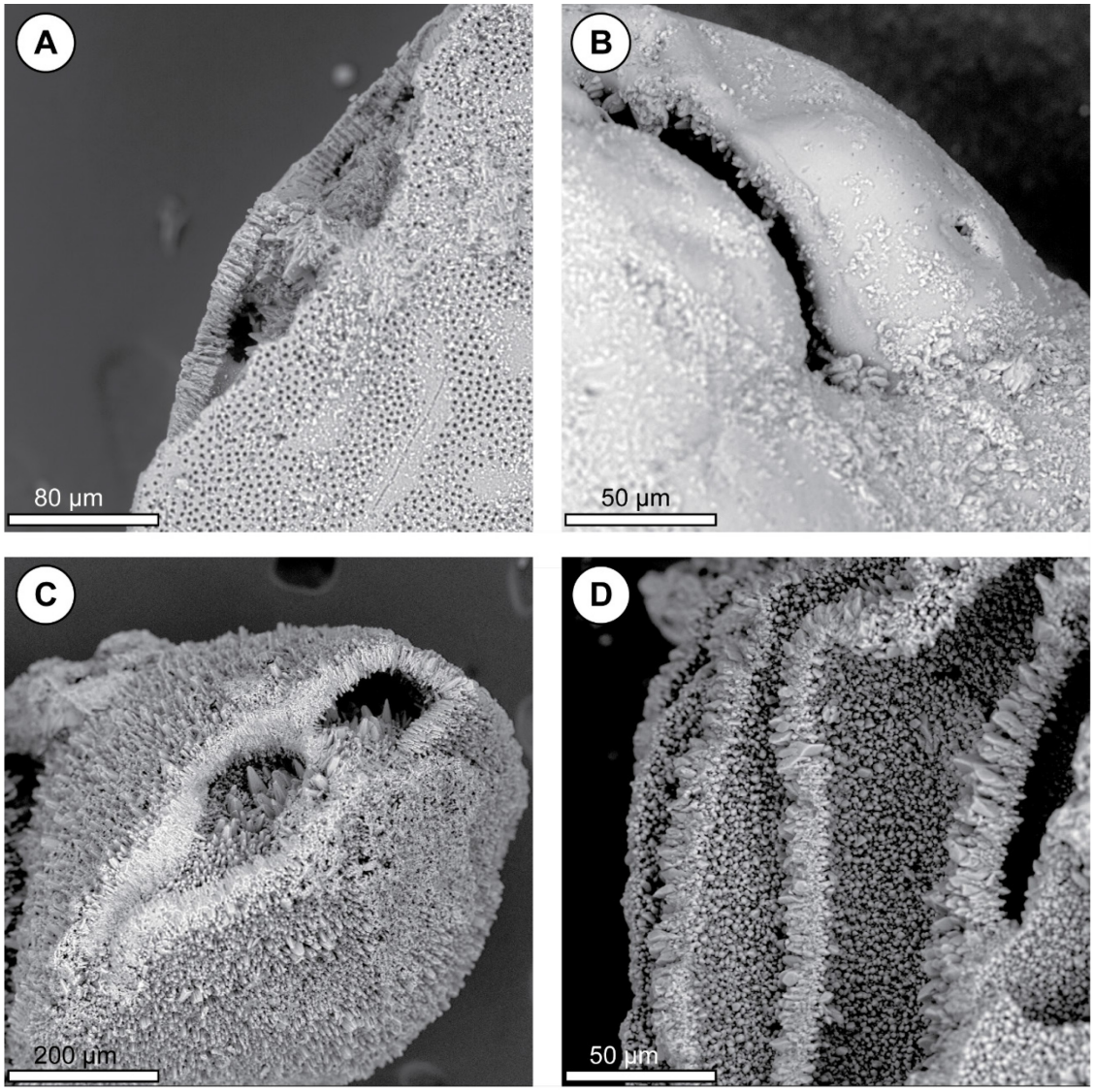

Figure IV.5. States of test preservation. (A) Fractured, uncemented test (U1468A-26F-2W 107/109). (B) Well preserved, minimally cemented test (U1468A-59X-6W 5/8). (C) Overgrown test with aperture showing extensive internal cementation (U1468A-8H-2W 22/25). (D) Fractured test with extensive internal cementation (U1468A-35F-4W 61/63).

Calcite overgrowths (**Figure IV.6**) most commonly occurred as bladed prismatic 'dogtooth' scalenohedral and elongated rhombohedral crystals with sharp to blunted terminations that are between 1 µm and 50 µm (Reinhold, 1999). Crystals are elongate and generally showed well-developed crystal faces. Overall, the calcite crystals show preferred orientation with the c-axis commonly oriented parallel to the foraminifera test. Radial-fibrous cements (**Figure IV.6B**), crystals that converge or diverge on c-axis, are less common but mainly form on top of other calcite crystal beds (Davies, 1977; Mazzullo, 1980). As depth increases, the abundance of calcite overgrowths decreases and it is common to see whole foraminifera with little to no calcite overgrowths at greater depths. This trend is most marked between Units II and III where there is a transition from LBF to planktonic foraminifera and a drastic reduction in the maximum crystal size.

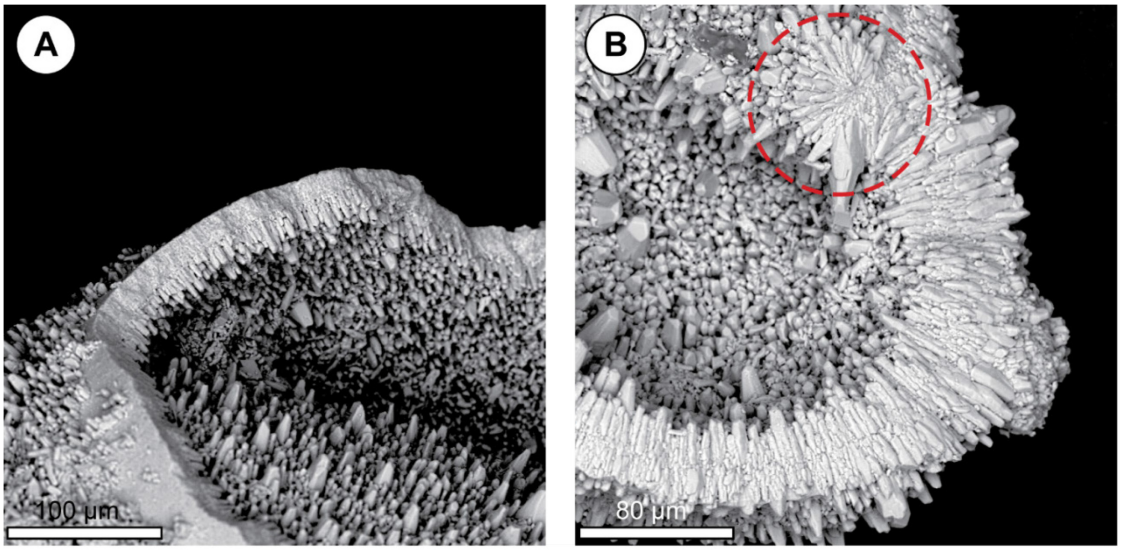

Figure IV.6. **(**A) Dog-tooth cements (U1468A-20F-1W 86/88). (B) Radiaxial-fibrous cement fabric (red dashed circle) (U1468A-13H-3W 130/132).

Dolomite was observed in varying abundances across samples between 62 and 350 mbsf, but was most abundant in samples from 62, 122, 204, 272, and 307 mbsf **(Figure IV.7)**. Dolomite observed under SEM were generally coincident with dolomite peaks from shipboard mineralogy data determined by XRD (Betzler et al, 2017).

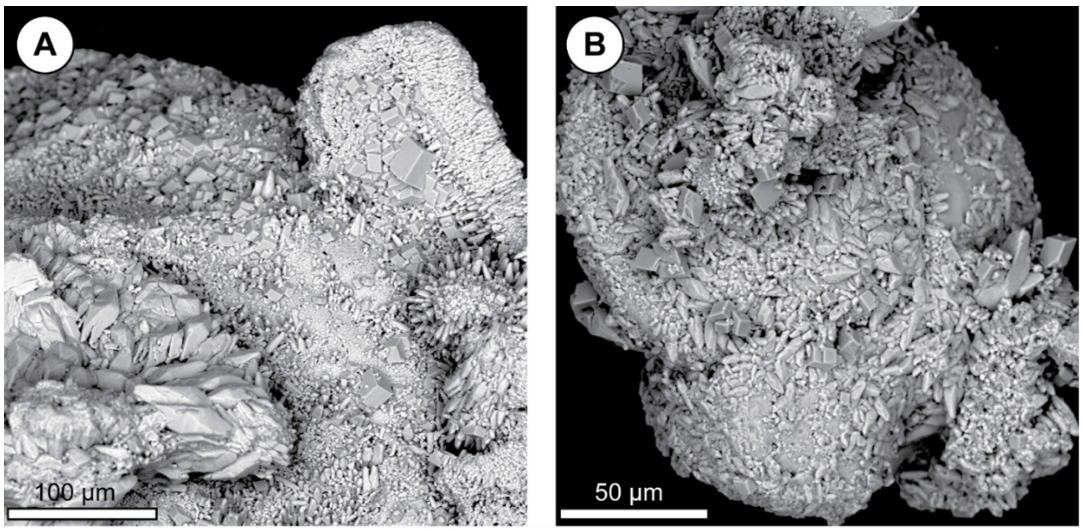

Figure IV.7. Dolomite rhombs in a matrix of calcite crystals. (A) (U1468A-20F-1W 86/88). (B) (U1468A-47F-4W 22/29)

Crystal size

Three cycles were observed between 62 and 200 mbsf where the maximum crystal size oscillates between 35 µm and 50 µm (**Figure IV.8**). Similar changes were noted in grain size with lithostratigraphic summary of Site U1468 showing a transition from granule-medium sand to fine-very fine sand at depths between 200-420 mbsf.

There is much more variation in grain size in Unit II than Units III and IV. These changes are coincident with the relative abundances of LBF and planktonic foraminifera. The mean crystal size averages 13.1 μm above 200 mbsf and then decreases drastically decreasing to 6.2 μm below this depth. The r-squared value for the mean crystal size versus depth is 0.7443 (or 74.43%); enough to suggest that depth can explain the variations in crystal size. This likely reflects the transition in depositional setting from shelf (~400 m water depth) to shallow marine (~50-100 m water depth) between Units II and II as accommodation space filled and seawater advection through the porous, shallow sediments increased.

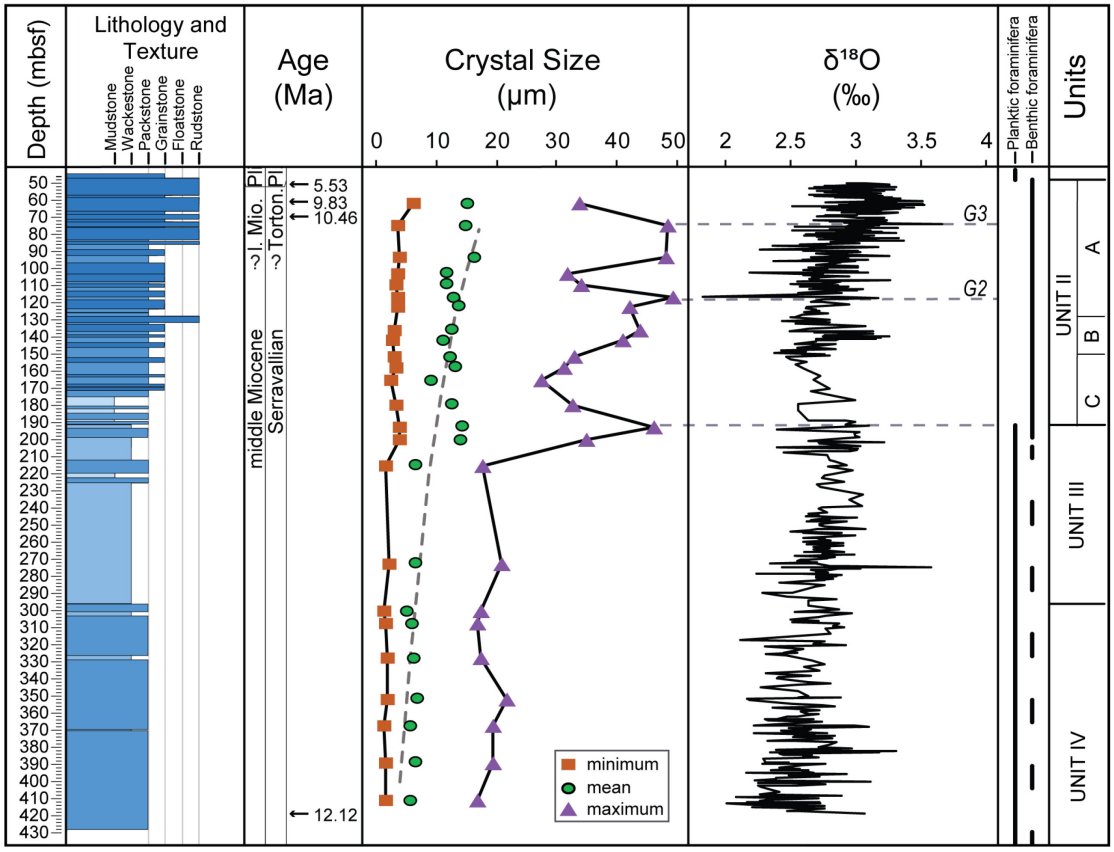

Figure IV.8. Lithology, age and crystal sizes of the study interval from Site U1468. Adapted from Betzler et al., 2017. $\delta^{18}O$ data from Zachos 2001.

Unit II

The crystal lengths measured in the borehole range from a minimum of 1.28 µm to a maximum of 82.05 µm. The average crystal size for all samples is 14.7 µm, and the accompanying median crystal size is 13.5 µm. (**Figure IV.9**). Two peaks were identified in Unit II, with another at the boundary of Units II and III, based on the maximum crystal length, which showed the greatest changes with depth. The first crystal length maxima occurred between 74.58 to 93.35 mbsf where the maximum length was ~48.4 µm. The second maxima at 116.65 mbsf (49.25 µm) with the third maxima at 192.4

mbsf (46.1 µm). All foraminiferal size classes showed the same general trends, with coincident maxima and minima. These varied mainly in magnitude with smaller foraminifera having shorter crystal lengths and larger foraminifera having longer lengths.

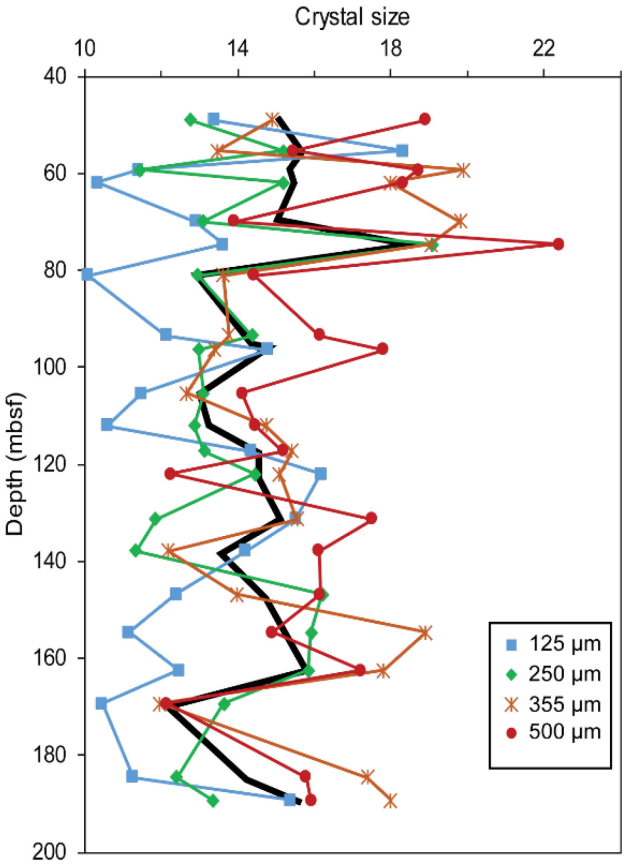

Figure IV.9. Crystal length for grain size classes, Site U1468. The blue squares are the average crystal lengths from the 125 µm size fraction, green diamonds are from the 250 µm size, orange asterisks are are 355 µm, and red circles are 500 µm. The black line is the average crystal c-axis length of the four size fractions.

Discussion

Calcite overgrowths

Overgrowths occur when inorganic calcite precipitates from solution on either the outer or the inner walls of the test (Pearson and Burgess, 2008). Carbonate cementation at or near the sediment-water interface requires a substantial input of $CaCO_3$ and an efficient fluid flow mechanism (Flügel, 2004). Overgrowths at Site U1468 occur mainly as dogtooth calcite cement on both benthic and planktonic foraminifera (Betzler et al., 2016b). This process began with the oversaturation of the pore fluid followed by the nucleation of the crystal and lastly, continued growth if there was sufficient Ca^{2+} supply. Recrystallization is a less obvious process whereby foraminifera tests are replaced at the microgranular level by larger $CaCO_3$ crystals on a very local (submicron) scale and therefore was not considered for this study (Pearson and Burgess, 2008).

Climatic controls on current strength

The distinct variations in grain size in Unit II reflect changes in current strength induced by seasonal variations in monsoonal intensity or by fluctuations in sea level (Betzler et al., 2017). Increased grain size in unconsolidated carbonate oozes relate to increased current strength (House et al., 1991). These changes in grain size, and thereby current velocity, are linked to glacial-interglacial periods, with larger proportions of <63 μm grains representing interglacial periods of high sea level, and thus low bottom

current strength, whereas smaller proportions of <63 μm grains represent glacial periods with low sea level and high bottom current strength (Rendle-Bühring and Reijmer, 2005). As it relates to base level in the narrow Kardiva Channel, lower sea level would result in higher current velocities causing an increase in erosion in the narrowed channel and increased winnowing of fine material. A wide channel during sea level highstands would result in lower current velocities thus increasing the abundance of the fine fraction.

It was demonstrated that there is grain size versus current strength relationship in Plio-Pleistocene sediments of the Maldives by comparing the grain size of periplatform oozes with $\delta^{18}O$, a common geochemical proxy for global glacial/interglacial variations of sea level, and strength of the monsoonal system (and therefore bottom-currents) (Betzler et. al., 2013). Our data, also showing good correlation between a long-term coarsening upward trend with a corresponding upward decrease in abundance the fine fraction, matches an upward trend toward more positive values for $\delta^{18}O$ that suggests long term cooling. These phenomena suggest that the grain size changes of Unit II reflect similar glacial/interglacial variations of sea level, a first for the middle to late Miocene sediments of the Maldives. As to which of these processes (glacioeustasy or monsoonal intensity) exerts a greater influence on grain size, during strong interglacials, Indian Summer Monsoon (ISM) maxima coincide with ice volume minima in the northern hemispehere and Antarctic temperature maxima during the Pleistocene. From peak interglacials into glacials, the ISM weakened as ice volume increased (Zhisheng et al., 2011). Since the grain size maxima in our dataset correspond to glacial periods, it

suggests that glacioeustasy, and not monsoonal changes is the primary control on bottom current intensity.

Crystal size and current strength

Crystal size changed noticeably above 200 mbsf, coinciding with the transition from lithostratigraphic Unit II to Unit III. This unit boundary is marked by a change in dominant foraminifera from planktic in Unit III to benthic in Unit II with a corresponding grain size increase (Betzler et al., 2017). The covariance of crystal length trends across the various foraminiferal size classes suggests that overgrowth development is influenced primarily by environmental factors and is likely independent of foraminiferal species or growth stage.

The thick sediment package of Unit III suggests that sedimentation rates were high during the deposition of this unit. Sediments were able to fill the available accommodation space quickly, resulting in a reduction in water depth and the creation of a shallow environment that served as a large benthic foraminifera carbonate factory during the deposition of Unit II (Betzler et al., 2016). This shallowing of the depositional setting would increase the influence of the bottom currents originating in the Kardiva Channel as the sediment interface came in closer proximity to the channel mouth.

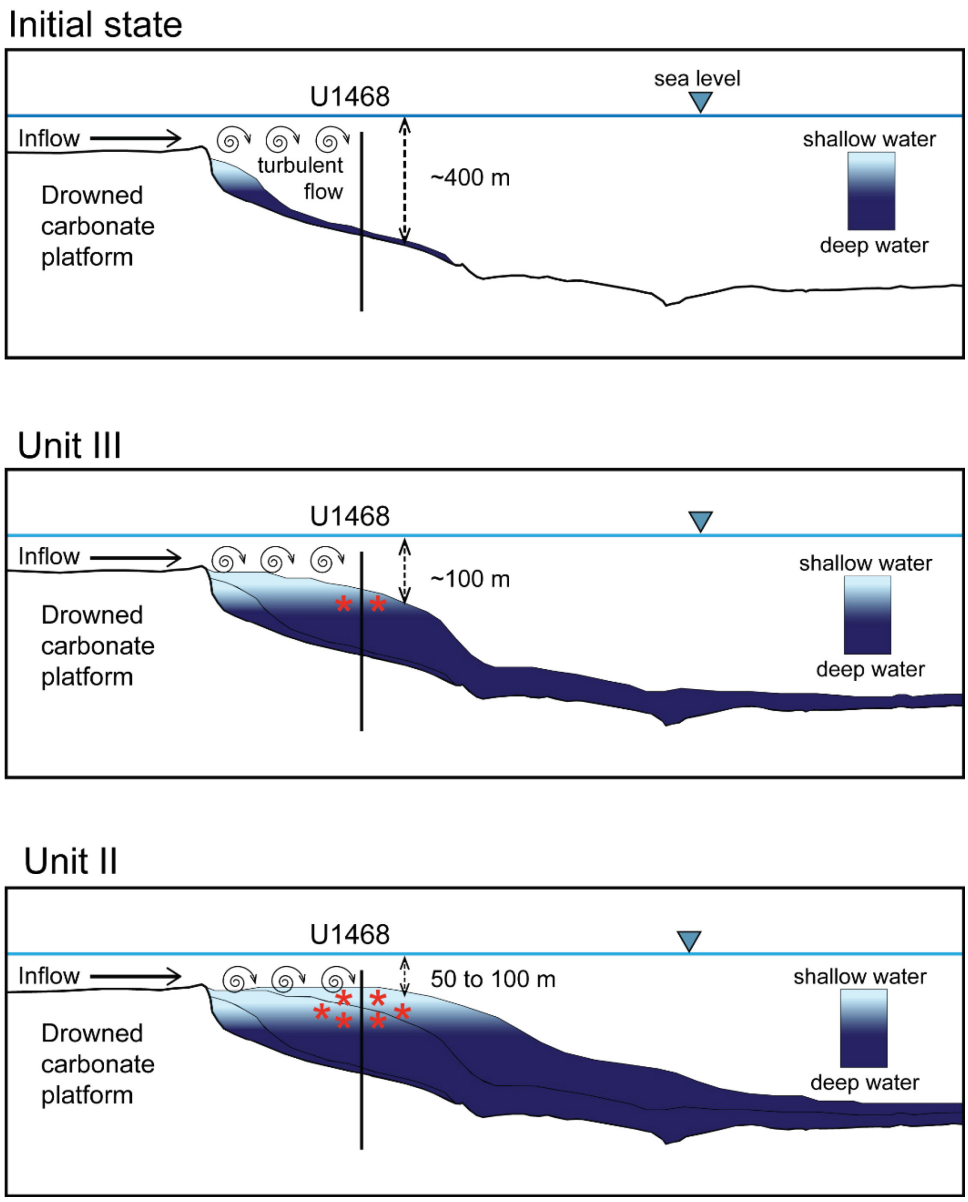

Figure IV.10. Unit III to II foraminifera overgrowth model. Initial state: drift sedimentation is initiated as currents from the Kardiva Channel sweep sediments from the platform and channel, creating a zone of turbulence at it enters the Inner Sea. Unit III: the latest sediments enter the zone of turbulent flow as accommodation space is filled with small crystals (~6 µm) forming mostly on planktonic foraminifera. Unit II: Sediment-water interface is fully established in turbulent flow zone. *In-situ* growth of benthic foraminifera with large crystals (13 µm) forming mostly on benthic foraminifera.

A sudden increase in the fine fraction percentage, in **Figure IV.11**, at approximately 82, 104, 143, 170 and 188 mbsf (here termed IG5 to IG1), is interpreted to be the onset of interglacial periods (House et. al., 1991; Rendle-Bühring and Reijmer, 2005). During glacial periods, there is winnowing of the fine-grained (<63 μm grain size) fraction, controlled by the exposure of the carbonate platforms to bottom currents, allowing glacial periods to be identified using grain size maxima (Lüdmann et al., 2013).

Crystal length maxima generally correspond to the minima of the fine fraction suggesting that crystal growth is enhanced during times of glaciation (G4 through G1) at 162, 120, 75 and 55 mbsf respectively, based on more positive $\delta^{18}O$ data from Zachos et. al., 2001) when bottom currents that are more vigorous winnow fine sediments and promoted crystal growth by enhancing interstitial fluid flow.

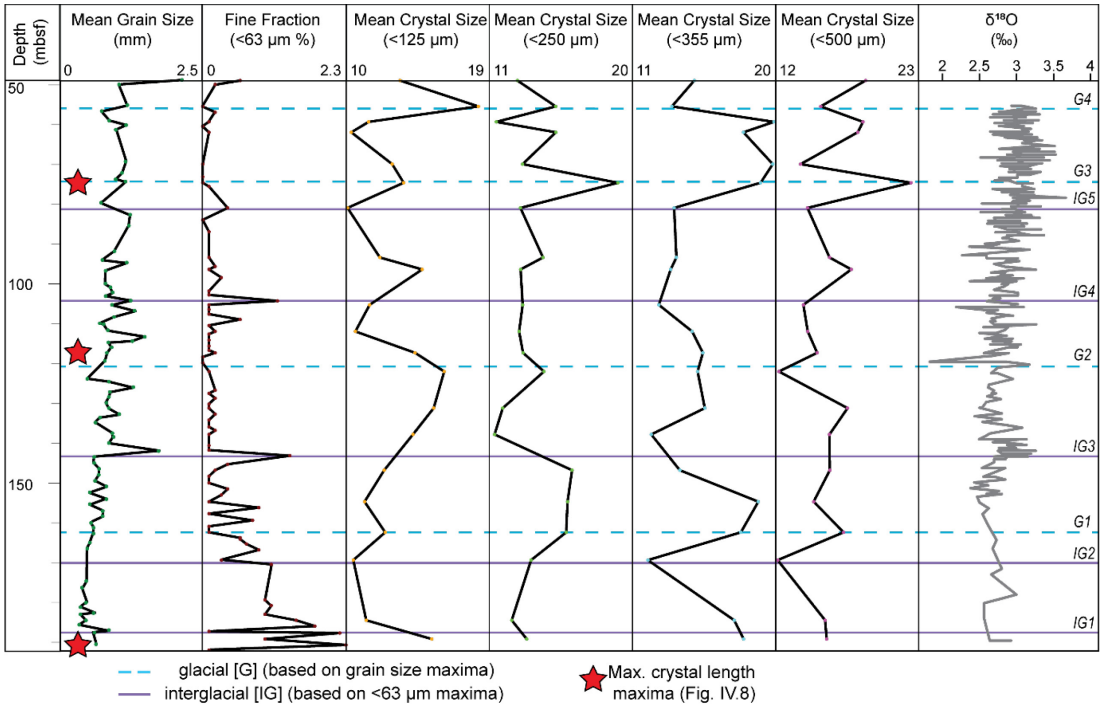

Figure IV.11. Mean grain size, fine fraction and crystal length for various size classes with interpreted glacial-interglacial periods. $\delta^{18}O$ data from Zachos et al., 2001.

Shallow advected zone

A "flushed zone" was identified in platform top at Great Bahama Bank in which analysis of the pore water indicated that advection of seawater is occuring (Eberli et al., 1997). This is an interval (0-150 mbsf) over which the concentration of minor elements did not vary appreciably when compared to seawater. A similar trend occurs at Sites 1004, 1005 (Swart, 1999), 1008 and 1009, which show uniform concentrations of both conservative and non-conservative constituents in the upper 20 - 40 mbsf (Malone et al., 2001). This profile suggests the active advection of seawater through this interval as advection removes the geochemical gradients usually associated with carbonate

diagenesis and diffusion (Swart, 1999). Covariance in pore fluid chloride, $\delta^{18}O$ and δD values, plus anti-correlation of strontium concentrations and calcium isotope ratios, combine to indicate that interstitial water masses are advected through the upper 400 m of the sediment column at the Kardiva Platform (Blättler et al., 2019). Therefore, it is likely that a similar flushed zone existed in the middle to late Miocene sediments at Site U1468. This zone was ~20 to 25 m deep at most as the inflection points (from decreasing to increasing crystal sizes for the 125 or 250 μm grain size classes) occur at or below the interglacial surfaces. The best way to explain this is by advection into the sediments during glacial periods down into lower strata that were originally deposited during interglacial periods (**Figure IV.11**).

A caveat to this approach is that the total duration of a glacial or interglacial period does not correlate directly with depth. Sediment production at Site U1468 is higher during interglacial periods, whereas during glacial times this rate was greatly reduced (Eberli and Betzler, 2019). Therefore, interglacial periods are over-represented when looking at the core and glacial periods are under-represented. Although the sedimentation rate was constant during the deposition of Unit II (Betzler et al., 2016), this approach to the interpretation of the presence of an advective zone must carefully consider changes to the sedimentation rate as this can inflate or deflate the estimation of the perceived depth of a current's infiltration.

Conclusions

The presence of an advective zone in the middle to late Miocene sediments at Site U1468 best explains the observed relationship between diagenetic crystal length, grain size and the abundance of the fine fraction. This zone would have been 20 to 25 m deep in the Maldives archipelago as the crystal lengths maxima occur around at this distance down-core from the onset of glacial periods. We suggest that changes in glacioeustasy, bottom-currents and thereby the advection of seawater below the sediment-water interface can be interpreted from grain and crystal sizes for the middle to late Miocene. Changes in the strength of the advective regime therefore are the main control on the size of the calcite overgrowths suggesting that overgrowth crystal size is a proxy for advective strength.

References

Schrag et al., 1992; Huber et al., 1995; Norris and Wilson, 1998

Banner, F., and Wood, G., 1964, Recrystallization in microfossiliferous limestones: Geological Journal, v. 4, no. 1, p. 21-34.

Betzler, Eberli, G. P., Alvarez-Zarikian, C. A., Alonso-García, M., Bejugam, N. N., Bialik, O. M., Blättler, C. L., Guo, J. A., Haffen, S., and Horozal, S., 2016, International ocean discovery program expedition 359 preliminary report: Maldives monsoon and sea level: Integrated Ocean Drilling Program: Preliminary Reports, no. 359, p. 1-53.

Betzler, C., Eberli, G., Zarikian, C. A., and Scientists, a. t. E., 2017, Maldives Monsoon and Sea Level. Proceedings of the International Ocean Discovery Program, 359: International Ocean Discovery Program.

Betzler, C., Eberli, G.P., Alvarez Zarikian, C.A., Alonso-García, M., Bialik, O.M., Blättler, C.L., Guo, J.A., Haffen, S., Horozal, S., Inoue, M., Jovane, L., Kroon, D., Lanci, L., Laya, J.C., Ling Hui Mee, A., Lüdmann, T., Nakakuni, M., Nath, B.N., Niino, K., Petruny, L.M., Pratiwi, S.D., Reijmer, J., Reolid, J., Slagle, A.L., Sloss, C.R., Su, X., Swart, P.K., Wright, J.D., Yao, Z., Young, J.R. (2017). Site U1468. In Betzler, C., Eberli, G.P., Alvarez Zarikian, C.A., and the Expedition 359 Scientists, Maldives Monsoon and Sea Level. Proceedings of the International Ocean Discovery Program, 359 (pp. 1-40). College Station, TX (International Ocean Discovery Program).

Betzler, C., Eberli, G. P., Lüdmann, T., Reolid, J., Kroon, D., Reijmer, J. J. G., Swart, P. K., Wright, J., Young, J. R., Alvarez-Zarikian, C., Alonso-García, M., Bialik, O. M., Blättler, C. L., Guo, J. A., Haffen, S., Horozal, S., Inoue, M., Jovane, L., Lanci, L., Laya, J. C., Hui Mee, A. L., Nakakuni, M., Nath, B. N., Niino, K., Petruny, L. M., Pratiwi, S. D., Slagle, A. L., Sloss, C. R., Su, X., and Yao, Z., 2018, Refinement of Miocene sea level and monsoon events from the sedimentary archive of the Maldives (Indian Ocean): Progress in Earth and Planetary Science, v. 5, no. 1, p. 5.

Betzler, C., Fürstenau, J., Lüdmann, T., Hübscher, C., Lindhorst, S., Paul, A., Reijmer, J. J. G., and Droxler, A. W., 2013, Sea-level and ocean-current control on carbonate-platform growth, Maldives, Indian Ocean: Basin Research, v. 25, no. 2, p. 172-196.

Betzler, C., Lindhorst, S., Eberli, G. P., Ludmann, T., Mobius, J., Ludwig, J., Schutter, I., Wunsch, M., Reijmer, J. J. G., and Hubscher, C., 2014, Periplatform drift: The combined result of contour current and off-bank transport along carbonate platforms: Geology, v. 42, no. 10, p. 871-874.

Blättler, C. L., Higgins, J. A., and Swart, P. K., 2019, Advected glacial seawater preserved in the subsurface of the Maldives carbonate edifice: Geochimica et Cosmochimica Acta, v. 257, p. 80-95.

Collen, J. D., and Burgess, C. J., 1979, Calcite Dissolution, Overgrowth and Recrystallization in the Benthic Foraminiferal Genus Notorotalia: Journal of Paleontology, v. 53, no. 6, p. 1343-1353.

Davies, G. R., 1977, Former magnesian calcite and aragonite submarine cements in upper Paleozoic reefs of the Canadian Arctic: A summary: Geology, v. 5, no. 1, p. 11-15.

Dunham, R. J., 1962, Classification of carbonate rocks according to depositional textures.

Eberli, G., Swart, P., McNeill, D., Kenter, J., Anselmetti, F., Melim, L., and Ginsburg, R., A synopsis of the Bahamas Drilling Project: results from two deep core borings drilled on the Great Bahama Bank, in Proceedings Proceedings of the ocean drilling program, initial reports1997, Volume 166, p. 23-42.

Embry, A. F., and Klovan, J. E., 1971, A late Devonian reef tract on northeastern Banks Island, NWT: Bulletin of Canadian Petroleum Geology, v. 19, no. 4, p. 730-781.

Flügel, E., 2004, Microfacies of carbonate rocks: analysis, interpretation and application, Springer Science & Business Media.

Friedman, G. M., 1975, The making and unmaking of limestones or the downs and ups of porosity: Journal of Sedimentary Research, v. 45, no. 2.

Gupta, A. K., Yuvaraja, A., Prakasam, M., Clemens, S. C., and Velu, A., 2015, Evolution of the South Asian monsoon wind system since the late Middle Miocene: Palaeogeography, Palaeoclimatology, Palaeoecology, v. 438, p. 160-167.

Gussone, N., Filipsson, H. L., and Kuhnert, H., 2016, Mg/Ca, Sr/Ca and Ca isotope ratios in benthonic foraminifers related to test structure, mineralogy and environmental controls: Geochimica et Cosmochimica Acta, v. 173, p. 142-159.

Haynes, J. R., 1981, Foraminifera, New York, Halsted Press, 433 p.:

Hottinger, L., 1990, Significance of diversity in shallow benthic foraminifera, [Erscheinungsort nicht ermittelbar], [Verlag nicht ermittelbar].

House, M. A., Rea, D. K., and Janecek, T. R., 1991, Grain size record of Oligocene to Pleistocene sediments from Broken Ridge, Supplement to: House, M.A. et al. (1991): Grain-size record of ocean current winnowing in Oligocene to Pleistocene ooze, Broken Ridge, southeastern Indian Ocean. In: Weissel, J; Peirce, J; Taylor, E; et al. (eds.), Proceedings of the Ocean Drilling Program, Scientific Results, College Station, TX (Ocean Drilling Program), 121, 211-218, https://doi.org/10.2973/odp.proc.sr.121.133.1991, PANGAEA.

Huber, B. T., Hodell, D. A., and Hamilton, C. P., 1995, Middle–Late Cretaceous climate of the southern high latitudes: Stable isotopic evidence for minimal equator-to-pole thermal gradients: GSA Bulletin, v. 107, no. 10, p. 1164-1191.

Kendall, A., 1976, Origin of fibrous calcite cements that apparently replace foraminiferal tests: Journal of Sedimentary Research, v. 46, no. 3, p. 545-547.

Lüdmann, T., Betzler, C., Eberli, G. P., Reolid, J., Reijmer, J. J. G., Sloss, C. R., Bialik, O. M., Alvarez-Zarikian, C. A., Alonso-García, M., Blättler, C. L., Guo, J. A., Haffen, S., Horozal, S., Inoue, M., Jovane, L., Kroon, D., Lanci, L., Laya, J. C., Mee, A. L. H., Nakakuni, M., Nath, B. N., Niino, K., Petruny, L. M., Pratiwi, S. D., Slagle, A. L., Su, X., Swart, P. K., Wright, J. D., Yao, Z., and Young, J. R., 2018, Carbonate delta drift: A new sediment drift type: Marine Geology, v. 401, p. 98-111.

Lüdmann, T., Kalvelage, C., Betzler, C., Fürstenau, J., and Hübscher, C., 2013, The Maldives, a giant isolated carbonate platform dominated by bottom currents: Marine and Petroleum Geology, v. 43, p. 326-340.

Malone, M. J., Slowey, N. C., and Henderson, G. M., 2001, Early diagenesis of shallow-water periplatform carbonate sediments, leeward margin, Great Bahama Bank (Ocean Drilling Program Leg 166): GSA Bulletin, v. 113, no. 7, p. 881-894.

Mazzullo, S. J., 1980, Calcite pseudospar replacive of marine acicular aragonite, and implications for aragonite cement diagenesis: Journal of Sedimentary Research, v. 50, no. 2, p. 409-422.

Norris, R. D., and Wilson, P. A., 1998, Low-latitude sea-surface temperatures for the mid-Cretaceous and the evolution of planktic foraminifera: Geology, v. 26, no. 9, p. 823-826.Pawlowski, J., Holzmann, M., Berney, C., Fahrni, J., Gooday, A. J., Cedhagen, T., Habura, A., and Bowser, S. S., 2003, The evolution of early Foraminifera: Proceedings of the National Academy of Sciences, v. 100, no. 20, p. 11494-11498.

Pearson, P. N., and Burgess, C. E., 2008, Foraminifer test preservation and diagenesis: comparison of high latitude Eocene sites: Geological Society, London, Special Publications, v. 303, no. 1, p. 59.

Reinhold, C., 1999, Dog-tooth cements: indicators of different diagenetic environments: Zentralblatt für Geologie und Paläontologie Teil I, v. 1997, p. 1221-1235.

Rendle-Bühring, R. H., and Reijmer, J. J. G., 2005, Controls on grain-size patterns in periplatform carbonates: Marginal setting versus glacio-eustacy: Sedimentary Geology, v. 175, no. 1, p. 99-113.

Reolid, J., Betzler, C., and Lüdmann, T., 2019, Facies and sedimentology of a carbonate delta drift (Miocene, Maldives): Sedimentology, v. 66, no. 4, p. 1243-1265.

Sarkar, S., De, S., and Gupta, A. K., 2009, Late Quaternary Benthic Foraminifera from Ocean Drilling Program Hole 716A, Maldives Ridge, Southeastern Arabian Sea: Micropaleontology, v. 55, no. 1, p. 23-48.

Schrag, D. P., DePaolo, D. J., and Richter, F. M., 1995, Reconstructing past sea surface temperatures: Correcting for diagenesis of bulk marine carbonate: Geochimica et Cosmochimica Acta, v. 59, no. 11, p. 2265-2278.

Swart, P. K., The oxygen isotopic composition of interstitial waters: evidence for fluid flow and recrystallization in the margin of the Great Bahama Bank, in Proceedings Proceedings of the Ocean Drilling Program, Scientific Results2000, Volume 166, p. 91-98.

Udden, J. A., 1898, The Mechanical Composition of Wind Deposits, Lutheran Augustana Book Concern, Printers, 69 p.

Vaziri-Moghaddam, H., Kimiagari, M., and Taheri, A., 2006, Depositional environment and sequence stratigraphy of the Oligo-Miocene Asmari Formation in SW Iran: Facies, v. 52, no. 1, p. 41-51.

Wentworth, C. K., 1922, A Scale of Grade and Class Terms for Clastic Sediments: The Journal of Geology, v. 30, no. 5, p. 377-392.

Zachos, J., Pagani, M., Sloan, L., Thomas, E., and Billups, K., 2001, Trends, Rhythms, and Aberrations in Global Climate 65 Ma to Present: Science, v. 292, no. 5517, p. 686-693.

Zhisheng, A., Clemens, S. C., Shen, J., Qiang, X., Jin, Z., Sun, Y., Prell, W. L., Luo, J., Wang, S., Xu, H., Cai, Y., Zhou, W., Liu, X., Liu, W., Shi, Z., Yan, L., Xiao, X., Chang, H., Wu, F., Ai, L., and Lu, F., 2011, Glacial-Interglacial Indian Summer Monsoon Dynamics: Science, v. 333, no. 6043, p. 719-723.

CHAPTER V

CONCLUSIONS

This study presents the diagenetic history of the drowned Kardiva platform, Maldives, in the context of the significant climatic events of the middle Miocene to Pliocene, utilizing samples collected as part of IODP Expedition 359. Both the depositional and diagenetic history of the platform are divided by its drowning during the middle Miocene as the SAM intensified. This event marks the transition from a sea-level dominated diagenetic regime to one that was controlled by strong bottom currents associated with the SAM.

The sea level controlled diagentic regime is typified by the subaerial exposure of the platform and the influence of meteoric fluids. The cumulative effect of meteoric alteration during this sea level controlled period of the platform's diagenesis was a major shift in mineralogy from aragonite to low-Mg calcite dominated sediments across the DS to PS transition observed at all of the main study Sites.

Evidence of exposure and meteoric alteration is also demonstrated by an exposure surface that is characterized by a C^{12}- enriched negative excursion of stable isotope values for $\delta^{18}O$ and $\delta^{13}C$. This was one of several periods of exposure that affected the platform and overprinted the stable isotopes and elemental concentrations of carbonate cements. The expansion of the EAIS during its first and second growth phases was a likely control during this phase of platform growth and diagenesis as $^{87}Sr/^{86}Sr$ values bounding the most well developed exposure at U1470 are within this period.

The most significant implication of this study is that carbonate platforms situated in low latitude settings record the effects of high latitude glaciations as diagenetic signals. The expansion of the EAIS initiated the narrowing of the ITCZ in the middle Miocene, and likely resulted in more intense rainfall in the region. This represents a new category of evidence for the middle Miocene expansion of the EAIS and demonstrates the impact of this environmental shift on the global sedimentary record.

The bottom current dominated diagenetic regime is characterized by the development of late stage dolomitization and calcite crystal growth in a system where seawater advects at shallow depths through porous sediments. This view of advection as a diagenetic driver is in contrast to most conventional models that typically invoke diffusive flow.

Our model suggests that easterly bottom water flow through the Kardiva Channel is responsible for dolomitization in the northern cores. These currents drive seawater through the upper 50 – 150 m of porous sediments, by interaction with dune bedforms at the sediment water interface, and provide the Mg needed for dolomitization. Dolomite abundance and crystal size are greater in areas proximal to the oceanward aperture of the channel and decreases towards the Inner Sea. This is interpreted to reflect attenuation of the bottom current as it enters the Inner Sea and dissipates over a larger cross-sectional area (i.e., is no longer restricted to the Kardiva channel). Slower bottom water flow means reduced bedform sizes, thus reduced pressure gradients and advective fluxes thus demonstrating the validity of this new model. This new model represents a

complementary scenario to the most commonly invoked seawater dolomitization model i.e. Kohout convection.

For calcite overgrowths at Site 1468, the presence of a shallow advective zone best explains the observed relationship between crystal length, grain size and the abundance of the fine fraction.

All foraminiferal size classes showed the same general trends, with coincident maxima and minima varying mainly in magnitude with smaller foraminifera having shorter crystal lengths and larger foraminifera having longer lengths. This would suggest that the crystal overgrowths are not species or growth controlled (i.e. juvenile versus adult) since all size fractions reflect the same general trends.

Our data suggest that the grain size changes of Unit II reflect glacial/interglacial variations of sea level, a first for the middle to late Miocene sediments of the Maldives. Since the grain size maxima in our dataset correspond to glacial periods, it suggests that glacioeustasy, and not monsoonal changes are the primary control on bottom current intensity as glacial maxima coincide with weaker monsoons.

During times of glaciation, a shallow advective zone extended 20 to 25 mbsf at Site U1468, creating an efficient fluid flow mechanism for the supply of $CaCO_3$ and thus promoting crystal growth. The filling of accommodation space created a shallow marine depositional setting and increased the influence of the bottom currents originating in the Kardiva Channel as the sediment interface moved in closer proximity to the channel mouth.

APPENDIX A

Table A.1. Strontium concentrations (mean) in samples from U1465 and U1470

Description	Depth (mbsf)	*n*	Sr (ppm)	SD	*n*	Mg (ppm)	SD	*n*	Na (ppm)	SD	*n*	Ca (ppm)	SD
U1465B-5R-1W-32/35	85.62												
Blocky		4	555	114	4	6650	1489.55	4	111.25	19.33	4	392750	7154.54
Isopachous		5	584	144	5	36006	51749.26	5	382.8	269	5	398400	17327.43
Dogtooth		-	-	-	-	-	-	-	-	-	-	-	-
Bladed		4	430	177	4	8792.5	4064	4	636.5	726.56	4	386750	7292.98
Syntaxial		-	-	-	-	-	-	-	-	-	-	-	-
Drusy		5	546	62	5	50592	58245.21	5	364.4	305.46	5	395600	8957.68
Brachiopod		-	-	-	-	-	-	-	-	-	-	-	-
U1465B-6R-1W-2/5	90.02												
Blocky		12	739	288	6	8618.33	1056.01	6	142.17	46.09	6	398333.33	4714.05
Isopachous		2	425	3	8	9101.25	1566.38	8	168.88	69.81	8	394750	8856.49
Dogtooth		-	-	-	-	-	-	-	-	-	-	-	-
Bladed		3	503	76	3	9473.33	1600.01	3	137	19.87	3	396000	816.5
Syntaxial		-	-	-	-	-	-	-	-	-	-	-	-
Drusy		1	566	-	1	11840	0	1	290	0	1	395000	0
Brachiopod		-	-	-	-	-	-	-	-	-	-	-	-
U1465C-10X-1W-16/20	90.06												
Blocky		7	457	115	7	7212.86	1790.62	5	4742.4	8356.83	7	393285.71	6385.57
Isopachous		4	485	150	4	10697.5	3895	4	14715	9855.64	4	393425	4323.41
Dogtooth		1	231	-	1	6360	0	1	24700	0	1	386000	0
Bladed		4	517	61	4	9272.5	4201.04	4	5832.5	8158.77	4	387000	3082.21
Syntaxial		-	-	-	-	-	-	-	-	-	-	-	-
Drusy		3	635	167	3	10876.67	1533.98	3	10828.67	8155.66	3	397666.67	12657.89
Brachiopod								-					
U1465C-11X-1W-5/8	99.65												
Blocky		2	585	83	2	16435	9365	2	38091.5	37908.5	2	408500	13500
Isopachous		3	630	115	4	24500	8215.53	4	73500.00	33589.43	4	415250.00	11031.21
Dogtooth		2	443	120	2	8500	2800	2	7566	7434	2	404000	8000
Bladed		2	853	75	2	34650	50	2	109500	4500	2	431500	7500

Table A.1. Continued

Description	Depth (mbsf)	*n*	Sr (ppm)	SD	*n*	Mg (ppm)	SD	*n*	Na (ppm)	SD	*n*	Ca (ppm)	SD
Syntaxial		-	-	-	-	-	-	-	-	-	-	-	-
Drusy		7	664	100	7	10952.86	5172.87	7	16707.57	23103.31	7	400285.71	8310.31
Brachiopod		-	-	-									
U1465B-15R-1W-4/6	143.54												
Blocky		-	-	-	-	-	-	-	-	-	-	-	-
Isopachous		3	754	81	3	8760.00	1400.74	3	493.33	105.23	3	394333.33	2494.44
Dogtooth		1	365	-	1	6090	0	1	2510	0	1	389000	0
Bladed		6	613	61	6	7363.33	1235.53	6	498.33	275.23	6	392666.67	6749.49
Syntaxial		8	736	153	8	7281.25	1621.19	8	191.00	49.47	8	392250.00	9640.41
Drusy			-	-	-	-	-	-	-	-	-	-	-
Brachiopod		-	-	-	-	-	-	-	-	-	-	-	-
U1465B-18R-1W-44/46	163.4												
Blocky		-	-	-	-	-	-	-	-	-	-	-	-
Isopachous		5	563	180	5	37078.00	59467.14	5	283.20	259.31	5	398200.00	6764.61
Dogtooth		7	519	56	7	7507.14	872.94	5	1289.80	2109.44	7	398857.14	7548.48
Bladed		2	654	74	2	5880	650	2	1176.5	843.5	2	371500	14500
Syntaxial		5	404	115	5	4150.00	573.34	4	130.50	94.02	5	391000.00	8366.60
Drusy		-	-	-	-	-	-	-	-	-	-	-	-
Brachiopod		1	751	-	1	6890	0	1	211	0	1	381000	0
U1465-19R-1W-77/80	173.37												
Blocky		4	529	102	4	5005.00	478.36	4	162.50	111.52	4	395750.00	3699.66
Isopachous		2	556	26	2	8370	320	2	473	7	2	392000	6000
Dogtooth		1	575	-	1	4910	0	1	131	0	1	39800	0
Bladed		-	-	-	-	-	-	-	-	-	-	-	-
Syntaxial		2	312	54	2	3925		2	1143	1047	2	401000	3000
Drusy		-	-	-	-	-	-	-	-	-	-	-	-
Brachiopod		9	857	47	9	1554.44	332.52	9	2044.56	286.59	9	391444.44	11557.69
U1470B-14R-CCW-5/7	285.47												
Blocky		11	250	81	7	1201.56	347.25	9	261.14	243.33	9	381000.00	7483.31
Isopachous		5	280	110	5	5038.40	3815.51	4	38435.75	30328.84	5	410800.00	42513.06
Dogtooth		1	279	-	-	-	-	-	-	-	-	-	-
Bladed		-	-	-	2	2050	190	1	273	0	2	379000	16000
Syntaxial		-	-	-	-	-	-	-	-	-	-	-	-

Table A.1. Continued

Description	Depth (mbsf)	*n*	Sr (ppm)	SD	*n*	Mg (ppm)	SD	*n*	Na (ppm)	SD	*n*	Ca (ppm)	SD
Drusy		1	153	-	4	3019.25	1634.39	4	8907.50	10571.36	4	382250.00	10158.12
Brachiopod		-	-	-	-	-	-	-	-	-	-	-	-
U1470B-15R-CCW-1/4	295.14												
Blocky		9	258	86	12	1203.83	384.41	3	51.67	16.66	12	378508.33	7886.22
Isopachous		5	309	62	5	2276.60	270.27	5	972.40	1469.05	5	378800.00	5114.68
Dogtooth		-	-	-	1	1203	0	1	51	0	1	383000	0
Bladed		2	353	109									
Syntaxial		-	-	-	-	-	-	-	-	-	-	-	-
Drusy		4	300	25	1	1800	0	1	630	0	1	374000	0
Brachiopod		-	-	-	-	-	-	-	-	-	-	-	-

Table A.2. Stable isotope values from Sites U1465, U1466, U1468, U1469 and U1470

Sample	Depth (mbsf)	$\delta^{13}C$	$\delta^{18}O$
359-U1465B-2R-1W 19/23-LAYA	66.02	1.034234801	-1.23276469
359-U1465B-3R-1W 16/20-LAYA	75.77	1.633659925	-0.43735678
359-U1465B-3R-1W 56/59-LAYA	76.17	1.748507764	-0.80137405
359-U1465B-4R-1W 6/8-LAYA	80.36	1.383815504	-1.10606255
359-U1465B-4R-1W 45/48-LAYA	80.75	1.131956208	-0.77925146
359-U1465C-8F-CCW 5/7-LAYA	81.74	0.960691887	-1.38561172
359-U1465C-9X-CCW 10/13-LAYA	81.9	1.224640429	-1.09500125
359-U1465B-5R-1W 16/20-LAYA	85.4	1.360644448	-1.25187057
359-U1465B-5R-1W 32/35-LAYA	85.62	1.311280026	-0.96729353
359-U1465B-6R-1W 2/5-LAYA	90.02	1.350570076	-1.24885385
359-U1465C-10X-1W 16/20-LAYA	90.06	1.254863544	-1.22069782
359-U1465B-7R-1W 8/10-LAYA	95.08	1.18837269	-1.38561172
359-U1465C-11X-1W 5/8-LAYA	99.65	1.042294298	-1.28807118
359-U1465B-8R-1W 1/4-LAYA	100.02	1.196432187	-0.85064711
359-U1465B-9R-1W 1/4-LAYA	104.72	0.885134098	-1.10103468
359-U1465C-12X-1W 3/6-LAYA	109.33	1.150090077	-0.98841055
359-U1465C-13X-CCW 5/8-LAYA	114.05	0.753159827	-1.3313108
359-U1465B-10R-1W 8/11-LAYA	114.48	0.976810882	-1.17343591
359-U1465C-15F-2W 17/20-LAYA	124.78	0.834762239	-1.24080927
359-U1465C-15F-2W 44/48-LAYA	125.05	0.955654701	-1.36751142
359-U1465C-15F-CCW 2/5-LAYA	125.39	1.18837269	-1.18047492
359-U1465C-16X-CCW 2/6-LAYA	125.62	0.868007666	-1.14527988
359-U1465B-12R-1W 1/3-LAYA	128.81	1.136993394	-1.26997088
359-U1465B-13R-1W 13/17-LAYA	133.99	1.407993996	-1.11913499
359-U1465C-17X-CCW 12/16-LAYA	135.42	1.25284867	-0.71388924
359-U1465B-15R-1W 4/6-LAYA	143.54	1.307250278	-1.43589035
359-U1465C-18X-CCW 9/12-LAYA	145.09	1.312287464	0.387212738
359-U1465B-16R-1W 6/8-LAYA	148.21	1.734403643	0.850781698
359-U1465B-17R-1W 12/14-LAYA	153.32	1.501685654	-0.92405391
359-U1465B-17R-1W 37/40-LAYA	153.57	1.91775721	-0.99544956
359-U1465B-18R-1W 19/21-LAYA	163.09	1.747500327	-1.10204026
359-U1465B-18R-1W 44/46-LAYA	163.37	1.786790377	-0.883831
359-U1465B-18R-1W 65/68-LAYA	163.57	1.669927663	-1.21164767
359-U1465B-19R-1W 13/16-LAYA	172.73	1.654816106	-1.12315728
359-U1465B-19R-1W 47/51-LAYA	173.07	1.850258919	-1.21868667
359-U1465B-19R-1W 77/80-LAYA	173.37	1.781753191	-0.93410963

Table A.2. Continued

Sample	Depth (mbsf)	$\delta^{13}C$	$\delta^{18}O$
359-U1465B-19R-1W 117/120-LAYA	173.77	1.834139924	-0.82852451
359-U1465B-20R-1W 7/10-LAYA	182.37	1.766641633	-1.17343591
359-U1465B-20R-1W 47/50-LAYA	182.77	1.904660527	-0.75914
359-U1465C-22X-CCW 17/20-LAYA	184.37	1.842199422	-0.96226567
359-U1465B-21R-1W 10/13-LAYA	192.2	1.817013492	-1.20360309
359-U1465B-21R-1W 68/72-LAYA	192.71	2.071895099	-1.06583964
359-U1465B-21R-1W 85/88-LAYA	192.95	1.955032386	-0.94818765
359-U1465B-22R-1W 22/25-LAYA	202.02	2.050738919	-0.78830161
359-U1465B-23R-1W 29/31-LAYA	211.89	2.237114797	-1.06282292
359-U1465B-23R-1W 59/62-LAYA	212.19	2.391252686	-0.74204527
359-U1465B-23R-1W 88/91-LAYA	212.48	2.279427159	-0.62640442
359-U1465B-23R-1W 102/104-LAYA	212.62	2.233085049	-0.75109542
359-U1465C-26X-1W 4/6-LAYA	223.44	2.364051883	-0.75109542
359-U1466A-11H-1W 27/30-LAYA	88.58	1.284079222	-0.94014307
359-U1466A-43F-2W 76/78-LAYA	274.46	1.332436207	-0.86673627
359-U1466A-47F-1W 100/104-LAYA	307.3	1.348555202	-0.80439077
359-U1466A-47F-3W 38/42-LAYA	309.68	1.320346961	-0.96528238
359-U1466B-2R-1W 123/127-LAYA	315.23	1.189380127	-0.83858024
359-U1466B-2R-2W 70/74-LAYA	316.17	1.320346961	-0.42528991
359-U1466B-2R-2W 98/102-LAYA	316.45	1.277027162	-0.61333198
359-U1466A-50X-1W 19/21-LAYA	316.69	1.424112991	-0.66964405
359-U1466A-50X-CCW 44/48-LAYA	317.86	1.675972287	-1.0748898
359-U1466B-3R-1W 125/128-LAYA	324.85	1.254863544	-1.22069782
359-U1466B-4R-1W 80/83-LAYA	334.1	1.842199422	-0.96226567
359-U1466B-5R-1W 58/61-LAYA	343.68	1.312287464	0.387212738
359-U1466B-6R-1W 82/84-LAYA	353.62	1.25284867	-0.71388924
359-U1466B-7R-1W 62/64-LAYA	363.12	2.364051883	-0.75109542
359-U1466B-8R-1W 120/122-LAYA	373.4	0.868007666	-1.14527988
359-U1466B-9R-1W 60/63-LAYA	382.6	0.960691887	-1.38561172
359-U1466B-10R-1-LAYA	392.61	1.224640429	-1.09500125
359-U1466B-10R-2W 15/19-LAYA	393.1	0.955654701	-1.36751142
359-U1466B-11R-2 30/33-LAYA	402.65	1.150090077	-0.98841055
359-U1466B-11R-CCW 17/21-LAYA	403.48	0.834762239	-1.24080927
359-U1466B-13R-1W 81/84-LAYA	421.61	2.119244647	-0.76617901

Table A.2. Continued

Sample	Depth (mbsf)	$\delta^{13}C$	$\delta^{18}O$
359-U1466B-14R-1W 58/60-LAYA	431.08	0.753159827	-1.3313108
359-U1466B-29R-1W 50/54-LAYA	440.58	1.18837269	-1.18047492
359-U1466B-30R-1W 14/17-LAYA	542.6	1.042294298	-1.28807118
359-U1466B-31R-2W 54/59-LAYA	547.24	1.926824145	-1.1553356
359-U1466B-32R-1W 51/56-LAYA	558.14	1.699143342	-0.11959584
359-U1466B-33R-1W 34/38-LAYA	567.01	1.527879021	-0.0954621
359-U1466B-33R-1W 105/109-LAYA	576.54	1.448291483	-1.10002911
359-U1466B-34R-1W 95/98-LAYA	577.25	1.618548367	-1.59376525
359-U1466B-35R-1W 37/40-LAYA	586.85	1.49967078	-1.37153371
359-U1466B-35R-2W 95/98-LAYA	595.97	1.577243443	-1.61287113
359-U1466B-36R-1W 27/30-LAYA	597.56	1.826080427	-0.48461869
359-U1466B-36R-1W 63/66-LAYA	605.57	1.814998618	-0.3559054
359-U1466B-37R-1W 89/92-LAYA	605.93	1.439224549	-0.61735427
359-U1466B-39R-1W 53/57-LAYA	615.89	1.797872186	-0.10250111
359-U1466B-39R-1W 101/105-LAYA	634.93	1.445269172	0.087552109
359-U1466B-40R-1W 44/48-LAYA	635.41	1.406986559	-0.56405892
359-U1466B-42R-1W 45/49-LAYA	644.54	1.836154799	-0.18194134
359-U1468A-7H-1W 67/71-LAYA	663.95	2.03965711	-0.2312144
359-U1468A-7H-2W 23/26-LAYA	50.9	2.266330476	-0.48964655
359-U1468A-7H-3W 55/58-LAYA	52.4	1.281056911	-1.8230358
359-U1468A-35F-3W 98/101-LAYA	53.9	1.792835	-0.11356241
359-U1468A-39X-1W 130/132-LAYA	213.48	1.876452286	-0.61835984
359-U1468A-39X-2W 21/23-LAYA	225.6	1.55306495	-0.64953259
359-U1468A-43X-1W 0/2-LAYA	227.11	1.72130696	-0.27043173
359-U1468A-53X-2W 0/0-LAYA	262.5	1.912720025	-0.19199707
359-U1468A-57X-CCW 5/7-LAYA	326.11	1.5137749	-0.89288116
359-U1468A-59X-1W 32/35-LAYA	346	1.223632991	-0.8214855
359-U1468A-59X-3W 30/32-LAYA	359.7	1.461388167	-0.46249609
359-U1468A-59X-4W 27/30-LAYA	362.7	1.587317814	-0.03211103
359-U1468A-59X-5W 94/96-LAYA	364.2	1.339488267	6.72942E-05
359-U1468A-60X-CCW 9/12-LAYA	365.7	1.054383545	-0.65254931
359-U1468A-61X-4W 104/108-LAYA	369.5	1.075539726	-0.46551281
359-U1468A-61X-6W 21/23-LAYA	383.7	1.115837213	-0.03915004
359-U1468A-61X-7W 36/38-LAYA	386.7	1.1561347	-0.35489983

Table A.2. Continued

Sample	Depth (mbsf)	$\delta^{13}C$	$\delta^{18}O$
359-U1468A-62X-CCW 6/9-LAYA	387.71	0.907297716	-0.47054067
359-U1468A-63X-1W 79/82-LAYA	388.9	0.875059726	-0.62539885
359-U1468A-64X-2W 19/21-LAYA	398.6	0.839799425	-0.24931471
359-U1468A-64X-CCW 20/23-LAYA	409.8	0.660475606	-0.70282794
359-U1468A-65X-1W 28/30-LAYA	411.72	0.921401837	-0.23925898
359-U1468A-66X-1W 21/24-LAYA	418	0.700773093	-0.21713638
359-U1469A-6R-CCW 1/3-LAYA	427.7	0.97378857	0.337939682
359-U1469A-9R-CCW 1/3-LAYA	44.51	1.011063746	0.828659101
359-U1469A-10R-CCW 3/5-LAYA	73.61	0.378393195	-0.72495054
359-U1469A-11R-CCW 3/5-LAYA	83.33	0.859948168	0.375145867
359-U1469A-11R-CCW 42/44-LAYA	93.03	0.246418924	1.654234191
359-U1469A-12R-CCW 13/15-LAYA	93.35	0.29074616	0.820614521
359-U1469A-13R-CCW 2/4-LAYA	102.83	0.171868572	0.985528424
359-U1469A-14R-CCW 10/12-LAYA	112.42	1.164194198	-0.65355488
359-U1469B-4R-CCW 3/5-LAYA	122.2	0.633274802	1.947861385
359-U1469A-16R-CCW 8/11-LAYA	141.63	1.102740529	1.697473812
359-U1469B-4R-CCW 23/25-LAYA	141.68	1.0775546	1.316361804
359-U1469A-17R-1W 2/4-LAYA	141.88	2.496026153	3.220916273
359-U1469A-17R-1W 47/50-LAYA	151.42	2.402334495	2.605505853
359-U1469A-17R-1W 77/80-LAYA	151.87	2.413416304	3.112314434
359-U1469A-17R-2W 19/22-LAYA	152.17	2.370096506	2.72516899
359-U1469A-17R-2W 47/50-LAYA	152.59	2.362037008	3.041924353
359-U1469A-17R-CCW 4/7-LAYA	152.87	2.202861933	2.486848288
	153.27	2.313680023	2.526065619
359-U1470A-17H-CCW 5/7-LAYA	148.33	1.296168469	-1.13622972
359-U1470A-18X-1W 8/10-LAYA	148.48	-0.24420298	-3.66524477
359-U1470A-20F-CCW 3/4-LAYA	164.67	0.031834804	-3.0478232
359-U1470A-21F-1W 85/89-LAYA	165.08	0.082206663	-2.75117929
359-U1470A-21F-2W 64/66-LAYA	166.09	0.351192391	-1.77677946
359-U1470A-21F-CCW 1/3-LAYA	166.87	0.276642039	-1.99800543
359-U1470A-22X-CCW 5/7-LAYA	167.05	-0.23009886	-2.38615644
359-U1470A-24X-1W 7/9-LAYA	168.98	-0.17468982	-2.23330941
359-U1470B-2R-CCW 8/11-LAYA	178.65	0.540590581	-2.04124505

Table A.2. Continued

Sample	Depth (mbsf)	$\delta^{13}C$	$\delta^{18}O$
359-U1470B-3R-CCW 5/7-LAYA	180.38	0.90931259	-1.30416034
359-U1470B-4R-CCW 8/10-LAYA	188.38	1.063450479	-1.75365129
359-U1470B-5R-1W 22/24-LAYA	198.22	1.02013068	-1.6028154
359-U1470B-5R-1W 47/49-LAYA	198.47	1.048338922	-1.55957578
359-U1470B-5R-1W 124/127-LAYA	199.24	0.904275404	-1.64002159
359-U1470B-5R-2W 12/14-LAYA	199.6	0.875059726	-1.60382097
359-U1470B-5R-2W 84/86-LAYA	200.32	0.827710179	-1.46304081
359-U1470B-5R-3W 23/25-LAYA	200.69	0.69472847	-1.68125006
359-U1470B-5R-3W 55/57-LAYA	201.01	0.287723848	-1.70035594
359-U1470B-5R-CCW 3/5-LAYA	201.32	0.357237014	-1.71443396
359-U1470B-6R-1W 8/10-LAYA	207.78	0.33003621	-1.75264572
359-U1470B-6R-1W 34/37-LAYA	208.04	0.40156425	-1.94370451
359-U1470B-6R-1W 90/93-LAYA	208.6	-0.33587977	-3.63909988
359-U1470B-7R-1W 49/52-LAYA	217.89	0.881104349	-2.17196948
359-U1470B-8R-CCW 4/6-LAYA	227.14	0.109407467	-4.02825647
359-U1470B-10R-CCW 7/10-LAYA	246.57	0.127541336	-0.28953761
359-U1470B-12R-CCW 3/5-LAYA	265.93	-1.97195775	-5.26108845
359-U1470B-13R-CCW 21/24-LAYA	275.81	-0.60385806	-4.36713443
359-U1470B-14R-CCW 5/7-LAYA	285.45	-5.58966468	-7.09525284
359-U1470B-15R-CCW 1/4-LAYA	295.11	-7.03835935	-6.60352785
359-U1470B-16R-CCW 3/5-LAYA	304.83	-0.63408117	-6.07459667
359-U1470B-17R-CCW 1/4-LAYA	314.51	-1.36850288	-5.84029826
359-U1470B-18R-1W 5/8-LAYA	324.35	0.379400632	-5.66331749
359-U1470B-18R-1W 28/31-LAYA	324.58	0.999981937	-4.07551838
359-U1470B-18R-1W 41/44-LAYA	324.71	1.019123243	-4.44959138
359-U1470B-18R-1W 50/52-LAYA	324.8	1.035242238	-4.58936597
359-U1470B-18R-CCW 5/8-LAYA	324.89	1.082591786	-3.84926455
359-U1470B-19R-CCW 1/3-LAYA	334.01	0.312909778	-5.57784382